Pyrite chemistry and S isotope systematics associated with paragenesis of epithermal-style gold mineralization in the Eastern Cobequid Highlands, Nova Scotia, Canada

By
Kali Jolane Gee

A Thesis Submitted to
Saint Mary's University, Halifax, Nova Scotia
in Partial Fulfillment of the Requirements for
the Degree of Bachelor of Science with Honours in Geology

April 26, 2019, Halifax, Nova Scotia

Approved: Dr. Jacob Hanley

Examining committee

Approved: Dr. James Brenan

External reader

Date: April 26, 2019

Pyrite chemistry and S isotope systematics associated with paragenesis of epithermal-style gold mineralization in the Eastern Cobequid Highlands, Nova Scotia, Canada

by Kali Jolane Gee

Abstract

Within the northeastern Cobequid Highlands (CH), Nova Scotia, Canada recent bedrock mapping and bulk rock geochemistry have identified a potential epithermal Au system. The Warwick Mountain area shows the most potential for Au mineralization with two zones of intensely silicified and sulphidized basalt identified. Assays show anomalous As, Sb, Cd, W, Hg, with Au concentrations up to ~660 ppb.

Trace element chemistry and S isotope systematics of sulphide minerals are used to track deposit evolution and epithermal processes at a variety of scales, and develops exploration criteria using these data.

The host rock setting, enrichments in bulk rock Au, As, Sb, and Hg, and sulphide mineralogy are consistent with a low sulphidation epithermal Au style of mineralization. The bulk S (as mainly pyrite) correlates to bulk $\delta^{34}S_{VCDT}$, possibly as a function of sulphate content enriched during sample weathering in core. The As content of pyrite correlates weakly to in-situ $\delta^{34}S_{VCDT}$ (by SIMS) in pyrite with

As-rich zones often showing high $\delta^{34}S_{VCDT}$, suggesting that ^{34}S enrichment and As enrichment were coupled. Bulk $\delta^{34}S_{VCDT}$ correlates to in-situ $\delta^{34}S_{VCDT}$ but bulk $\delta^{34}S_{VCDT}$ values are consistently higher by several ‰, suggesting partial oxidation of sulphides to sulphates and preferential loss of ^{32}S in core during long-term storage (degassing, removal by rain water?). Pyrite grains with rare, late overgrowths showing very high $\delta^{34}S_{VCDT}$ values are attributed to sulphide derived from the reduction of seawater sulphate. There are systematic variations in As and $\delta^{34}S_{VCDT}$ in surface samples and a few core samples. The biggest variation between core and rim $\delta^{34}S_{VCDT}$ to more negative values occurs at the Nuttby Mountain occurrence, where late enrichment in Au, Ag, As, and Sb occurs in the rims of pyrite grains. Similar rim enrichment in Au was observed in some pyrite from drill core.

April 26, 2019

Table of Contents

List of Figures

List of Tables

Acknowledgements

1.0 Introduction

1.1 Objectives of study

In the northeastern Cobequid Highlands (CH), Nova Scotia, approximately 30 km northeast of Truro, Nova Scotia, bedrock mapping and bulk rock geochemical surveys by the Nova Scotia Department of Natural Resources has identified a potential epithermal Au system in Late Devonian to Early Carboniferous bimodal volcanics (MacHattie, 2011). Two Au occurrences have been documented (the Warwick and Nuttby Mountain Au occurrences), comprising zones of silicified and sulphidized volcanic rocks with bulk rock assays yielding up to 660 ppb Au (MacHattie, 2011). Following the discovery of the Au occurrences, a total of 388m of drilling was completed (two holes) by RJ Drilling Ltd. for Sugarloaf Resources Ltd. approximately 770m northwest of the Warwick Mountain Au occurrence (Jensen, 2012). Drilling showed heavily sulphidized volcanic rocks at depth but only slightly anomalous Au relative to Warwick and Nuttby Mountain Au occurrences. To date no detailed study has characterized the sulphide mineralogy of these newly discovered epithermal occurrences.

Pyrite is a key host phase for Au and a mineral that is shown to record the hydrothermal evolution of mineralizing systems (Pals et al., 2003; Reich et al., 2005; Kouhestani et al., 2012; Deditius et al., 2014; Cook et al., 2015; Franchini et al., 2015; Gregory et al., 2015; Neyedley, 2017; Kerr, 2018; Román et al., 2018; Sykora et al., 2018). Key objectives of this B.Sc. Honours thesis are to: (i) use trace element chemistry and S isotope systematics of sulphide minerals in the epithermal mineralized rocks to track deposit evolution and processes including

boiling and oxidation, and (ii) use complimentary in-situ techniques in tandem to understand mineralizing processes at a variety of scales. Integration of this information into a future genetic model will aim to develop exploration criteria for this style of mineralization in the CH.

In this study, pyrite (the dominant sulphide phase of hydrothermal origin) from drill core and surface localities in the eastern CH was examined using a variety of analytical techniques. Following bulk S isotope analyses of drill core samples, reflected light petrography, scanning electron microscopy backscattered electron (SEM-BSE) imaging, and SEM-energy dispersive spectroscopy (SEM-EDS) were used to characterize the mineralogy and textural characteristics of pyrite and other sulphides present. Representative pyrite grains were investigated in-situ by secondary ion mass spectrometry (SIMS) to determine their $\delta^{34}S$ composition. Electron microprobe (EMP) and laser ablation inductively coupled plasma mass spectrometry (LA-ICP-MS) were used to characterize pyrite and trace element composition.

1.2 General characteristic of epithermal gold systems

Epithermal systems can broadly be classified in to two variants: low sulphidation and high sulphidation systems, primarily based on hydrothermal fluid acidity, and oxidation states (White and Hedenquist, 1995). Low sulphidation systems are typically more oxidized, involve higher fS_2, and show evidence of low pH fluids. They generally form in magmatic hydrothermal environments and steam heated (geothermal) regions (Rye et al., 1992), in close proximity to magmas that

serve as heat and volatile sources, with fluid temperatures ranging from 100 – 400°C depending on the setting. They are typically formed at shallow depths (<2000 m; Taylor, 2007). Albeit, it is the distinct changes in temperature and pressure that allow characterization of the environment, as they generally occur over short distances.

Low sulphidation systems typically occur in an extensional tectonic environment and their formation is often fault controlled, causing the deposits to cover a generally small area. They occur primarily in igneous rocks (predominantly volcanic)   but can also occur in sedimentary and metamorphic rocks. The mineralization events are similar in age to the formation of the host rock, within 0.5 Ma. Most low sulphidation deposits are Tertiary in, but some deposits have been discovered that are Jurassic, Devonian, and even late Proterozoic in age (Wrucke and Armbrustmacher, 1975; Diakow et al., 1983; Lindhorst and Cook, 1990).

Gold and/or silver are the principle commodity of these deposits and is hosted in quartz-dominated veins. Gold commonly occurs as free gold, alloyed with silver, or included in the structure of sulphides or as Au-Ag-Te minerals (Ashley, 1982). In addition to being alloyed with gold, most silver occurs as native silver or sulphosalts (e.g. acanthite-argentite or proustite-pyrargyrite) or as tellurides (e.g hessite). Specific to the magmatic hydrothermal environments, mineral assemblages include pyrite, enargite, tennantite, covellite, sphalerite, and galena. Many deposits also show a characteristic enrichment in elements such as Hg, As, Sb, and Tl. Characteristic alteration typically includes silicification, sericitization, and chloritization. Evidence of boiling can be seen in veins, in the form of bladed

calcite, as well as jigsaw, plumose, and colloform quartz textures (Moncada et al., 2008).

Deposit formation requires a sustained and localized heat and fluid source. It is hypothesized that gold is sourced from the magma that is acting as the heat sources, or it is leached from the host rocks of the surrounding area. To form a low sulphidation system, it is hypothesized that a highly acidic magmatic-hydrothermal plume ascends over a short period of time and boils due to compression fluid, or mixes with meteoric fluids heated by magma providing ore fluids (Poulsen, 1996).

2.0 Geological Setting

2.1 Regional geology of the eastern Cobequid Highlands

The CH are located in the northwestern part of the Nova Scotia mainland, spanning a distance of approximately 150 km from Cape Chignecto to Pictou County. The CH are located directly north of the Cobequid Chedabucto fault zone, consisting of Avalonian Proterozoic rocks, Silurian to Lower Devonian sedimentary rocks, and Devonian to early Carboniferous plutonic and volcanic rocks (Pe-Piper and Piper, 2002).

The Au occurrences and associated mineralized volcanic rocks studied here occur in the northeastern CH, Nova Scotia, Canada. The ~450 km^2 area of focus is bordered by the Cobequid-Chedabucto fault zone to the south and the Cumberland Basin, comprised of Late Carboniferous sedimentary rocks, to the north (Figure 1). To the northeast, Neoproterozoic and Silurian rocks are in fault contact with the area (Donohoe and Wallace, 1982). The bi modal rocks that host

the Au occurrences display within-plate geochemical signatures and are coeval with the development of the Maritimes Basin, suggesting they formed in a plume-related intra-continental rift (Dessureau et al., 2000).

The area is subdivided into four main lithological units: the Folly Lake Pluton, the Hart Lake-Byers Lake Pluton, the Byers Brook Formation, and the Diamond Brook Formation. The sequence is comprised of gabbro-diorite, overlain by granite, which is overlain by felsic volcanic and volcaniclastic rocks, and finally vesicular basalt flows. The magmatic events responsible for the rock sequence can be generally divided into two major events: (i) the intrusion of the Hart Lake-Byers Lake pluton and the coeval emplacement of the Byers Brook Formation (ca. 365-355 Ma; Dunning et al., 2002), and (ii) the emplacement of the Diamond Brook Formation and the injection of diorite and diabase dykes and sills lower in the magmatic package (ca. 355-350 Ma; Dunning et al., 2002). The succession is unique in that it has been uplifted and tilted (~350-310 Ma) to a near-vertical northwest-striking orientation (MacHattie, 2013). The potential for low sulphidation epithermal Au mineralization is considered likely in such an environment comprised of modern and ancient rift-related bi-modal volcanic succession, similar to other epithermal mineralized environments globally (e.g., the Miocene deposits in the Great Basin, Nevada; John, 2001).
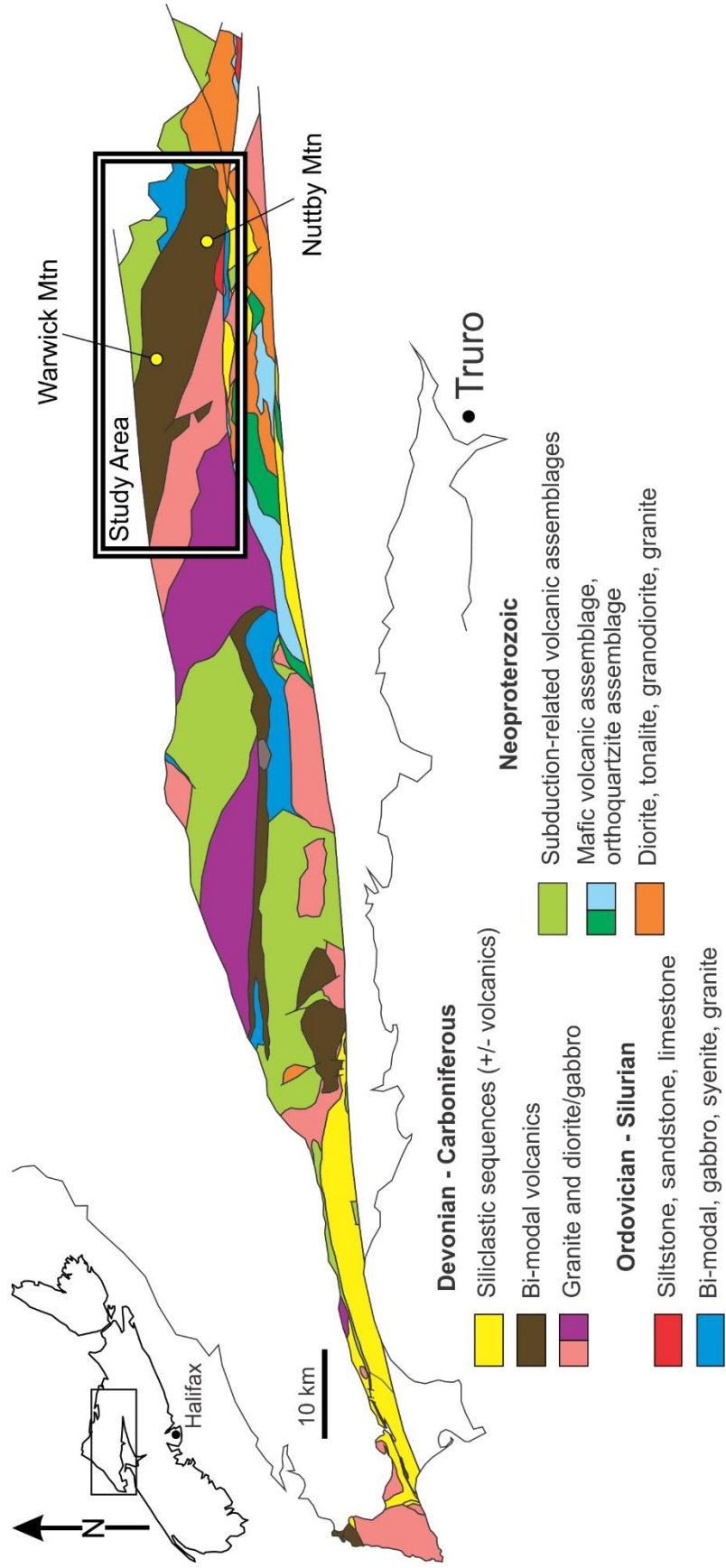
Figure 1 - Geological map of the Eastern Cobequid Highlands with study area outlined. Two distinct volcanic formations comprise the bi-modal volcanics: i) the Byers Brook Formation consisting of felsic and volcaniclastic rocks and ii) the overlying Diamond Brook Formation comprised of vesicular basalts with minor felsic volcaniclastic rocks.

7

2.2 Characteristics of epithermal mineralization in the study area

Within the Diamond Brook Formation, the Warwick Mountain area shows the most potential for Au mineralization as indicated by intense silicification and sulphidization of basalt at two different "zones" or localities (Figure 2A; MacHattie, 2011). The alteration in the basalt consists of pervasive quartz + sericite + carbonate + pyrite ± chlorite ± epidote (MacHattie, 2013). Of four assayed samples collected during early field work, one returned a highly anomalous Au concentration (~660 ppb; MacHattie, 2013), as well as anomalous concentrations of several other trace metals of epithermal affinity including: As (200-300 ppm), Sb (15-25 ppm), W (6-16 ppm), and Pb (150-500 ppm). A disaggregated rock sample from the first location was sieved and panned, resulting in the recovery of several gold grains < 500 μm in diameter (MacHattie, 2011). Four samples were also assayed from a second zone, returning lower Au concentrations (25-70 ppb) and trace element concentrations (MacHattie, 2011). Within the Byers Brook Formation, the Nuttby Mountain area also shows high potential for gold mineralization (Figure 2B). Two samples were assayed and returned anomalous Au concentrations (50-150 ppb), as well as slightly anomalous concentrations of As (~100 ppm), Sb (4-7 ppm), and Pb (~50 ppb; MacHattie, 2011). Field work completed in 2016 revealed anomalously high concentrations of As and Sb at several locations throughout the surrounding areas (Figure 3; MacHattie, 2016).

In 2011, property in the Whirley Brook area, Colchester County was staked by Sugarloaf Resources Ltd. following exploration conducted by the Nova Scotia Department of Natural Resources. Wireline drilling (NQ) was conducted by RJ

Drilling Ltd to obtain 388m of drill core between two drill holes, DDH SL-11-01 (Core 1) and DDH SL-11-02 (Core 2). The first hole (Core 1) was 197 m in length, drilled toward 188° Az at 45° dip. The second hole (Core 2) was 191m in length, drilled toward drilled toward 188° Az at 60° dip. The collars were approximately 700m to the northwest of the Warwick Mountain Au occurrence (Figure 4). Within drill core obtained, alteration similar to that observed at the Warwick Mountain occurrence was observed in several narrow, silicified and pyrite-rich zones within the first 100 m of Core 1. Assays from various intervals returned highly anomalous concentrations of As (215-700 ppm), but much lower than were seen in surface zones. Assays also returned low concentrations of Au (8-20 ppb) and Ag (270-950 ppb; Jensen, 2012). Drill core from Core 2 encountered a less silicified zone containing disseminated, fine grain pyrite. Assays from 141-150 m in depth returned anomalous concentrations of As (up to 200 ppm), and Pb (600 ppm), but low concentrations of Ag (272 ppb), and only slight enrichment in Au and Mo relative to background (Jensen, 2012).

Figure 2 - Outcrop at Warwick and Nuttby Mountain Au occurrences. A) Silicified and sulphidized basalt from Warwick Mountain and Nuttby Mountain outcrops. Assays returned up to 660 ppb gold. B) Sulphide veinlet cross cutting rhyolite. Assays returned up to 150 ppb gold.
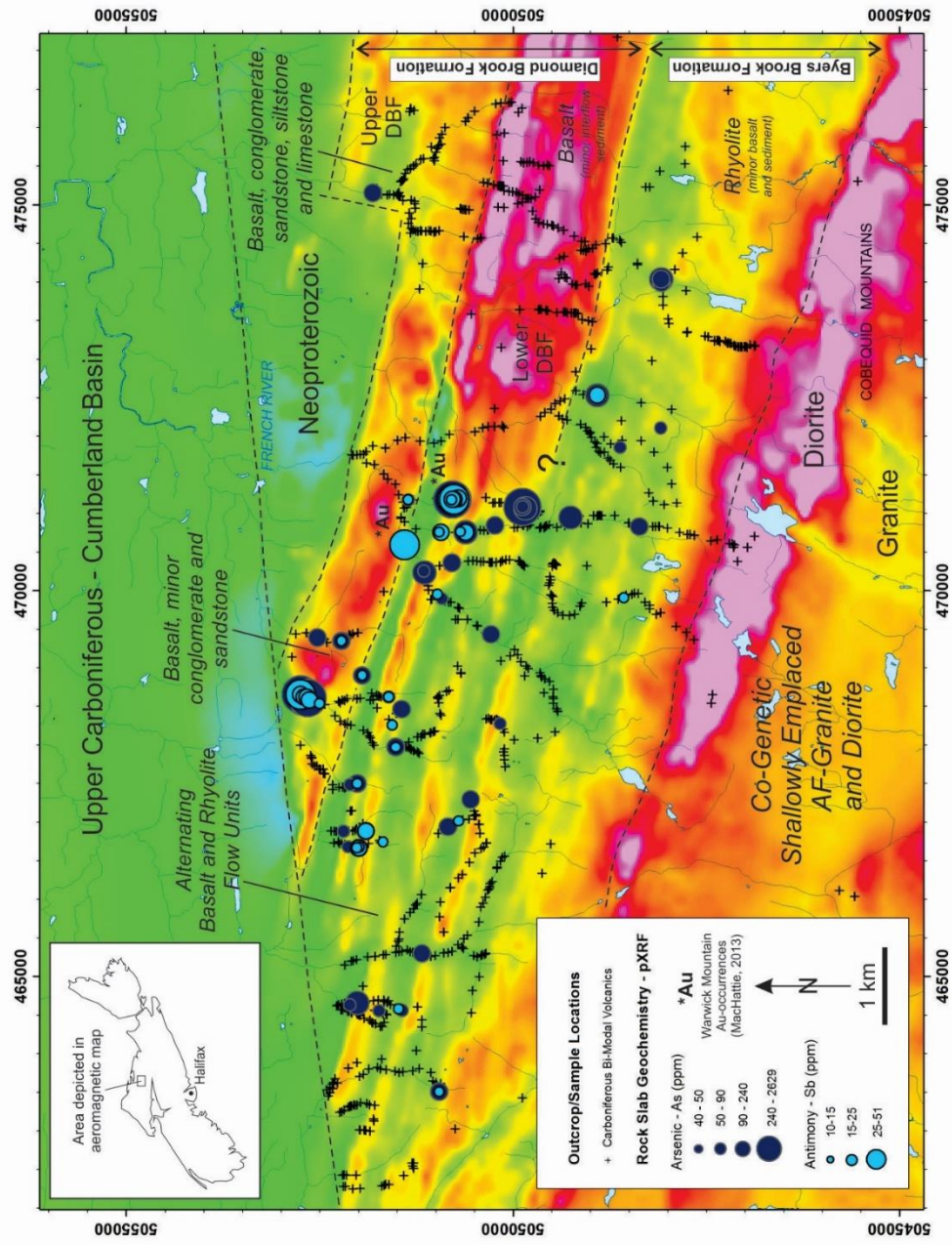
Figure 3 - Aeromagnetic map of the NW portion of the Byers Brook and Diamond Brook Formations. Bubble plots show As and Sb concentrations determined by portable XRF analysis on rock slabs and powders. Map modified from MacHattie, 2017.

11
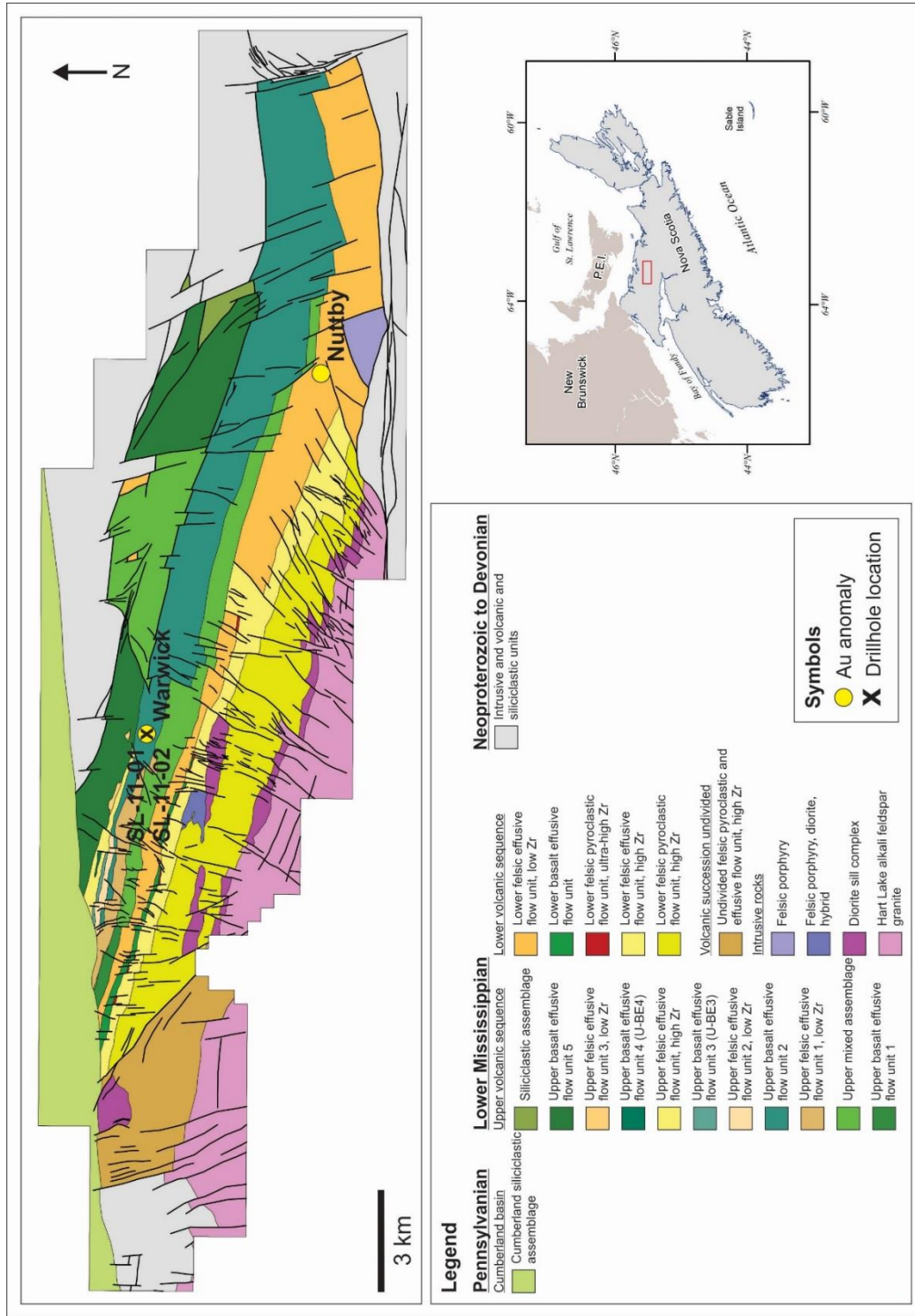
Figure 4 - Geological map of the Eastern Cobequid Highlands showing distinct units. Sample locations of study shown. Map modified from MacHattie, 2018.

3.0 Methods

3.1 Sample collection and preparation

Samples for this study were collected from the drill core (Sugarloaf Resources Ltd.) during the 2018 field season. Core was assessed at the Nova Scotia Department of Natural Resources storage facility in Stellarton, Nova Scotia. 27 polished thick sections were made at Vancouver Petrographics Ltd. These included 15 sections from Core 1 (DDH SL-11-01) from depths of 15.35 m to 129.8 m, and 12 sections from Core 2 (DDH SL-11-02) from depths of 12.35 m to 144.04 m. Surface samples collected during the 2011 field season by the NSDNR were also studied. 11 samples were selected for polished thick sections, including six from Warwick Mountain occurrence, two from Nuttby Mountain occurrence, two from approximately 850 m northwest of the Warwick Mountain locality in the upper basalt flow unit, and one from approximately 970 m northwest of Nuttby Mountain locality in the lower felsic flow unit.

3.2 Optical microscopy and scanning electron microscopy (SEM-BSE-EDS)

All samples were characterized petrographically in transmitted and reflected light using a Nikon Eclipse H550L microscope. All samples were carbon-coated and analyzed with a TESCAN MIRA 3 LMU VPS Field Emission Scanning Electron Microscope (SEM) at Saint Mary's University. The SEM is equipped with a silicon drift detector (SDD) and solid-state, 80 mm^2 X-max Oxford Instruments EDS detector was used. A beam voltage of 20 kV and routine working distance of 17 mm was applied for all imaging and analyses. SEM-EDS was used to characterize

the As content controlling different types of zoning in pyrite (observed as grey-scale variations in SEM-BSE images) and to identify other sulphide minerals present. Petrography and SEM-EDS were used as the basis to select specific pyrite grains for SIMS, LA-ICP-MS, and EMP analyses.

3.3 Bulk S isotopes

Analyses of the bulk S isotope composition of drill core samples was performed at the Queen's University Facility for Isotope Research, Kingston, Canada. Samples were weighed into tin capsules and the S isotope composition measured using a MAT 253 Stable Isotope Ratio Mass Spectrometer coupled to a CostechECS 4010 Elemental Analyzer. $\delta^{34}S$ values were calculated by normalizing the $^{34}S/^{32}S$ ratios in the sample to that in the Vienna Canyon Diablo Troilite (VCDT) international standard reference. Values are reported using the delta (δ) notation in units of permil (‰) and are reproducible to within 0.2 ‰.

3.4 In-situ S isotopes by secondary ion mass spectrometry (SIMS)

Analyses of in-situ S isotope compositions of pyrite and marcasite in-situ were conducted at the University of Manitoba, Canada using SIMS. Nine samples from Core 1 and Core 2 and two surface samples from Nuttby and Warwick Mountain occurrences were selected as showing distinct zoning variants observed by SEM-BSE. The sulphur isotope ratio ($^{34}S/^{32}S$) of pyrite grains was collected using a CAMECA 7f SIMS. A cesium (Cs^+) primary beam with a 3 nA current was accelerated (+10 kV) onto the sample surface with a sputtering diameter of ~25

μm. Riciputi et al. (1998) provide a detailed description of operating conditions and strategy for correction of instrumental mass fractionation and matrix effects. $\delta^{34}S$ values were calculated by normalizing the $^{34}S/^{32}S$ ratios in the sample to that in the Vienna Canyon Diablo Troilite (VCDT) international standard reference.

A pyrite sample with an accepted $\delta^{34}S$ value of 15.1 ± 0.3 ‰ from the Balmat metamorphosed massive sulphide deposit in Maine was used as the S isotope standard (Riciputi et al., 1998). Spot-to-spot reproducibility for Balmat pyrite was 0.3 ‰. Precision for individual analysis was 0.3 ‰ for $\delta^{34}S$ values. Therefore, the 1σ error for sulphur isotope analysis is 0.3. Results from the standards were compared to accepted isotopic compositions in order to calculate correction factors that were applied to the unknowns measured during the same analytical session (e.g., Holliger and Cathelineau, 1988). As content of pyrite was shown to not have a systematic bias on $\delta^{34}S_{VCDT}$ composition of pyrite as analyzed by SIMS for the range of As observed in the study samples.

3.5 *Laser ablation inductively coupled mass spectrometry (LA-ICP-MS)*

Pyrite trace element composition (single spots; n=57) and trace element distribution maps were determined by LA-ICP-MS at the University of New Brunswick, Canada using a Resonetics M-50 193 nm excimer laser system connected, via Nylon tubing, to an Agilent 7700x quadrupole ICP-MS equipped with dual external rotary pumps (McFarlane and Luo, 2012).

Samples and standards were loaded together into a two-volume, low-volume Laurin Technic Pty sample cell that was repeatedly evacuated and backfilled with

ultra-pure He to remove traces of air from the cell after each sample exchange. Spot ablations of pyrite were done using a 24 μm beam diameter at a 3 Hz repetition rate with the laser fluence regulated at ~3 J/cm^2. Spot ablations involved 30 s of transient signal collected from pyrite followed by 30 s of gas background collection. Pyrite trace element mapping used a 17 μm beam diameter, a stage scan speed of 6 μm/s, and a 10 Hz repetition with the laser fluence regulated at ~3 J/cm^2. A He carrier gas was used at a flow rate of 300 mL/min transported the ablated material out of the ablation cell and mixed downstream of the cell with 2 mL/min N_2 (to enhance sensitivity) and 930 mL/min Ar (from the ICP-MS) prior to reaching the ICP-MS torch. Oxide production rates were maintained below 0.3 %. Dwell times for all elements was 10 ms except for Au, Pt, and Pd which were 50 ms.

For spot analyses, a 'squid' smoothing device was used to ensure low %RSD signals; the 'squid' was removed for trace element mapping to ensure fastest possible washout duration from the cell (~3 orders of magnitude decrease in signal intensity in 1 s). Trace element concentrations in unknowns were calibrated against sulphide reference material MASS-1 (to calibrate analyte sensitivities) and an internal standard of 46.5 wt. % Fe for ideal pyrite. At the end of the ablation sequence, the laser log file and ICP-MS intensity data file were synchronized using Iolite™ (Paton et al., 2011) running as a plug in for Wave metrics Igor Pro 6.22™. Individual ablation signals were inspected offline and adjusted when necessary to avoid artifacts related to ablating through thin grains or from the beam ablating another mineral (e.g., silicates). Spikes in the data were automatically filtered using

the default 2σ outlier rejection in the Iolite internally- standardized trace-element data reduction scheme. For trace element maps, non-pyrite material was removed using the Fe CPS elemental map as a guide; concentration scales for each map portray internally standardized absolute ppm levels.

3.6 Electron microprobe

Electron microprobe analyses of pyrite were performed using a JEOL JXA8230 electron microprobe (EMP) at University of Toronto. The instrument was operating at 15 kV accelerating voltage with a 30 nA beam current for all analyses. The nominal beam diameter was 1 μm. Raw microprobe data count rates were converted to concentrations using the ZAF matrix correction scheme using the JEOL software.

High-resolution compositional maps of S, Fe, As, Au, and Cu were also collected using with the same equipment. Sulphur, Fe, As, Au, and Cu were collected on separate spectrometers at 15 kV, 50nA, with a focused beam and a dwell time of 45 ms on each pixel. Elemental map intensities were converted into concentrations using Fe as the internal standard at a value of 46.55 wt % Fe for ideal FeS_2.

4.0 Results

4.1 Host rock petrology and mineralogy

The samples from the core show a variety of textures of basalt and rhyolite. The samples from Core 1 were selected from intersections of massive, vesicular,

scoracious, and porphyritic basalt, and spherulitic rhyolite (Table 1; Figure 5). The samples from Core 2 were selected from intersections of massive, porphyritic, vesicular, scoracious, amygdular, and tuffaceous basalt, and spherulitic rhyolite (Table 1; Figure 6).

Seven samples were selected from Core 1 to demonstrate representative textures throughout the drill core. SL-11-01-82.82 is tuffaceous basalt, with quartz, calcite, and minor sulphides and hematization (Figure 7A-C). SL-11-01-108.95 is spherulitic rhyolite containing finely disseminated sulphides and showing extensive silicification (Figure 7D-E). SL-11-01-149.75 is tuffaceous rhyolite with a range in fragment dimensions (mm to cm scale) and showing extensive silicification (Figure 7G-I). SL-11-01-156.75 is vesicular basalt with chlorite-filled vesicles and pervasive silicification (Figure 7J-L). SL-11-01-168.98 is massive tuffaceous basalt containing few coarse tuffaceous fragments, and pervasive hematization. SL-11-01-172.1 is tuffaceous basalt with a large size range of fragments (Figure 7M-O).

Samples selected for S isotope and pyrite chemistry study (KG series) are highly altered, exhibiting silicification, chloritization, carbonatization, and hematization. Quartz is typically fine-grained and pervasive throughout the samples, but also exhibits unique colloform or comb-texture where space was sufficient (Figure 8A). Chlorite often occurs in veins, or infilling vesicles (Figure 8B). Carbonate is present predominantly as calcite veins (Figure 8C), with pervasive alteration throughout the sample. Where hematization occurred, it was typically pervasive throughout the sample, causing an overall burnt-red appearance (Figure 8D).

Table 1 - Sample summary and descriptions for core samples from Core 1 (18KG014 – 18KG028) and Core 2 (18KG01 – 18KG013).

Sample	Start (m)	End (m)	Length	Rock type	Texture	Mineralogy	Alteration
18KG001	15.22	15.33	0.11	Basalt	Massive, vein present	py (breaking down), qtz vein	sil, carb
18KG002	15.65	15.74	0.09	Basalt	Massive, vein present	py, ccp, chl, lm, cal (bladed), qtz (comb-texture)	sil, carb
18KG004A	17	17.35	0.35	Basalt	Porphyritic	py, ccp (fractures/edges), pl phenocrysts, chl	chl
18KG004B	36.29	36.58	0.29	Basalt	Massive	py, qtz, fractured mineral?	sil, hem, ser
18KG005	36.66	36.80	0.14	Basalt	Vesicular (vesicles infilled)	py, chl, fractured mineral?	chl, sil
18KG006	37.39	37.46	0.07	Basalt	Scoraceous, vesicles infilled	py, ilm?, qtz, chl (in fractures)	chl, sil
18KG008	63.6	63.75	0.15	Basalt	Amygdular, vein present	py, qtz (comb-texture/f-g), cal, chl	chl, sil, carb
18KG009	127.75	127.87	0.12	Basalt	Tuffaceous	py, qtz	sil
18KG010	131.75	131.90	0.15	Basalt	Massive, patches of scoraceous	py, qtz (comb-texture/colloform/f-g), feldspar	sil
18KG011	132.54	132.67	0.13	Basalt	Massive, patches of scoraceous	py, qtz (f-g and rhombic)	sil
18KG012	138.85	138.95	0.10	Basalt	Tuffaceous, coarse-grained	py, qtz (rhombic, chl, feldspar remnant	sil, chl
18KG013	142.9	144.04	1.14	Rhyolite	Spherulitic	py, qtz	sil
18KG014	15.35	15.45	0.10	Basalt	Highly vesicular (>0.5mm vesicles)	py, ilm? qtz, chl	sil, chl
18KG015	27.85	28.00	0.15	Basalt	Scoracious	py, ilm?, qtz, cb	sil, carb , chl
18KG016	40.7	41.10	0.40	Basalt	Scoracious, highly altered	py, ilm?, qtz, cb	sil, carb
18KG017	45.9	46.05	0.15	Basalt	Scoracious, highly altered	py, cb, qtz	sil, carb
18KG018	46.2	46.40	0.20	Basalt	Massive, brecciated	py, chl, qtz	chl, sil
18KG019	55	55.15	0.15	Basalt	Porphyritic, fine-grained	py, chl, feldspar remnants, qtz (f-g), ilm?	chl, sil
18KG020	65.15	65.35	0.20	Basalt	Vesicular	py (matrix/vug), qtz (f-g/comb-texture), chl, cb	sil, chl, carb
18KG021	84.8	85.10	0.30	Basalt	Vesicular (vesicles infilled)	py (matrix), chl, qtz, pl	sil, chl
18KG022	91.05	91.30	0.25	Basalt	Scoraceous	py (matrix and vug), qtz (vug), cb (vug), ilm?	sil, carb, hem
18KG023	109.25	109.35	0.10	Rhyolite	Spherulitic	py, qtz (comb-texture), ilm?	sil
18KG024	118.15	118.35	0.20	Rhyolite	Spherulitic	py, qtz (colloform/comb-texture)	sil
18KG025	117.8	118.00	0.20	Rhyolite	Spherulitic	py, qtz, ghosts of unknown minerals?	sil, hem
18KG026	120.3	120.50	0.20	Rhyolite	Spherulitic	py, qtz (colloform/f-g), ilm, cb	sil, carb
18KG027	124.35	124.50	0.15	Rhyolite	Spherulitic	py, qtz, feldspar remnant, vesicles infilled	sil
18KG028	129.65	129.8	0.15	Rhyolite	Spherulitic, flow banded	py, qtz (cockade?), ilm?	sil

Notes:
Mineralogy: cal = calcite, cb = carbonate, ccp = chalcopyrite, chl = chlorite, ilm = ilmenite, lm = limonite, pl = plagioclase, py = pyrite, qtz = quartz; f-g = fine-grained
Alteration types: sil = silicification, carb = carbonatization, chl = chloritization, hem = hematization, ser = sericitization

19
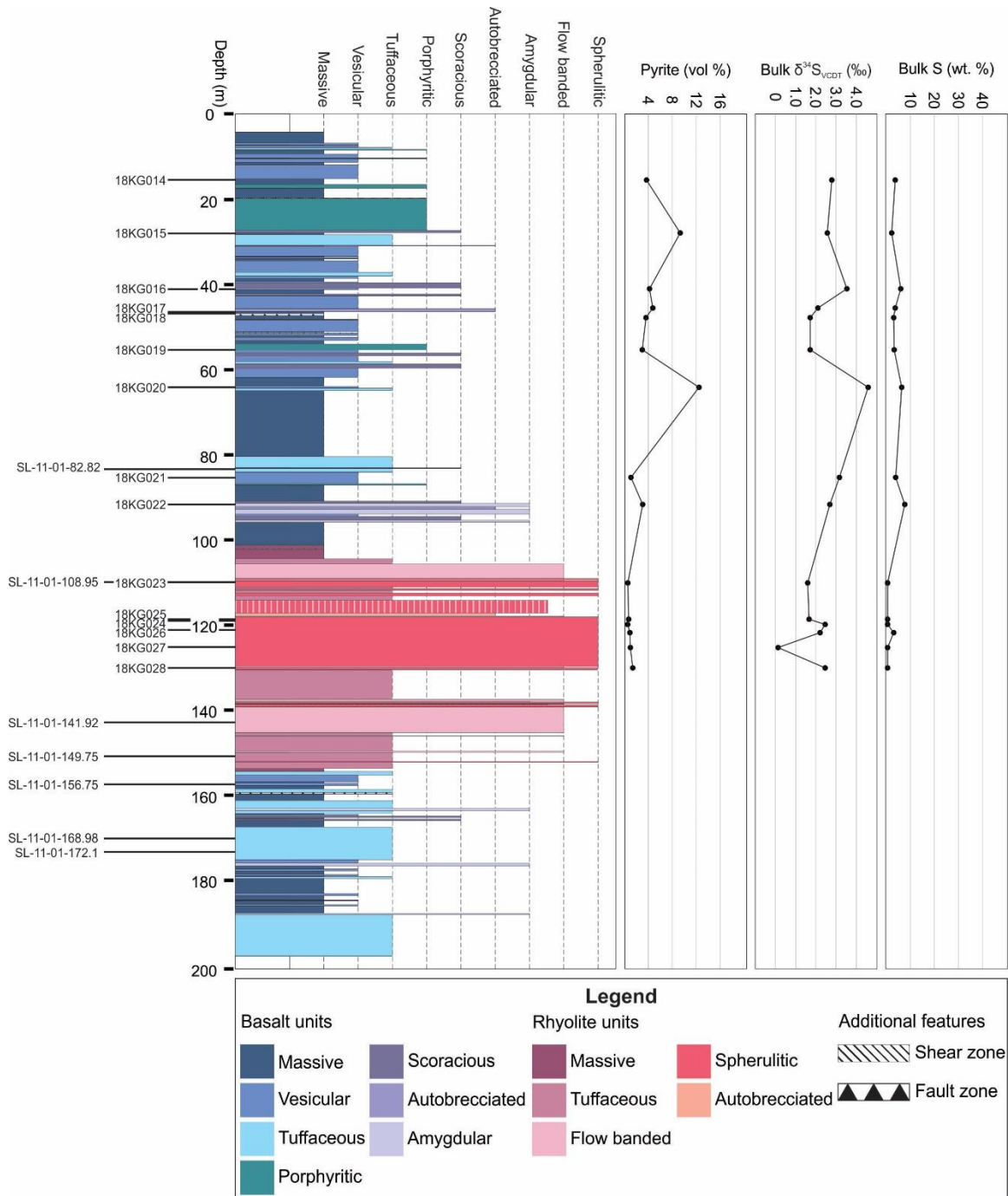
Figure 5 - Stratigraphic column of DDH SL-11-01 (Core 1) showing sample locations of thick sections used for analysis (KG series) and thin sections used for representative textures (SL-11-01 series). Corresponding bulk $\delta^{34}S_{VCDT}$, bulk S, and pyrite abundance shown.
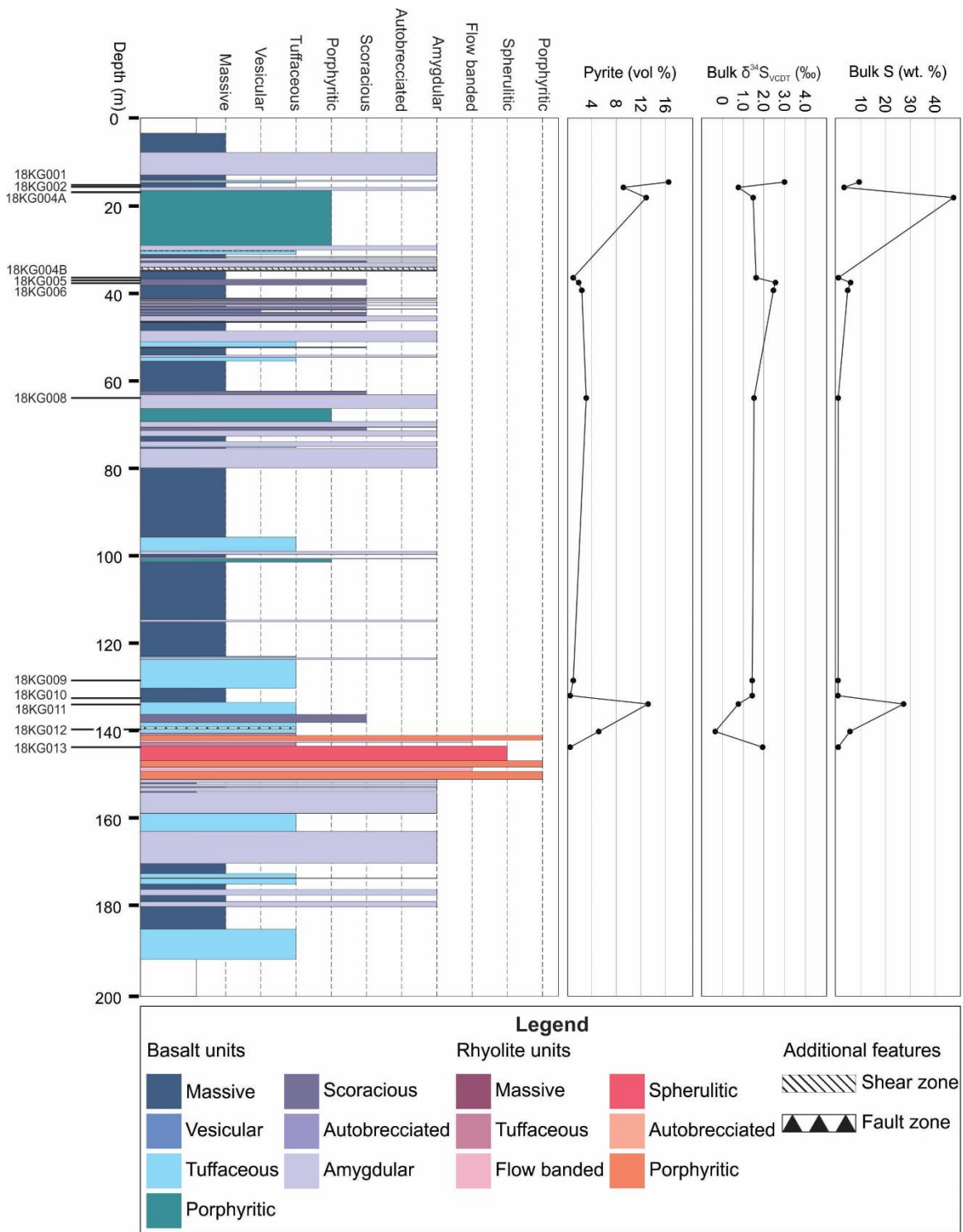
Figure 6 - Stratigraphic column of DDH SL-11-02 (Core 2) showing sample locations of thick sections used for analysis (KG series). Corresponding bulk $\delta^{34}S_{VCDT}$, bulk S, and pyrite abundance shown.
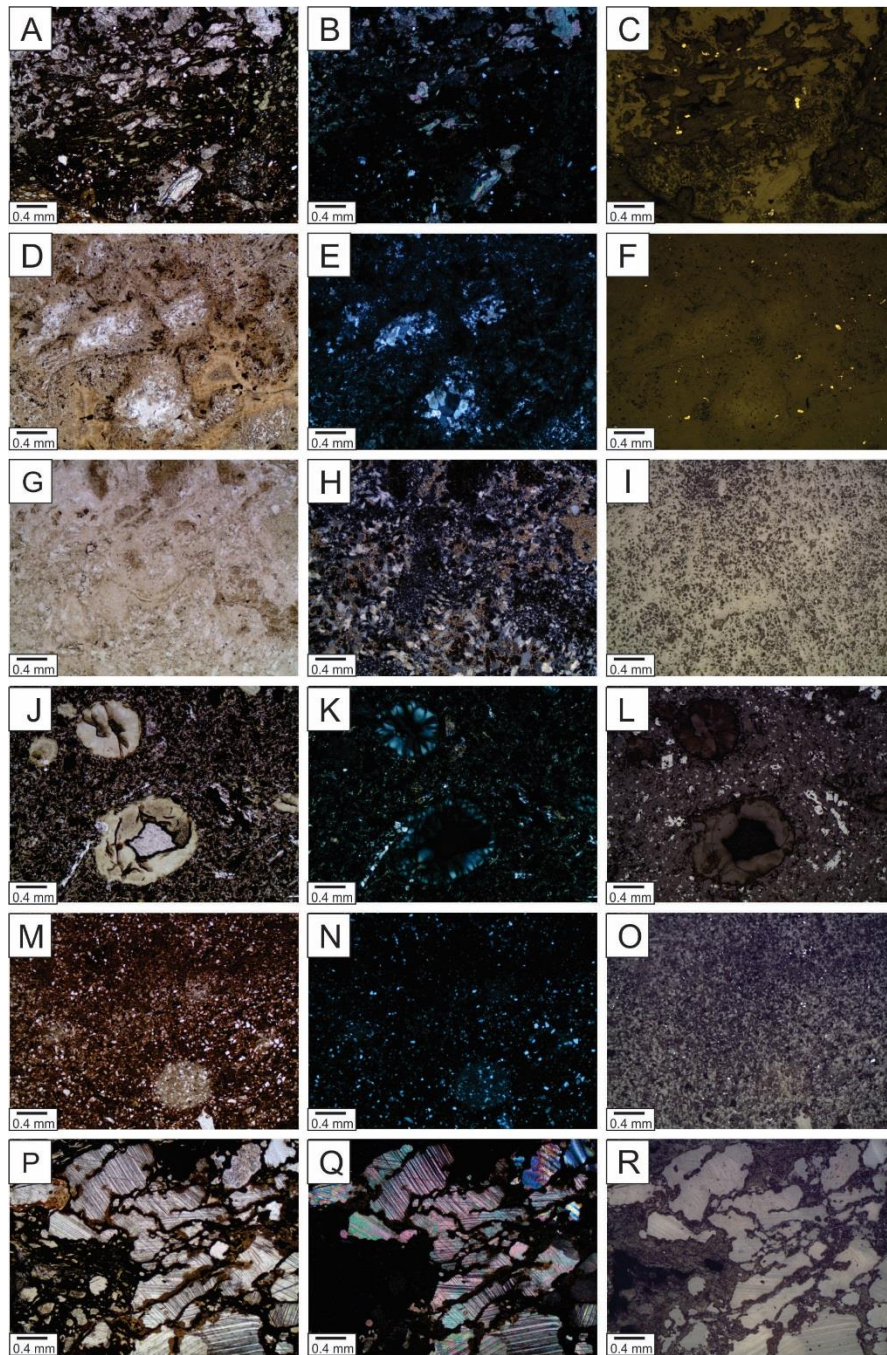
Figure 7 - Representative textures from DDH SL-11-01 series (Core 1). Images in left column were taken using transmitted plain polarized light, images in center column were taken using transmitted cross polarized light, images in right column were taken using reflected light. A-C) Tuffaceous basalt (SL-11-01-82.82). D-F) Spherulitic rhyolite (SL-11-01-108.95). G-I) Tuffaceous rhyolite (SL-11-01-149.75. J-L) SL-11-01-156.75. M-O) Massive basalt (SL-11-01-168.98). S-U) Tuffaceous basalt with scoria fragments (SL-11-01-172.1).
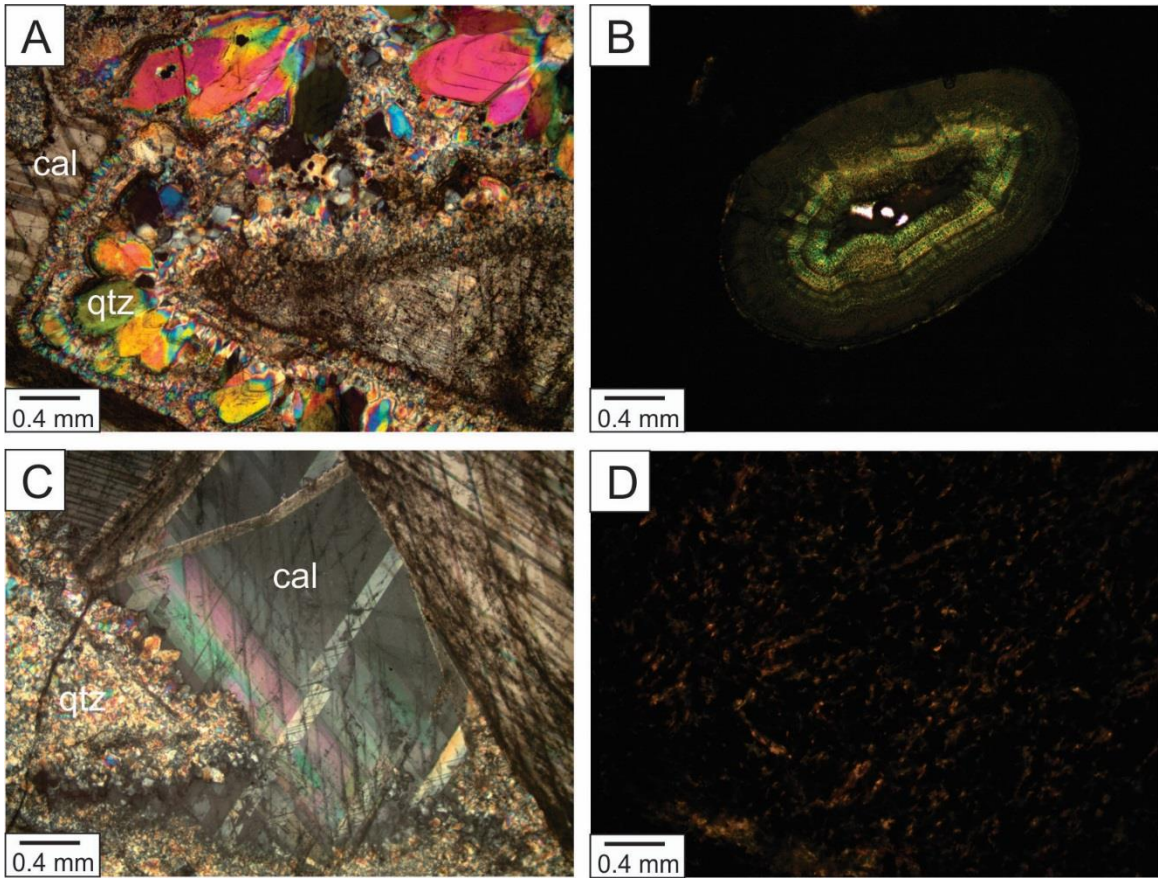
Figure 8 - Host rock mineralogy of Core 1 and Core 2 samples. All images captured in transmitted cross polarized light. A) Alternating plumose-texture quartz and comb-texture quartz. B) Chlorite infilling vesicle. C) Lattice-bladed calcite vein. D) Pervasive hematization of fine-grained volcanic matrix.

4.2 Sulphide mineralogy

The main sulphide minerals in the studied samples are pyrite, marcasite, galena, sphalerite, arsenopyrite, and chalcopyrite; with pyrite being the most abundant. Modal abundances of pyrite in the samples range widely from 0.1 to 25 volume %. In Core 1, pyrite is more abundant in the upper section of the drill core corresponding to mainly massive and vesicular basalts, and in smaller lenses in lower sections of the drill core, corresponding to massive basalt and tuffaceous rhyolite (Figure 5). Its abundance is lowest in flow banded and spherulitic rhyolite. In Core 2, pyrite is also predominantly concentrated in the upper section of the drill core corresponding to massive and porphyritic basalt, and in smaller lenses in lower sections of the drill core, corresponding to amygdular and massive basalt (Figure 6).

Galena, sphalerite, and arsenopyrite occur as inclusions within pyrite, infilling fractures in pyrite, as overgrowths on early pyrite, and as separate, isolated grains (Figure 9). Galena most commonly occurs infilling thin, extensive fracture networks in pyrite grains (Figure 9A). More rarely, it occurs in sieve-textured pyrite, sometimes associated with distinct concentric growth rings (Figure 9B). Galena also commonly infills open spaces within pyrite grains, allowing for a higher abundance of galena to form (Figure 9C-D). Chalcopyrite is present as individual grains scattered throughout the samples, often closely associated with clusters of pyrite (Figure 9D). Sphalerite is also present as individual grains dispersed throughout the samples, sometimes uniquely demonstrating zoning patterns controlled by its Cd content (Figure 9E-F). Arsenopyrite is found in only a few

24

samples, but is abundant when it is present. Pyrite in these samples is extensively fractured, with arsenopyrite commonly infilling these fractures (Figure 9G). It also nucleated on pyrite rims (Figure 9H-I), showing partial replacement of pyrite by arsenopyrite. Marcasite occurs in few samples as variably fractured, diamond-shaped grains or grain aggregates. Generally, textural evidence suggests that these other sulphides are late with respect to pyrite, mainly infilling porosity or fractures in pyrite, or partial replacement of pyrite.
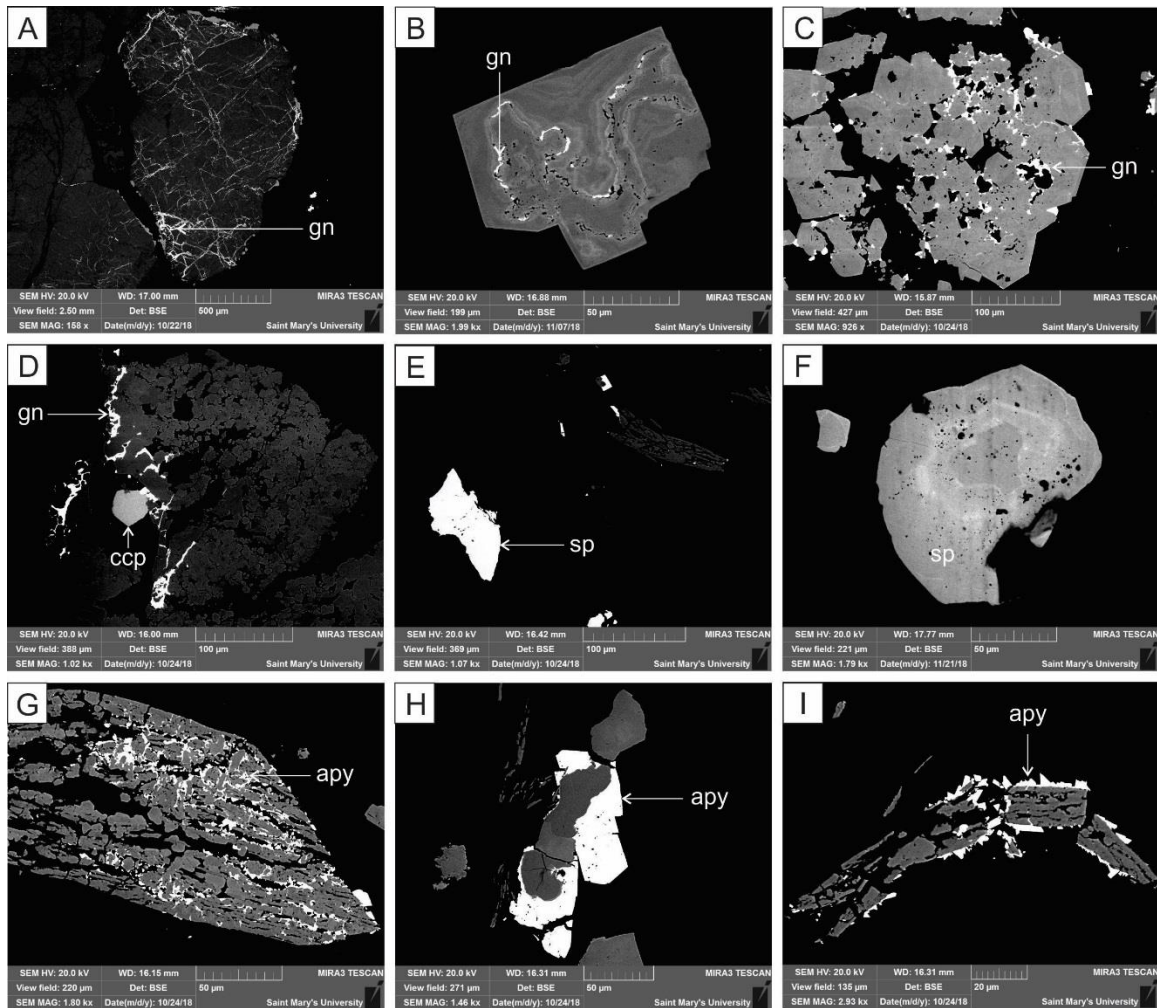
Figure 9 - SEM-BSE images of associated minerals. A) Galena infilling fractures in pyrite. B) Galena associated with zoned pyrite growth. C) Galena grains precipitating in open spaces in pyrite. D) Galena infilling fractures in pyrite, and chalcopyrite grain on edge. E) Individual sphalerite grain hosted in matrix. F) Zoned sphalerite grain. G) Arsenopyrite infilling fractures in pyrite. H) Euhedral arsenopyrite grains growing on the rim of pyrite grains. I) Euhedral arsenopyrite grains growing on the rim of pyrite grains.

4.3 Pyrite morphology and zoning classification

Pyrite morphology was characterized using several criteria, broken down into categories including single grain vs. cluster, cubic vs. non-cubic (with a respective descriptor), and euhedral vs. anhedral (Table 2 and Table 3). Grain size of individual grains ranged from 20 µm to 1 mm. Individual grains were typically non-cubic euhedral grains, most often categorized as either clean or sieve (Figure 10A and Figure 10B, respectively). Pyrite infrequently occurred throughout samples as cubic (or close to cubic) grains and exhibited sieve textures (Figure 10C-D). In one sample, diamond-shaped grains with both clean and fractured surfaces were identified to be marcasite based on anisotropism in reflected, cross-polarized light (Figure 10E and Figure 10F, respectively). In two samples, pyrite occurred as highly fractured individual bladed grains or radiating clusters of grains (Figure 10G-H). Grain size of bladed grains ranged from 100 µm to 500 µm. Although pyrite predominantly occurred as individual grains typically isolated in the matrix, it was often closely surrounded by other individual grains in the matrix (Figure 10I-J). Pyrite also commonly occurred as clusters, appearing as if several grains grew together and exhibiting extensive fracturing and sieve texture (Figure 10K-L). Clusters ranged in size from 100 µm to several mm.

The top of Core 1 is a basalt unit and contains nine of the samples studied. The first two sample contain mainly small individual euhedral grains with a notable amount of medium size grains closely related in agglomerations (Figure 11A). A unique sample around 46 m shows diamond-shaped grains, identified as marcasite (Figure 11B). The next units contain pyrite grains in clusters and as

individual euhedral grains. The remainder of the samples in Core 1 are from the rhyolite unit, and contain very minimal pyrite occurring as small individual euhedral grains disseminated in the matrix (Figure 11C). The top of Core 2 is a basalt unit dominated by pyrite in bands and clusters (Figure 11D-E), with a less significant amount of small individual euhedral grains disseminated in the matrix. The remainder of the top basalt unit is dominated by small individual euhedral pyrite grains disseminated in the matrix (Figure 11F). There is a unique section around 127 m – 132 m showing bladed and radiating pyrite grains (Figure 11G). The remainder of the rhyolite unit contains medium-sized individual subhedral grains (Figure 11H). The final sample from Core 2 is from a basalt unit and contains small individual euhedral grains disseminated in the matrix (Figure 11I).

Table 2 - General petrography and textural features of pyrite in Core 1 and Core 2 based on optical microscopy.

Sample	Pyrite (vol%)	Grain morphology cl / sg	c / n-c	description	eu - an	location	Size (um)	Notes
18KG001	16.56	cls	n-c	sv/frac	an	???	4-40	
		sg	n-c	cln	eu	Vein	1	
18KG002	9.02	cls/sg	n-c	frac/sv	eu/sub	mx	cl=5-50; sg=2-10	clusters appear eaten away
		sg (minor cls)	n-c	cln	sub	mx	10-1.0	py only assc. w/ host rock
		sg	n-c	cln	eu	vein	<1	v. minimal grains
18KG004A	12.62	sg(s)	n-c	frac/sv	sub	cav (min. mx)	30-100	py grains fractured
		sg	n-c	frac	an	mx	02-10.0	v. minimal py; v. frac/eaten away
18KG004B	1.00	sg	n-c	cln?	eu-an	mx	lg=1-5; sm=<1	lg = eu / sm = an
						ves		v. sm amount
18KG005	2.15	sg	n-c	cln?	eu (min.sub)	mx	lg=1-5; sm=<1	sm= diamond shaped?
18KG006	2.46	sg	n-c	cln	eu	mx	lg=1-5; sm=<1	
18KG008	3.57	cls (min. sg)	n-c	cln/sv	cl=an / sg=eu	mx	cl=5-15; sg=1-5	lg frac eu. grain, edges eaten away
18KG009	1.34	sg (min. cls)	n-c	bld/rad	sub (bladed)	mx	<1 - 10	bld grains
18KG010	0.38	sg (min. cls)	n-c (min. c)		sg=eu / cl=an	mx?		cls/eaten away around edges
18KG011	12.82	cls	n-c	rad/frac	an	mx	sg= 1-10; rad=10-150	bld/rad grains v. fractured
18KG012	5.45	sg	n-c	frac/sv	an	mx	1.0-40	v. eaten away
18KG013	0.73	sg	c	cln	eu	mx	1.0-3; up to 5	
18KG014	3.95	sg	n-c	cln (sv)	eu	mx	1.0-10; up to 15	
18KG015	9.11	cls (min. sg)	n-c	cln	sub	cav	1.0-15	
18KG016	4.04	sg(s)	n-c	sv	an	mx	1.0-50	py eaten away
18KG017	4.86	sg(s)	n-c	sv	eu - an	mx	1.0-50	sm grains in bands (min lg eu. grains)
18KG018	3.88	sg	n-c	sv	sub	mx	1.0-15	
18KG019	3.29	cls	n-c	sv	an	mx		Hard to give size to, often in bands
18KG020	12.57	sg(s) / cls	n-c	cln?	eu (min. sub)	mx	sg= 5-20; cl= 10-60	
18KG021	1.40	sg(s)	n-c	diamond	an	mx	1.0-5.0	v. eaten away; in cavities/cracks?
18KG022	3.04	sg(s)	n-c	frac	an (minor eu)	mx	1.0-5.0; up to 50	Generally sm; more eaten away
			n-c	cln (min. sv)	eu	ves	5.0-15.0	
18KG023	0.38	sg	n-c	sv	eu (min. an)	mx	mostly <1, up to 5	very min. py
18KG024	0.14	sg	n-c (min. c)	cln	eu (min.an)	mx	Mostly <1	extremely min. py
18KG025	0.50	sg	n-c (min. c)	cln	eu (min.sub)	mx	mostly <1; up to 5	min. py
18KG026	1.05	sg	n-c	cln (min. rad)	eu (min.sub)	mx	mostly <1; up to 5	min. py
18KG027	1.12	sg	n-c	cln	eu (min.sub)	mx	mostly <1; up to 5	min. py
18KG028	1.33	sg	n-c (min. c)	cln (min. sv)	eu	mx	mostly <1; up to 5	min. py

Notes:

cls = cluster, sg = single grain, sg(s) = single grains

c = cubic, n-c = non-cubic

cln = clean, sv = sieve, frac = fractued, bld = bladed, rad = radiating

eu = euhedral, sub = subhedral, an = anhedral

cav = cavity, mx = matrix, ves = vesicle

lrg = large, sm = small

py = pyrite

Table 3 - Detailed petrography and textural features of individual pyrite occurrences in Core 1 and Core 2 based on scanning electron microscopy in preparation for SIMS analysis.

Sample	Image	sg / cl	c / n-c	description	eu - an	location	Zoning type	Grain (um) x	Grain (um) y	Zone (um) x	Zone (um) y	Notes
18KG001	1	cls?	n-c	cln?	eu		core	130	105	2		gn grain
	2	N/A	N/A	N/A								gn - edges/frac
	3	cls?	n-c	frac/sv	an	mx?	mass	230	160	~10-30	~10-30	
	4	cls?	n-c	frac/sv	an	mx?	mass	370	345	330	265	gn infilling vug
	5	cls?	n-c	cln	eu	cav?	core/rim	140	70	5		
	6	cls?	n-c	frac	an	cav?	core					
	7	cls?	n-c	cln	eu	mx?	core	60	45	3		
18KG002	N/A	N/A	N/A	N/A	N/A	N/A	N/A					No zoning
18KG004A	1	N/A	N/A	N/A	N/A	N/A	N/A					gn - frac, ccp - edges
	2	cls?	n-c	frac	an	mx?	mass			110	90	Dark = ilmenite; light = gn
18KG004B	1	sg?	n-c	frac	eu	mx?	conc (osc)	55	25			
	2	sg	n-c	frac	eu	mx?	mass	55	35			gn (?) inclusion
18KG005	1	sg	n-c	sv	sub	mx	mass	105	65	10		
	2	sg(s)	n-c	cln/frac	eu	mx	conc (osc)	85	55	5		
	3	sg	n-c	cln/sv	eu	mx	core	185	85	60	80	
	4	sg	n-c	cln/frac	eu	mx	core	45	45	10		
	5	sg	n-c	cln	eu	mx	core	110	80	10		
	6	sg	n-c	cln	eu	mx	rim?	80	80	10		
	7	sg	n-c	cln	eu	mx	core					
	8	sg	n-c	cln	eu	mx	core					
18KG006	1	sg	n-c	cln/frac	eu	mx	core	85	60	3		
	2	sg	n-c	cln/sv	eu	mx	rim					
	3	sg(s)	n-c	cln	eu	mx	core					
	4	sg(s)	n-c	cln	eu	mx	core					
	5	sg(s)	n-c	cln/sv	eu	mx	core					
	6	sg	n-c	cln	eu	mx	core					
	7	sg	n-c	cln/sv	eu	mx	core	210	190	25		
	8	sg	n-c	cln	eu	mx	core	90	105	13		
	9	sg(s)	n-c	cln/sv	eu	mx	core	85	75	65	60	
	10	sg	n-c	cln/sv	eu	mx	core	90	90	55	70	
18KG008	1	sg	n-c	?	an	ves?	core	115	140	17?		
	2	N/A	N/A	N/A	N/A	N/A	N/A					
	3	sg	n-c	cln/sv?	eu		core	100	95	5?		
	4	sg	n-c	cln/sv?	eu		rim					
	5	sg	n-c	cln/sv?	eu	mx	core	115	120			

Table 3 (con't) - Detailed petrography and textural features of individual pyrite occurrences in Core 1 and Core 2 based on scanning electron microscopy in preparation for SIMS analysis.

Sample	Image	Grain morphology sg/cl	c/n-c	description	eu-an	location	Zoning type	Grain (um) x	Grain (um) y	Zone (um) x	Zone (um) y	Notes
	6	N/A	N/A	N/A	N/A	N/A	N/A					
	7	cls?	n-c	sv	eu	mx	core	310	225			
	8	cls?	n-c	sv	eu	mx	rim					
	9	sg	n-c	cln	eu	mx	rim					
	10	sg	n-c	cln	eu	mx	rim	100	110			
	11	cls?	n-c	sv	eu	mx	rim					gn inclusions
	12	sg	n-c	sv	eu	mx	conc (osc)	105	180			
18KG010T	1	N/A	N/A	N/A	N/A	N/A	N/A					apy; V high As! Minor Sb
	2	cls?	n-c	rad	an	mx	mass	310	35			
	3	cls?	n-c	rad	an	mx	mass					apy around py
	4	cls?	n-c	rad	an	mx	mass					apy around py
	5	cls?	n-c	rad	an	mx	mass					apy around py
	6	N/A										sph grain
18KG010T	1	cls?	n-c	frac/sv	an		mass					ccp, gn (brightest)
18KG011	1	cls?	n-c	frac	an							apy infilling fractures
	2	N/A	N/A	N/A								rad py with apy in frac
	3	N/A	N/A	N/A								
18KG012	N/A	N/A	N/A	N/A	N/A	N/A	N/A					No zoning
18KG013	1	sg	c?	sv	eu	mx	rim	30	50			
	2	sg	c?	cln	eu	mx	rim	60	200			
	3	sg	c?	cln	eu	mx	rim					
	4	sg	n-c	sv	sub	mx	rim	125	225	20-40		
	5	sg	c?	sv	eu	mx	osc	105	120			gn inclusions
	6	sg(s)	n-c	cln	eu	mx	osc	50	75			Cubic - no zoning
	7	cls?	n-c	cln/frac	eu	mx	core	50	200			
18KG014	1	sg	n-c	sv	eu	mx	osc (rim)	500	270	20-80		
	2	sg	n-c	sv	eu	mx	osc (rim)	370	270	60		
	3	sg	n-c	sv	eu	mx	osc (rim)	220	150	30?		
	4	sg	n-c	sv	eu	mx	osc (rim)					
	5	sg(s)	n-c	sv	eu	mx	osc (rim)			6		grains grown together?
	6	cls?	n-c	sv	eu	mx	osc (rim)			25		grains grown together?
	7	sg	n-c	cln	eu	mx	osc (rim)					
18KG015	1	cls?	n-c	cln/sv	eu	mx	osc			18-30		
	2	cls?	n-c	cln/sv	eu	mx	osc			10-20.0		
	3	cls?	n-c	cln/sv	eu	mx	osc					gn grain
	4	cls?	n-c	cln/frac	eu	mx	osc			10		
	5	sg	n-c	cln/sv	eu	mx	osc			25-30		
	6	cls?	n-c	cln/sv	eu	mx	osc					

31

Table 3 (con't) - Detailed petrography and textural features of individual pyrite occurrences in Core 1 and Core 2 based on scanning electron microscopy in preparation for SIMS analysis.

Sample	Image	Grain morphology		description	eu - an	location	Zoning type	Grain (um)		Zone (um)		Notes
		sg / cl	c / n-c					x	y	x	y	
18KG016	1	sg(s)	n-c	sv	eu	mx	core					
	2	cls?	n-c	sv	an	mx	core					
	3	sg(s)	n-c	sv	an	mx	core					
	4	sg(s)	c	sv	an	mx	core					
	5	sg(s)	n-c	sv	an	mx	core/mass					
	6	sg(s)	n-c	sv	an	mx	core/mass					
	7	sg(s)	n-c	sv	an	mx	core/mass					
18KG017	1	sg	n-c	sv	an	mx	core					
	2	cls?	n-c	frac/sv	an	mx	core					
	3	sg	n-c	sv	an	mx	core					
	4	sg	n-c	sv	an	mx	core					
	5	sg	n-c	cln/sv	eu	mx	rim					
	6	sg	n-c	frac	sub	mx	box			33		
	7	sg	n-c	cln/sv	eu	mx	rim					
	8	sg	n-c	cln/sv	eu	mx	box					Lead?
	9	sg	n-c	cln/sv	eu	mx	core					
	10	sg	n-c	cln/sv	eu	mx	rim					
18KG018	1	sg	n-c	frac	eu	mx	core					gn
	2	sg	n-c	frac	eu	mx	rim?					
	3	sg	n-c	diamond	eu	mx	core					
	4	sg	n-c	sv	sub	mx	rim?					
	5	sg	n-c	frac	eu	mx	core					
	6	sg	n-c	diamond	eu	mx	core					
18KG019	1	cls?	n-c	frac/sv	sub	mx	box					
	3	sg	n-c	cln/sv	eu	mx	rim? box					
	4	cls?	n-c	frac	sub	mx	box					
18KG020	1	sg	n-c	cln/frac	eu	mx	rim?			9		gn grains
	2	sg	n-c	cln	eu	mx	osc?					
	3	sg	n-c	cln/sv	eu	mx	rim					
	4	sg	n-c	cln/frac	eu	mx	rim					
	5	sg	n-c	cln/sv	eu	mx	conc					
	6	sg	n-c	cln/frac	eu	mx	box					
	7	sg	n-c	cln	eu	mx	conc					
	8	cls?	n-c	sv	an	Vein?	box					
	9	sg	n-c	cln	eu	mx	conc					
	10	sg	n-c	frac	eu	mx	core					
18KG021	1	cls?	n-c	sv	an	mx	?					
18KG022	N/A	N/A	N/A	N/A	N/A	N/A	N/A					No zoning

32

Table 3 (con't) - Detailed petrography and textural features of individual pyrite occurrences in Core 1 and Core 2 based on scanning electron microscopy in preparation for SIMS analysis.

Sample	Image	Grain morphology		description	eu - an	location	Zoning type	Grain (um)		Zone (um)		Notes
		sg / cl	c / n-c					x	y	x	y	
18KG023	1	sg	n-c	sv	eu	mx	rim					
	2	sg	n-c	sv	eu	mx	core					
	3	sg	n-c	sv	eu	mx	rim					gn inclusion
	4	sg	n-c	sv	eu	mx	rim					
	5	sg	n-c	sv	eu	mx	rim					
	6	sg	n-c	sv	eu	mx	rim					
18KG024	1	sg	n-c	sv	an	mx	conc (rim)					
	2	sg	n-c	sv	an	mx	conc (rim)					
	3	N/A	N/A	N/A	N/A	N/A	N/A					sph - zoned?
18KG025	1	sg	n-c	sv	eu	mx	rim?					
	2	sg(s)	n-c	sv	eu	mx	banded					
	3	sg(s)	n-c	sv	eu	mx	rim					
	4	sg(s)	n-c	sv	eu	mx	rim					
18KG026	1	sg	n-c	sv	eu	mx	rim					sph grain
	2	sg(s)	n-c	sv	eu	mx	rim					
	3	cls?	n-c	sv	an	mx	rim					
	4	Single		sv	eu	mx	rim					
18KG027	1	sg(s)	n-c	sv	eu	mx	rim					gn inclusion
	2	cls?	n-c	sv	eu	mx	rim					
	3	cls?	n-c	sv	eu	mx	rim					
	5	sg(s)	n-c	sv	eu	mx	rim					
	6	sg(s)	n-c	sv	eu	mx	rim					
18KG028	1	sg(s)	n-c	sv	eu	mx	rim					gn inclusion
	2	sg(s)	n-c	sv	eu	mx	rim					
	3	sg(s)	n-c	sv	eu	mx	core					
	4	sg(s)	n-c	sv	eu	mx	rim					gn inclusion, "ring"
	5	sg(s)	n-c	sv	eu	mx	rim					
	6	sg(s)	n-c	sv	eu	mx	rim					

Notes:

Grain morphology: cl = cluster, sg = single grain, sg(s) = single grains

c = cubic, n-c = non-cubic

cln = clean, sv = sieve, frac = fractued, rad = radiating

eu = euhedral, sub = subhedral, an = anhedral

cav = cavity, mx = matrix, ves = vesicle

mass = massive, conc = concentric, osc = oscillatory, box = boxwork

lrg = large, sm = small

py = pyrite, ccp = chalcopyrite, apy = arsenopyrite, gn = galena, sph = sphalerite

33
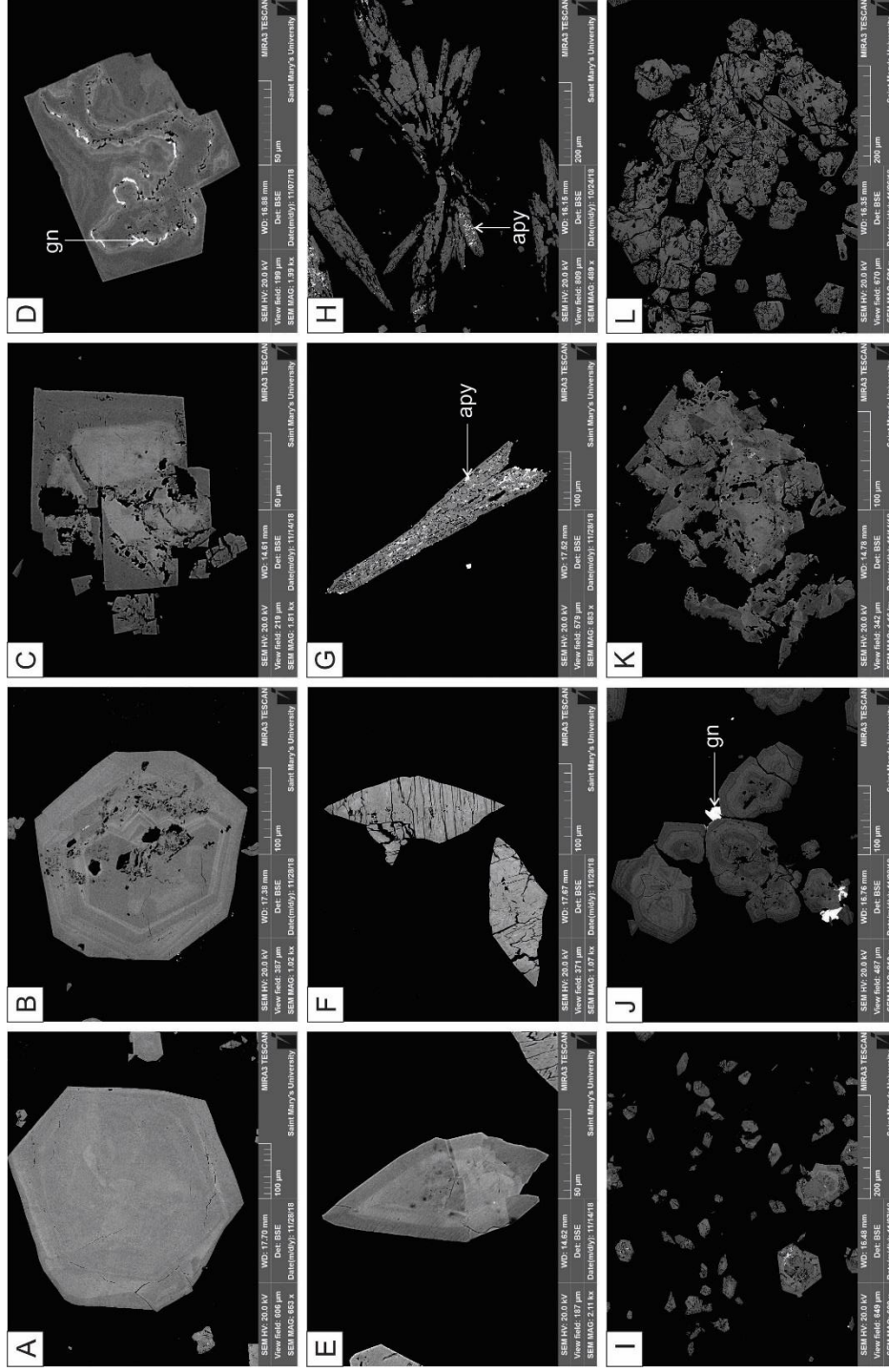
Figure 10 - Scanning electron microscope backscattered electron (SEM-BSE) images of representative pyrite (or marcasite) grain types. A) Euhedral pyrite. B) Euhedral pyrite with sieve texture. C) Cubic pyrite with sieve texture. D) Cubic pyrite with pervasive fracture and sieve texture. E) Diamond-shaped marcasite. F) Diamond-shaped marcasite with fractures. G) Bladed pyrite with arsenopyrite infilling fractures. H) Radiating pyrite with arsenopyrite infilling fractures. I-J) Clusters of single grains of pyrite. K-L) Clustered pyrite with pervasive fracturing and sieve texture.

34
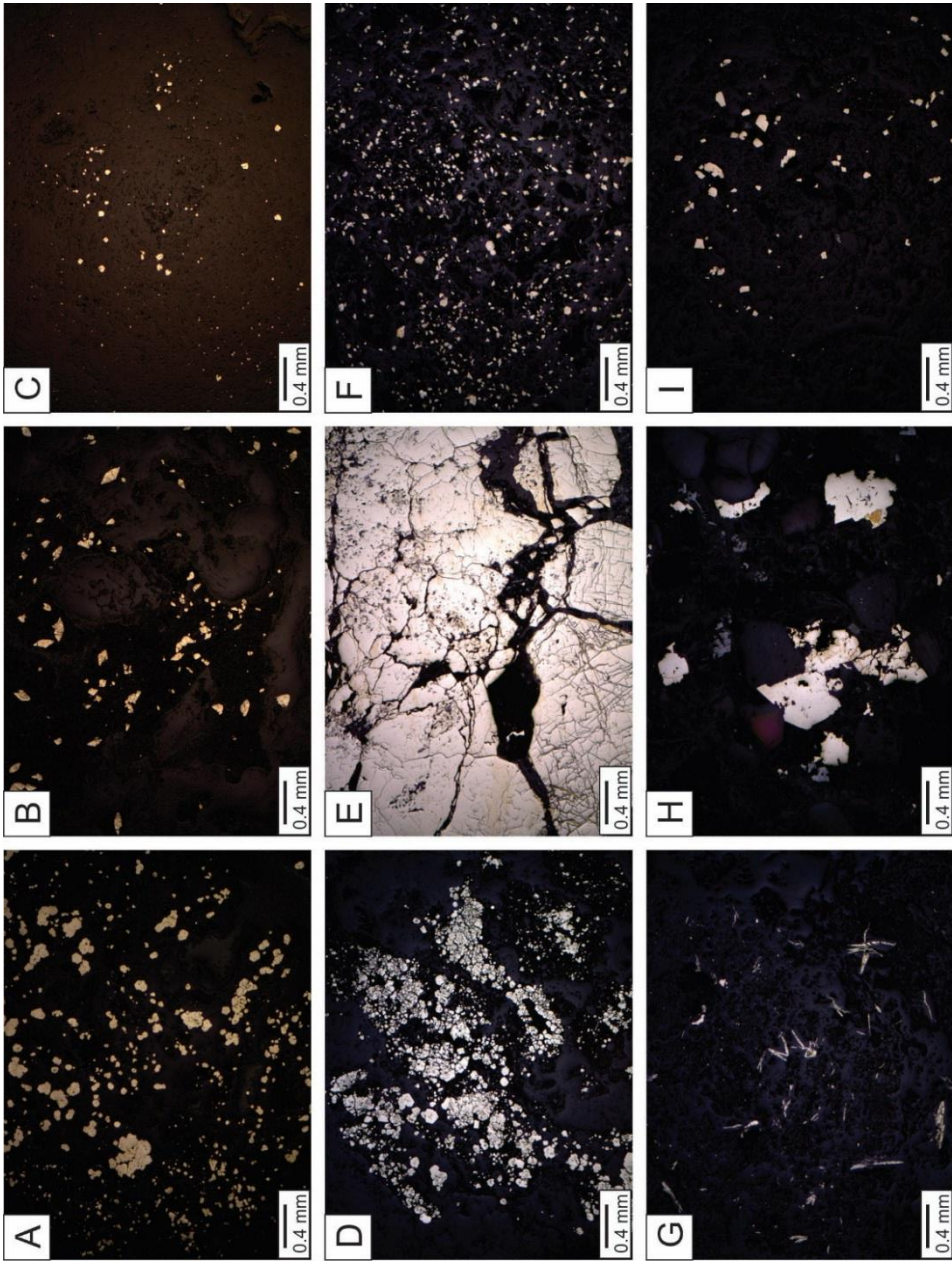
Figure 11 - Representative pyrite textures from Core 1 (A-C) and Core 2 (D-I). All images captured using 4x magnification. A) Small individual euhedral grains with medium size grains closely related in agglomerations. B) Diamond-shaped marcasite grains. C) Small individual euhedral grains disseminated in basalt. D) Varying sized pyrite in bands. E) Clusters of large grained, highly fractured pyrite. F) Small euhedral pyrite grains disseminated in basalt. G) Bladed and radiating pyrite grains. H) Medium-sized individual subhedral grains. I) Small euhedral grains disseminated in rhyolite.

4.4 Chemical and isotopic composition of pyrite

4.4.1 Arsenic zonation

Through extensive SEM-EDS analyses of all samples, strong arsenic zoning was identified in pyrite and classified as "core", "rim", "boxwork", or "massive". Core zoning was characterized by an anomalous concentration of arsenic within the interior of a grain, followed by a rim with minimal to no arsenic enrichment (Figure 12A-B and Figure 13A-C). Thickness of core zones ranged from 5 μm to 65 μm. Rim zoning was characterized by an arsenic free interior with a concentric ring around the edge of a grain, and in some cases several concentric rings, with an anomalous concentration of arsenic (Figure 12C-D and Figure 13D-F). Thickness of rim zones ranged from 1 μm to 60 μm. A unique style of zoning classified as boxwork zoning showed arsenic enrichment in a cross-hatched pattern, and was identified predominantly in surface samples (Figure 12E-F). Massive zoning was characterized by non-uniform concentrations of arsenic throughout pyrite (Figure 13G-I). Thickness of massive zones ranged from 10 μm to 330 μm. Anomalous arsenic concentrations in the zones in pyrite ranged from 0 to 9.02 wt. %. Rim and core zoning occurred predominantly in individual grains and rarely in small clusters, while massive and boxwork zoning occurred predominantly in clusters and less often in individual grains.
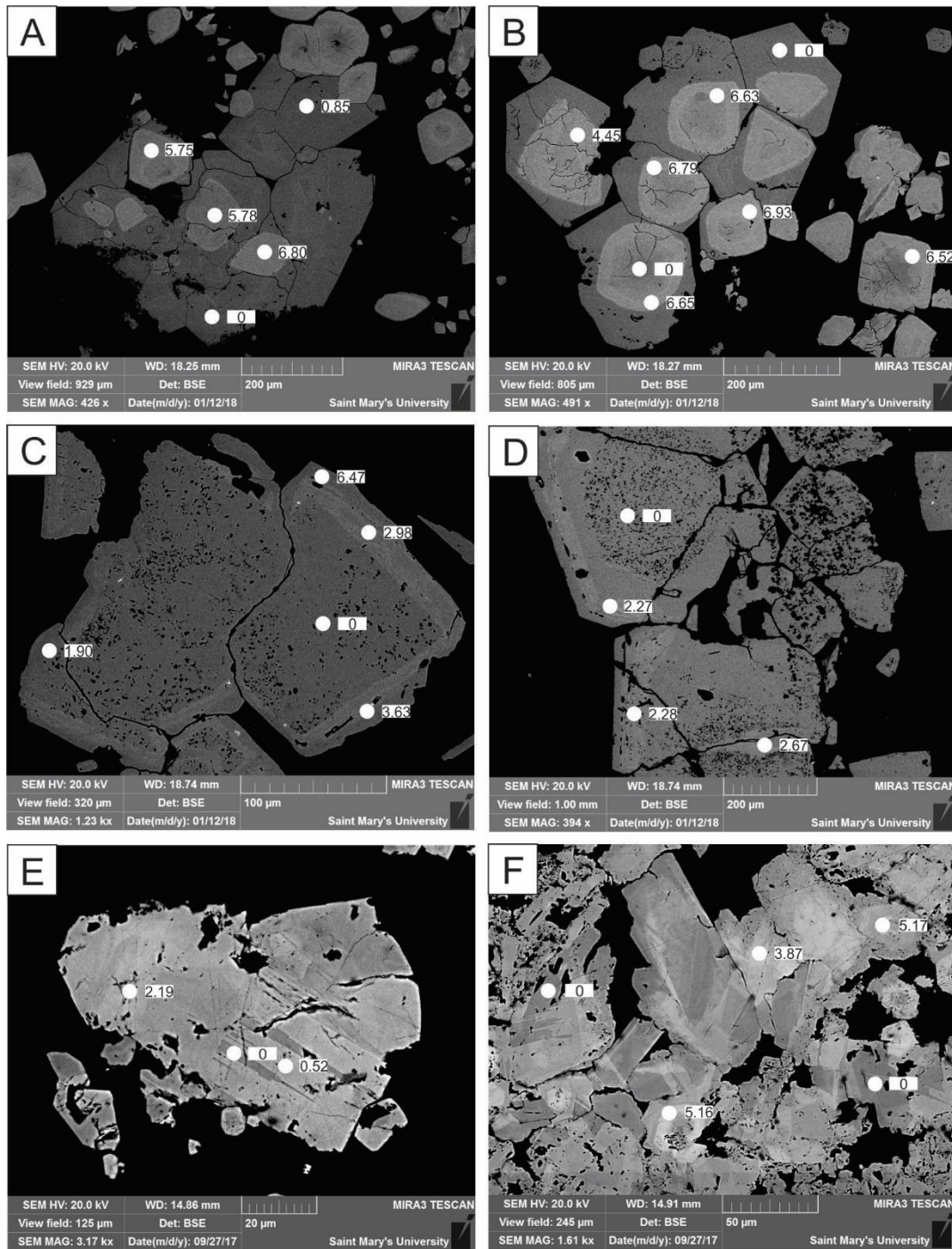
Figure 12 - SEM-BSE images of representative zoning types in pyrite from Warwick and Nuttby Mountain occurrences. Values in white rectangles represent wt% As. Spot size denoted by white circle is not proportional to SEM-EDS beam size. A-B) Core zoning, with arsenic concentrated in the core of the grain. C-D) Rim zoning, with arsenic concentrated around the edge of the grain. E-F) Boxwork zoning, with arsenic concentrated in cross-hatched patterns in pyrite grains.
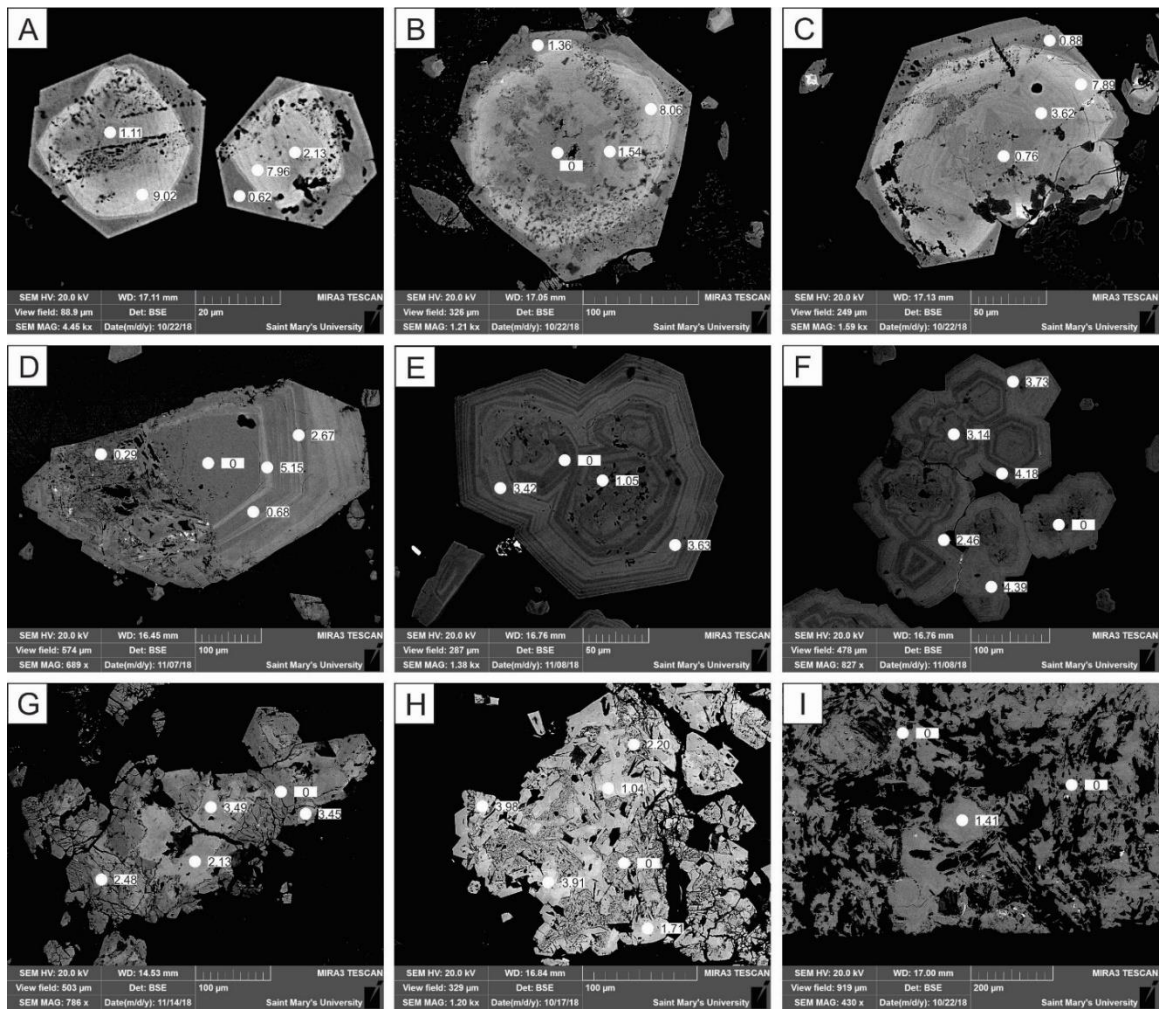
Figure 13 - SEM-BSE images of representative zoning types in pyrite from Core 1 and Core 2 samples. Values in white rectangles represent wt% As. Spot size denoted by white circle is not proportional to SEM-EDS beam size. A-C) Core zoning, with arsenic concentrated in the core of the grain. D-F) Rim zoning, with arsenic concentrated around the edge of the grain and in concentric rings trending towards the center of the grain. G-I) Massive zoning, with arsenic concentrated in non-uniform patches throughout sieved and fractured clusters of pyrite.

4.4.2 Bulk S isotopes

Bulk S isotope values and bulk S values were obtained for drill core samples (Table 4). Analyses of samples from Core 1 and Core 2 returned $\delta^{34}S_{VCDT}$ (‰) values ranging from -0.3 ‰ to 4.3 ‰ (ave. 2.0 ‰ ± 0.95 ‰), and bulk S (%) values ranging from 0.1 % to 47.3 % (ave. 5.6 % ± 9.77 %). Based on results from bulk S isotope and SEM analyses, nine samples with a range in As content and bulk S isotope values were selected for in-situ S isotope analysis.

4.4.3 In-situ S isotopes

In-situ S isotope analyses were conducted on Nuttby and Warwick Mountain occurrence samples and on a select 9 samples from Core 1 and Core 2 drill core samples. Pyrite from Nuttby Mountain occurrence showed distinct differences between As-rich and As-poor zones. Arsenic-poor pyrite cores has $\delta^{34}S$ values ranging from -1.8 ‰ to -0.6 ‰ (ave. -1.3 ± 0.4 ‰) and As-rich rims has $\delta^{34}S$ values between -3.0 ‰ and -6.8 ‰ (ave. -4.5 ± 1.5‰; Table 5, Figure 14A-C). Pyrite from Warwick Mountain showed indistinct differences between As-rich and As-poor zones. Arsenic-rich cores had $\delta^{34}S$ ranging from -1.5 ‰ to 0.7 ‰ (-0.2 ± 0.6 ‰) and As-poor rims with $\delta^{34}S$ between -1.9 ‰ and 0.6 ‰ (-1.1 ± 0.7 ‰; Table 6, Figure 14D-F). Pyrite from Core 1 and Core 2 samples shows less distinct variations in core and rim $\delta^{34}S$ values, with majority of the data ranging from -2.7 ‰ to 2.1 ‰ with a few outliers (Table 6, Figure 15). Marcasite, coeval with pyrite, in sample 16TM0096A shows a range of positive $\delta^{34}S_{VCDT}$ values ranging from 0.2 ‰ to 3.1 ‰ (Table 7).

Table 4 - Bulk sulfur isotope compositions of drill core samples from Core 1 and Core 2.

Sample	$\delta^{34}S_{VCDT}$ (‰)	S (wt%)
18KG001	3.0	9.8
18KG002	0.8	3.3
18KG004A	1.5	47.3
18KG004B	1.8	1.4
18KG005	2.6	6.4
18KG006	2.4	5.4
18KG008	1.6	0.5
18KG009	1.4	0.8
18KG010	1.4	0.6
18KG011	0.8	27.6
18KG012	-0.3	6.1
18KG013	1.9	0.9
18KG014	2.8	3.6
18KG015	2.6	1.3
18KG016	3.6	6.4
18KG017	2.1	3.4
18KG018	1.8	2.0
18KG019	1.8	2.5
18KG020	4.3	6.8
18KG021	3.2	3.8
18KG022	2.8	8.7
18KG023	1.3	0.3
18KG024	2.2	0.3
18KG025	1.7	0.2
18KG026	2.1	2.3
18KG027	0.6	0.1
18KG028	2.2	0.4

Table 5 - Summary table displaying collected results from SEM-EDS (As content (wt. %)) and SIMS ($\delta^{34}S_{VCDT}$ (‰)) analyses for each pyrite grain in selected surface samples from Nuttby and Warwick Mountain Au occurrences.

Sample	Image	Grain	Spot location	Grain Type	As content (wt. %)	SIMS $\delta^{34}S_{VCDT}$ (‰)
Nuttby	A	i	Core	Sieve (mod)	0.21	-0.6
		ii	Core	Sieve (mod)	0.07	-0.8
			Rim	Sieve (mod)	1.41	-4.4
		iii	Core	Sieve (mod)	0.45	-1.6
			Rim	Sieve (mod)	1.71	-3.1
		iv	Core	Sieve (mod)	0.30	-0.8
			Rim	Sieve (mod)	1.49	-4.4
			Rim	Sieve (mod)	0.13	-6.7
	B	i	Core	Sieve (mod)	0.31	-1.6
		ii	Core	Sieve (mod)	0.24	-0.9
			Rim	Clean	0.53	-4.4
			Rim	Clean	0.53	-6.8
	C	i	Core	Sieve (mod) / fractured (low)	0.15	-1.4
			Core	Sieve (mod) / fractured (low)	0	-1.8
		ii	Core	Sieve (mod)	0.16	-1.5
			Rim	Fractured (low)	0.08	-3.1
			Rim	Fractured (low)	0.23	-3.0
Warwick	D	i	Core	Fractured (mod)	4.17	0.5
			Core	Fractured (mod)	4.31	0.1
			Core	Fractured (mod)	4.87	-0.9
			Core	Fractured (mod)	5.03	0.4
			Rim	Fractured (mod)	0.16	-1.4
			Rim	Fractured (mod)	1.46	-1.8
			Rim	Fractured (mod)	1.18	-1.9
			Rim	Fractured (mod)	0.23	-1.1
			Rim	Fractured (mod)	0.16	-1.0
			Rim	Fractured (mod)	0.03	-1.0
			Rim	Fractured (mod)	0.28	-1.5
	E	i	Core	Clean	0.72	0.3
		ii	Core	Clean	5.26	-1.5
		iii	Core	Clean	3.89	0.2
		iv	Core	Clean	4.86	-0.6
		v	Core	Clean	4.44	-0.8
	F	i	Core	Clean	6.17	-0.6
		ii	Core	Clean	5.29	0.0
			Rim	Clean	0.84	-1.8
		iii	Core	Fractured (low)	3.96	0.7
			Rim	Fractured (low)	0	-0.4
		iv	Core	Clean	5.22	-0.3
			Rim	Clean	0.05	0.6

Notes:
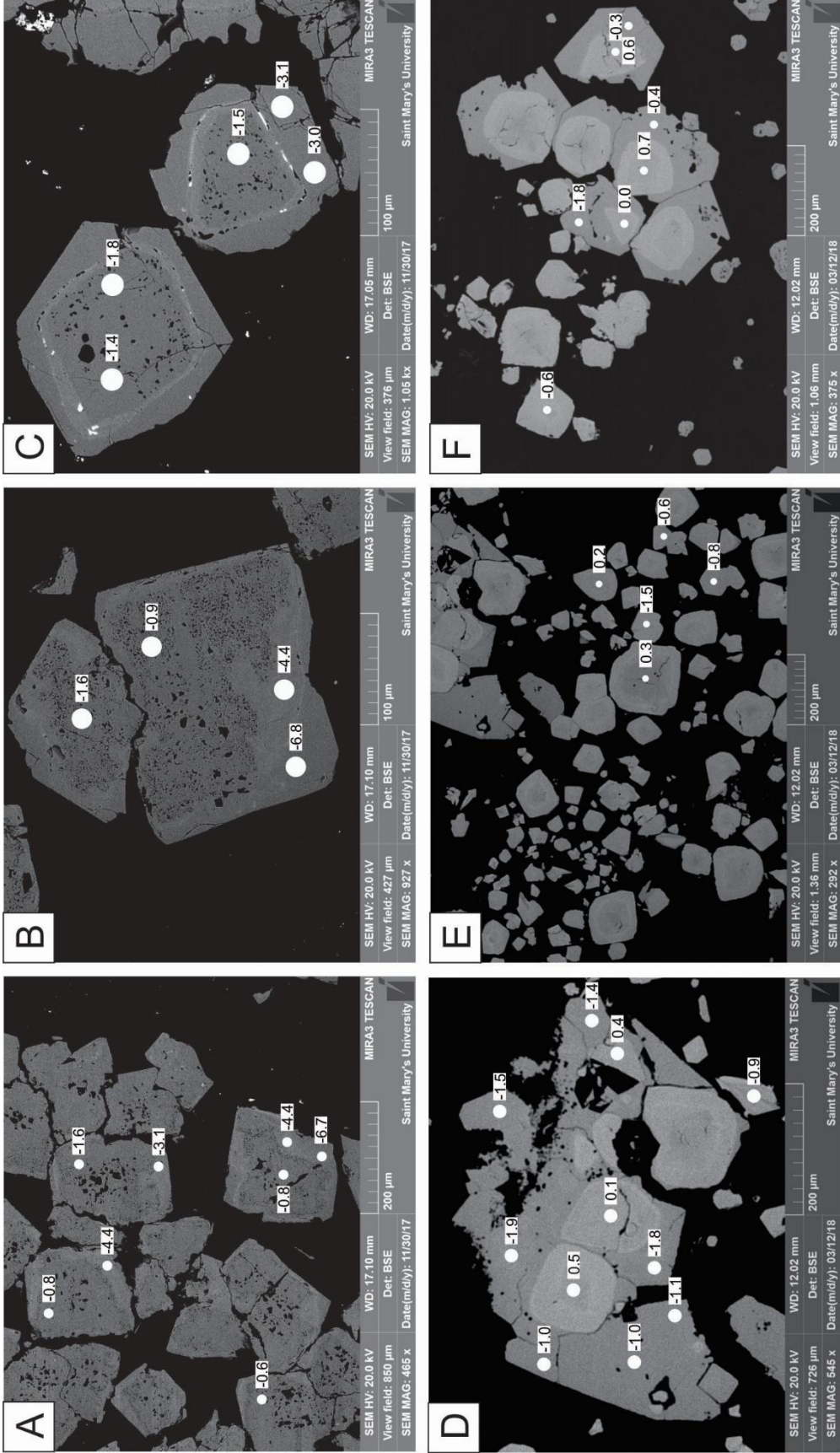Analyses listed in chronological order by individual grain. Corresponds to Figure 14.

Figure 14 - SEM-BSE images of representative pyrite grains from Nuttby (A-C) and Warwick Mountain (D-F) Au occurrences with secondary ion mass spectrometry (SIMS) point analysis results. Values in white rectangles represent S-isotope values in per mil. Spot size denoted by white circle is proportional to SIMS beam size.

Table 6 - Summary table displaying collected results from SEM-EDS (As content (wt. %)), SIMS ($\delta^{34}S_{VCDT}$ (‰)), and bulk S (Bulk $\delta^{34}S_{VCDT}$ (‰)) analyses for each pyrite grain in selected drill core samples from Core 1 and Core 2.

Sample	Image	Grain	Spot	Spot location	Grain type	As content (wt. %)	SIMS $\delta^{34}S_{VCDT}$ (‰)	Bulk $\delta^{34}S_{VCDT}$ (‰)
18KG002	A	i	1	Grain	Sieve (high)	0.54	-0.6	0.8
			2	Grain	Sieve (high)	0.46	-2.7	
			3	Grain	Sieve (high)	0	-0.9	
	B	ii	4	Grain	Sieve (high)	0.65	-1.7	
18KG006	C	i	8	Core	Clean	2.93	1.5	2.4
		ii	5	Core	Clean	6.32	0.2	
			6	Core	Clean	3.86	1.4	
			9	Core	Clean	5.20	1.1	
			7	Rim	Clean	3.19	1.6	
	D	iii	10	Core	Sieve (mod)	4.36	1.7	
	E	iv	11	Core	Sieve (low)	3.34	0.9	
	F	v	12	Core	Sieve (mod)	3.36	1.3	
			13	Rim	Sieve (mod)	2.06	2.1	
18KG009	G	i	14	Grain	Fractured (mod)	0.19	1.7	1.4
	H	ii	15	Grain	Fractured (mod)	0.12	-1.5	
18KG012	I	i	16	Grain	Fractured (mod)	0.28	-2.1	-0.3
			17	Grain	Fractured (mod)	0.08	-2.4	
			23	Grain	Fractured (mod)	0.14	-1.9	
			22	Grain	Fractured (mod)	0.02	-3.0	
	J	ii	18	Grain	Fractured (mod)	0.15	-3.7	
		iii	19	Grain	Fractured (mod)	0.03	-3.2	
	K	iv	20	Grain	Fractured (mod)	0.48	-2.3	
			21	Grain	Fractured (mod)	0.03	-2.5	
18KG014	L	i	25	Core	Sieve (low)	0.45	-0.7	2.8
			27	Core	Sieve (low)	0.70	-0.4	
			28	Core	Sieve (low)	1.31	-0.9	
			26	Rim	Sieve (low)	0.29	0.0	
			29	Rim	Sieve (low)	3.02	-0.9	
			43	Core	Sieve (low)	1.38	-0.8	
		ii	24	Core	Clean	0	0.1	
		iii	42	Core	Clean	2.46	-0.9	
			30	Rim	Clean	0	-1.3	
	M	i	31	Core	Sieve (mod)	0.14	-0.3	

Table 6 (con't) - Summary table displaying collected results from SEM-EDS (As content (wt. %)), SIMS (δ^{34}S$_{VCDT}$ (‰)), and bulk S (Bulk δ^{34}S$_{VCDT}$ (‰)) analyses for each pyrite grain in selected drill core samples from Core 1 and Core 2.

Sample	Image	Grain	Spot	Spot location	Grain type	As content (wt. %)	SIMS δ^{34}S$_{VCDT}$ (‰)	Bulk δ^{34}S$_{VCDT}$ (‰)
	N	i	32	Rim	Sieve (mod)	1.48	-0.7	
			33	Core	Sieve (mod)	0	-0.9	
			34	Rim	Sieve (mod)	1.79	-0.5	
	O	i	35	Core	Sieve (low)	0.12	5.6	
			37	Core	Sieve (low)	0.24	5.9	
			36	Rim	Sieve (low)	2.55	-1.0	
	P	i	40	Core	Sieve (mod)	0.09	6.1	
			38	Rim	Sieve (mod)	1.32	-1.0	
			39	Rim	Sieve (mod)	2.56	-0.3	
	Q	i	41	Core	Sieve (mod)	0.07	0.5	
18KG015	R	i	62	Core	Sieve (low) / fractured (mod)	0.53	-0.6	2.6
		ii	44	Core	Sieve (low) / fractured (high)	0.77	-1.7	
			64	Core	Sieve (low) / fractured (high)	1.16	-1.0	
			45	Rim	Sieve (low) / fractured (high)	0.93	-1.3	
		iii	63	Rim	Sieve (low)	2.11	-1.3	
		iv	46	Core	Clean	0.84	-1.9	
			47	Rim	Clean	2.49	-1.6	
	S	i	48	Core	Fractured (mod)	1.80	-1.2	
			49	Rim	Fractured (mod)	2.85	-0.3	
		ii	51	Core	Sieve (mod) / fractured (mod)	1.23	-0.2	
			50	Rim	Sieve (mod) / fractured (mod)	2.10	-0.9	
	T	i	53	Core	Sieve (mod)	0.79	1.2	
			54	Rim	Sieve (mod)	2.17	-0.2	
		ii	52	Core	Sieve (mod) / fractured (mod)	0.47	2.0	
			55	Rim	Sieve (mod) / fractured (mod)	2.45	0.0	
	U	i	58	Core	Sieve (mod)	0.73	1.8	
			59	Rim	Sieve (mod)	2.42	-0.2	
		ii	56	Core	Sieve (low)	0.75	0.7	
			57	Rim	Sieve (low)	2.69	-1.0	
	V	i	61	Core	Sieve (low) / fractured (low)	1.95	0.1	
			60	Rim	Sieve (low) / fractured (low)	2.06	0.0	
18KG016	W	i	75	Grain	Sieve (low)	2.30	0.6	3.6
			67	Grain	Sieve (low)	1.75	0.2	

Table 6 (con't) - Summary table displaying collected results from SEM-EDS (As content (wt. %)), SIMS ($\delta^{34}S_{VCDT}$ (‰)), and bulk S (Bulk $\delta^{34}S_{VCDT}$ (‰)) analyses for each pyrite grain in selected drill core samples from Core 1 and Core 2.

Sample	Image	Grain	Spot	Spot location	Grain type	As content (wt. %)	SIMS $\delta^{34}S_{VCDT}$ (‰)	Bulk $\delta^{34}S_{VCDT}$ (‰)
			66	Grain	Sieve (low)	3.79	0.1	
			65	Overgrowth	Sieve (low)	0.45	24.8	
			74	Overgrowth	Sieve (low)	0.30	26.4	
	X	i	69	Grain	Sieve (high) / fractured (high)	1.47	-0.3	
			70	Grain	Sieve (high) / fractured (high)	1.57	-0.8	
		ii	68	Grain	Sieve (high) / fractured (high)	3.09	-1.7	
	Y	i	71	Grain	Sieve (high) / fractured (high)	0.32	-2.2	
		ii	73	Grain	Sieve (high) / fractured (high)	2.41	-1.1	
			72	Grain	Sieve (high) / fractured (high)	4.22	-1.8	
18KG018	Z	i	80	Marcasite	Fractured (high)	1.56	-1.5	1.8
		ii	79	Marcasite	Fractured (high)	0.27	-3.8	
			81	Marcasite	Fractured (high)	1.08	-4.0	
		iii	82	Marcasite	Fractured (high)	1.72	-3.6	
		iv	83	Marcasite	Fractured (high)	0.84	-3.5	
	AA	i	84	Marcasite	Fractured (high)	0.41	0.0	
			85	Marcasite	Fractured (high)	1.66	-1.5	
	AB	i	86	Marcasite	Fractured (high)	2.92	-3.6	
	AC	i	87	Marcasite	Clean	2.74	-0.9	
18KG020	AD	i	90	Core	Clean	0.70	-1.8	4.3
			89	Rim	Clean	3.51	-0.2	
			88	Rim	Clean	1.11	0.2	
	AE	i	98	Core	Clean	0.73	-1.5	
			91	Core	Clean	1.39	1.2	
			92	Rim	Clean	2.69	-0.6	
	AF	i	95	Grain	Sieve (high)	0.31	-3.8	
			96	Grain	Sieve (high)	0.82	-3.3	
			93	Grain	Sieve (high)	0.39	-1.3	
		ii	94	Grain	Sieve (high)	1.03	-1.2	
	AG	i	97	Grain	Sieve (high)	1.21	-1.5	

Notes:
Analyses listed in chronological order by individual grain. Corresponds to Appendix.

Table 7 - Summary table displaying relative As content and results from SIMS ($\delta^{34}S_{VCDT}$ (‰)) for each marcasite grain in surface sample 16TM0096A.

Sample	Grain	Spot Location	Grain type	Relative As content	SIMS $\delta^{34}S_{VCDT}$ (‰)
16TM0096A	i	Rim	Marcasite	High	1.5
		Core	Marcasite	Low	0.8
		Core	Marcasite	Low	0.7
		Rim	Marcasite	High	1.6
		Core	Marcasite	Low	1.4
		Rim	Marcasite	Low	2.5
	ii	Core	Marcasite	Low	1.5
		Core	Marcasite	Low	0.2
		Rim	Marcasite	High	1.0
		Rim	Marcasite	High	2.8
		Core	Marcasite	Low	2.4
	iii	Core	Marcasite	Low	2.2
		Rim	Marcasite	High	3.1

Figure 15 - SEM-BSE images of representative pyrite grains from Core 1 and Core 2 samples with secondary ion mass spectrometry (SIMS) point analysis results. Values in white rectangles represent S-isotope values in per mil. Spot size denoted by white circle is proportional to SIMS beam size. A) 18KG002. B) 18KG006. C) 18KG012. D) 18KG014. E-F) 18KG015. G) 18KG016. H) 18KG018. I) 18KG020.

4.4.4 Other trace element distributions

Ten spot analyses were conducted by electron microprobe (EMP) on selected pyrite grains from Nuttby and Warwick Mountain (Table 8; Figure 16). Gold and Cu concentrations for both Nuttby and Warwick Mountain were below the detection limits; with the lowest Au and Cu detection limits being 410 and 677 ppm, respectively. Arsenic-rich rims from Nuttby Mountain returned As values of 2.47 wt. % and 3.21 wt. %; otherwise, As was below detection. Arsenic-rich areas near the core of pyrite from Warwick Mountain returned As values ranging from 3.05 – 5.07 wt. %. Rims of pyrite from Warwick had As values ≤ 0.07 wt. %.

Element maps for Au, Fe, S, Cu, and As were also collected. Sulphur and As maps demonstrate an inverse relationship between the two, suggesting the replacement of S by As in the structure of pyrite (e.g., Fleet and Mumin, 1997). Pyrite from Nuttby Mountains is oscillatory zoned with respect to As with the highest concentrations of As occurring on the rims of pyrite (Figure 17 and Figure 18). Oscillatory zoning is also present in the Warwick Mountain pyrites, with As values increasing progressively outwards from the core, then gradually decreasing to As-free rims (Figure 19 and Figure 20). Gold maps show some elevated concentrations near and along the rims of pyrite from Nuttby, but no gold grains were observed during SEM-EDS analyses so it could be Au present within the structure of pyrite. No Au was observed in the maps from Warwick Mountain. Copper is below detection limits in pyrite from both Nuttby and Warwick Mountain.

Table 8 - Electron microprobe analysis of pyrite from Nuttby Mountain and Warwick Mountain Au occurences. All analyses reported in wt. %.

Point	Analysis	Fe	Cu	As	S	Au	Total
1	Nuttby-2 core	46.36	B.D.L.	B.D.L.	53.39	B.D.L.	99.76
2	Nuttby-2 rim	45.80	B.D.L.	2.47	52.04	B.D.L.	100.37
3	Nuttby-3-1 core	46.78	B.D.L.	B.D.L.	53.88	B.D.L.	100.67
4	Nuttby-3-1 core2	46.53	B.D.L.	B.D.L.	53.92	B.D.L.	100.51
5	Nuttby-3-1 rim	45.41	B.D.L.	3.21	50.83	B.D.L.	99.50
6	Warwick-1 core	44.97	B.D.L.	5.07	50.68	B.D.L.	100.76
7	Warwick-1 rim	45.90	B.D.L.	0.07	53.28	B.D.L.	99.26
8	Warwick-6 core	45.78	B.D.L.	3.05	51.70	B.D.L.	100.58
9	Warwick-6 rim1	44.99	B.D.L.	5.05	50.58	B.D.L.	100.63
10	Warwick-6 rim2	46.64	B.D.L.	B.D.L.	54.01	B.D.L.	100.73

Notes:

B.D.L. = Below Detection Limit
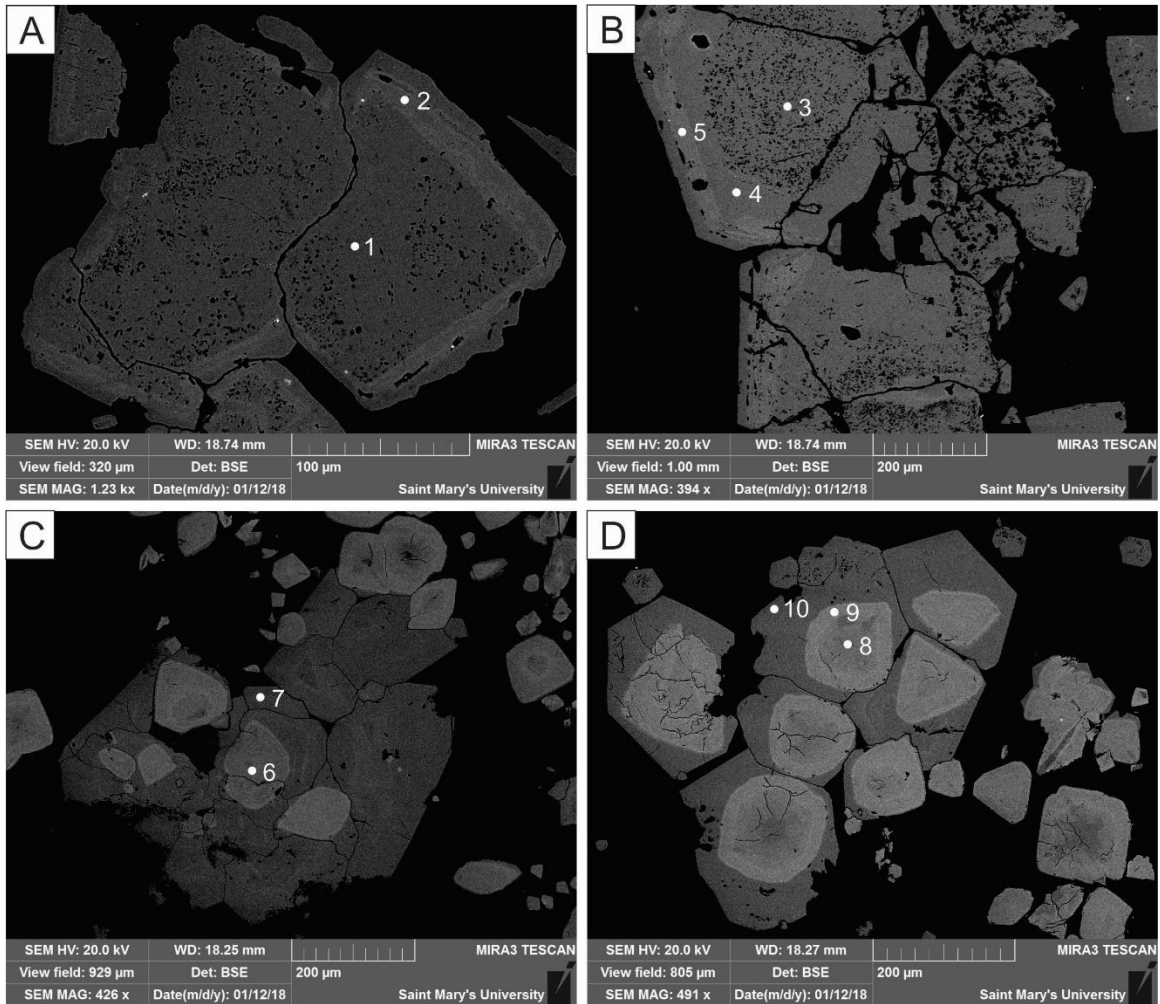
Figure 16 - Pyrite from Nuttby Mountain (A-B) and Warwick Mountain Au occurrences (C-D) analyzed by electron microprobe. Spot analyses correspond to the analysis number in Table 8.
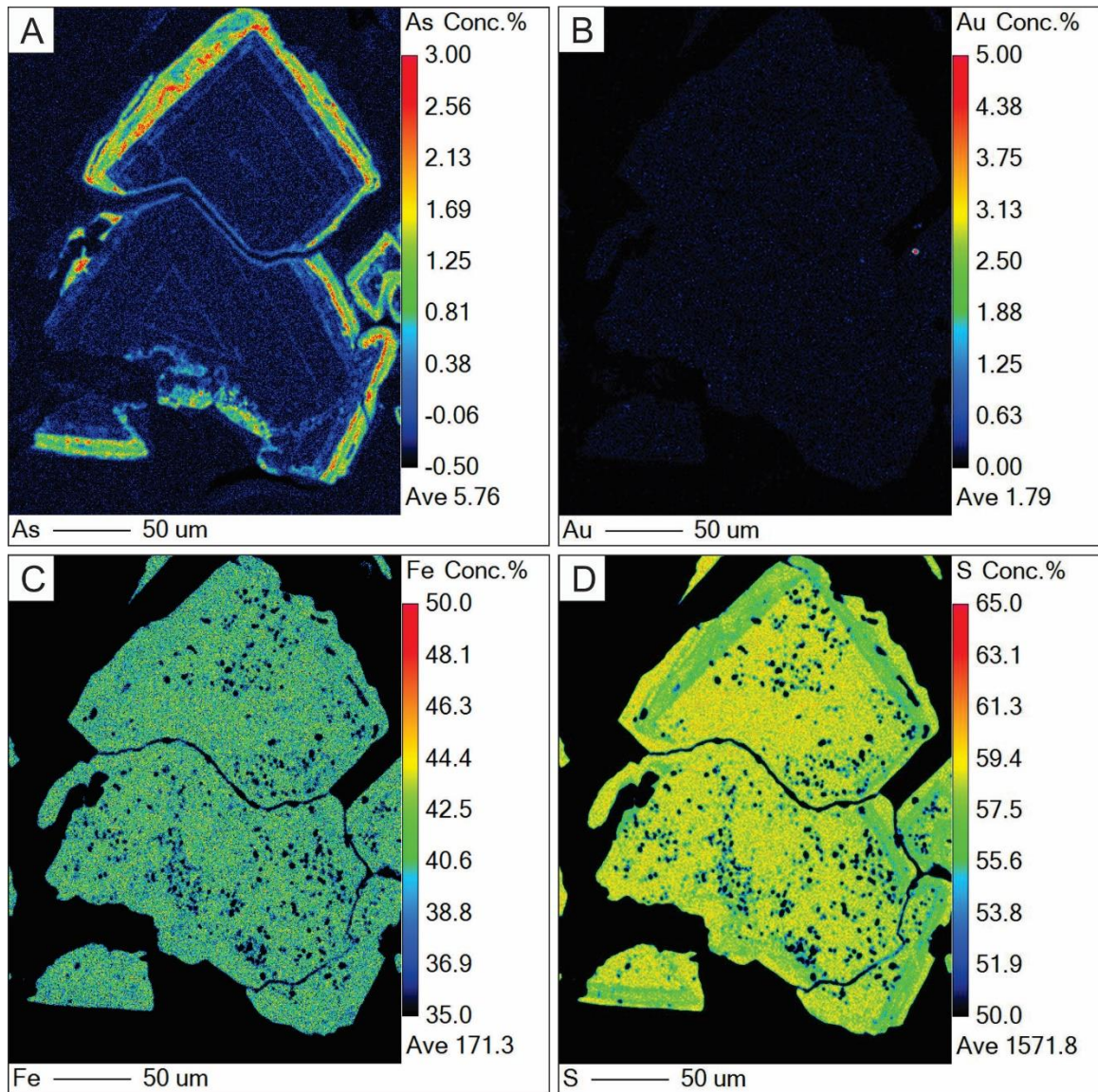
Figure 17 - Element map of As, Au, Fe, and S returned from electron microprobe analysis of pyrite from Nuttby Mountain Au occurrence. Mapped pyrite corresponds to Figure 16A.
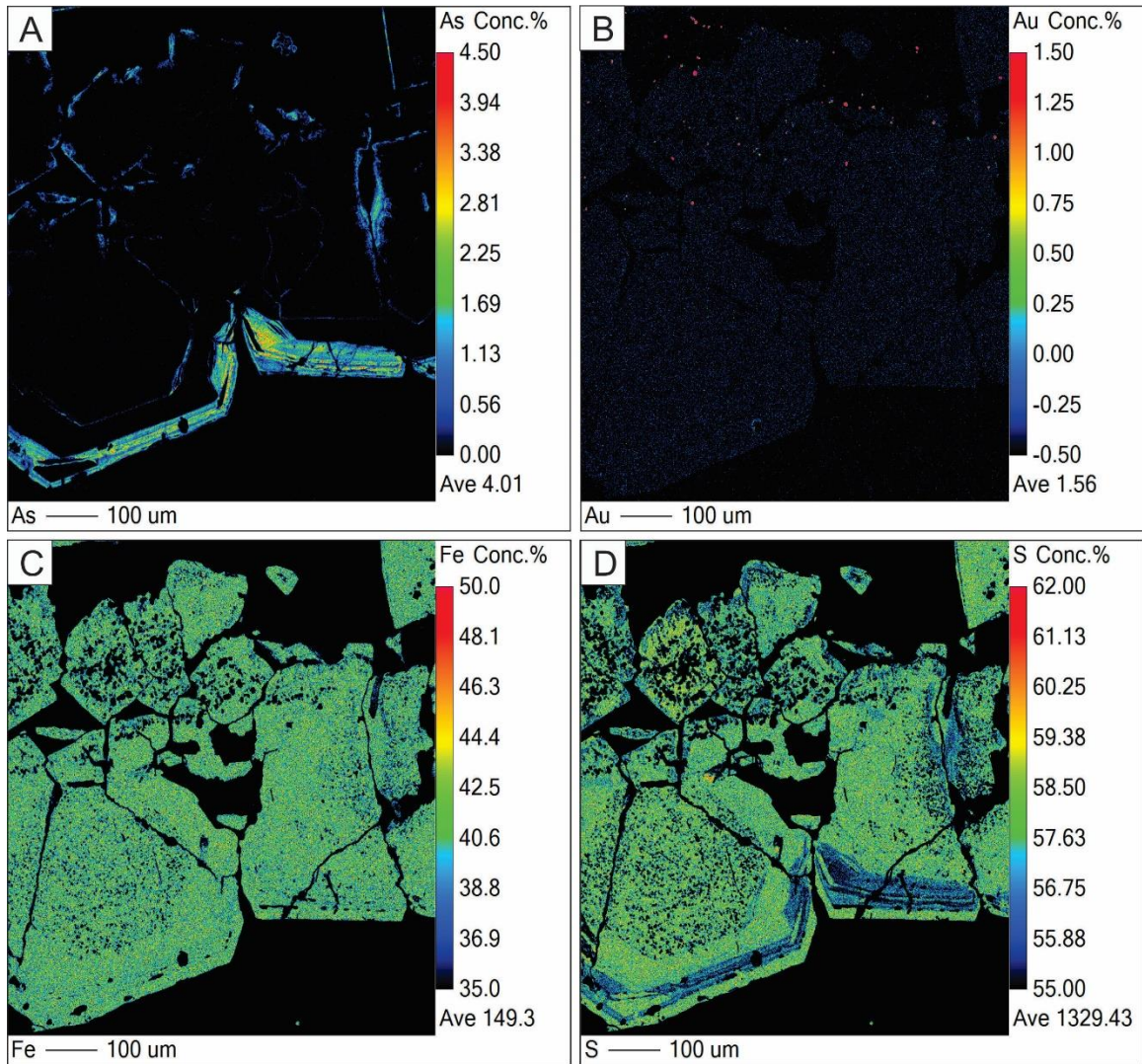
Figure 18 - Element map of As, Au, Fe, and S returned from electron microprobe analysis of pyrite from Nuttby Mountain Au occurrence. Mapped pyrite corresponds to Figure 16B.
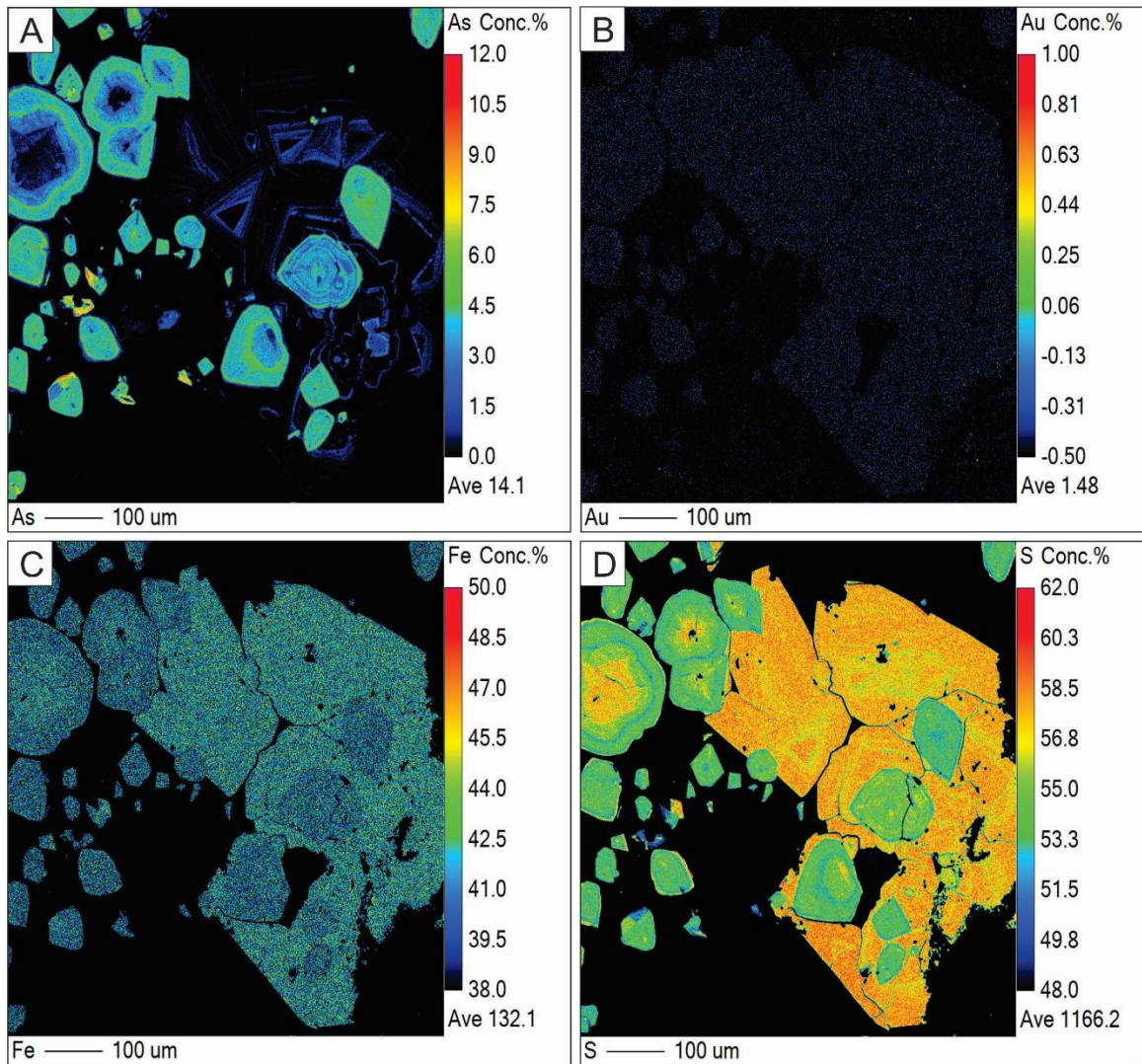
Figure 19 - Element map of As, Au, Fe, and S returned from electron microprobe analysis of pyrite from Warwick Mountain Au occurrence. Mapped pyrite corresponds to Figure 16C.
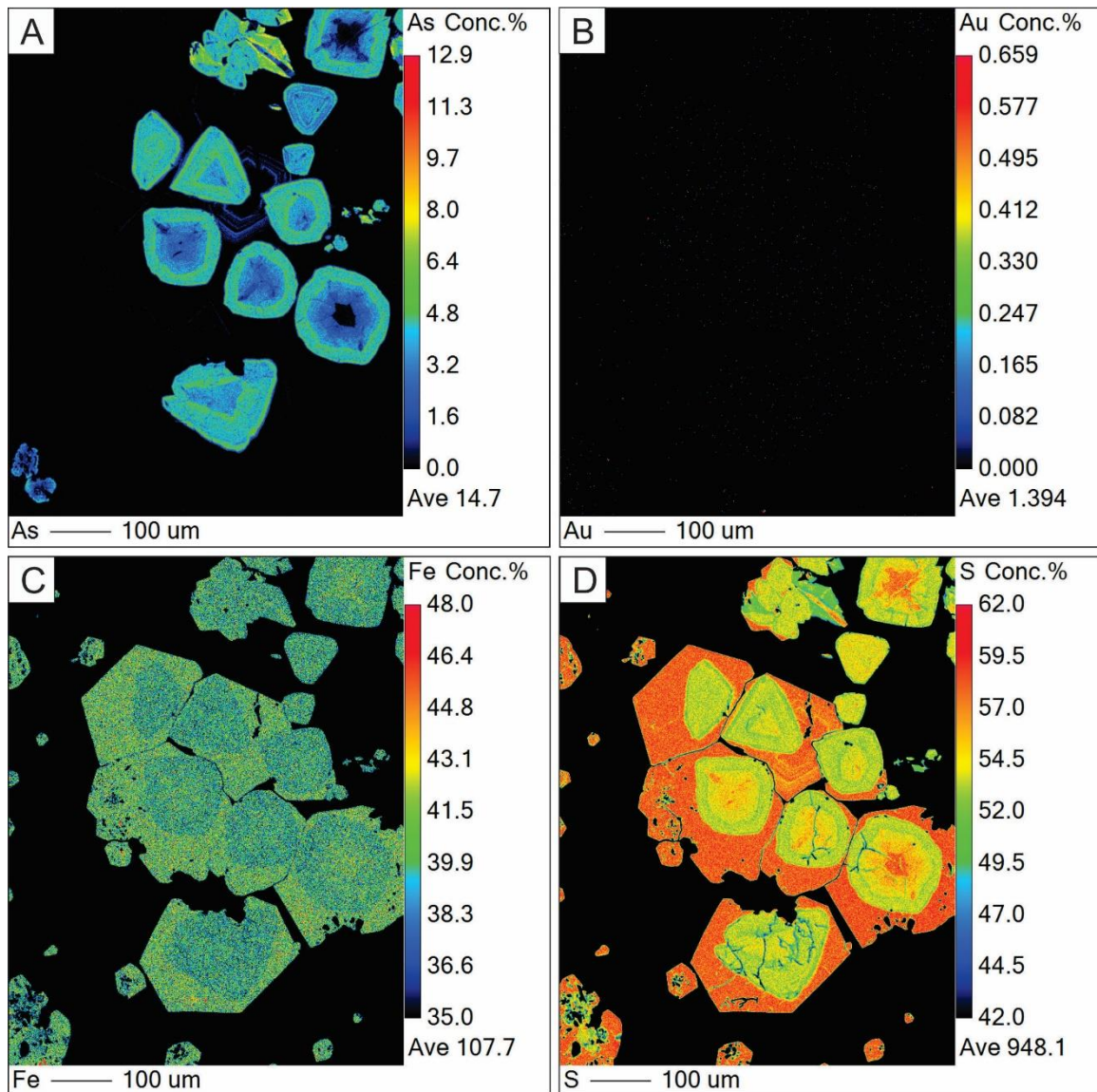
Figure 20 - Element map of As, Au, Fe, and S returned from electron microprobe analysis of pyrite from Warwick Mountain Au occurrence. Mapped pyrite corresponds to Figure 16D.

Pyrite was selected for LA-ICP-MS trace element mapping from Warwick and Nuttby Mountain occurrence samples, and Core 1 and Core 2 samples based on the strong As zoning confirmed by SEM-EDS and EMP.

Warwick Mountain pyrite shows complex zoning of trace elements throughout the pyrite growth history (Figure 21 and Figure 22). Elements concentrated in the core at the onset of pyrite formation include Hg-Se-Co-Ni-Cd-Cu-Pb, followed by As-Sb-In-Ag-Au with minor Hg-Se forming a zone around the core (Figure 21). Minor concentrations of Co-Ni±Mo±Sn form a thick rim after the As enrichment stage, followed by a final stage of pyrite growth characterized by W-Sn-Co-Ni-In-Sb-Cu-Ag±Pb. Concentrations of Au in pyrite do not reach higher than ~ 0.1 ppm.

Nuttby Mountain pyrite has a much more simple trace element distribution (Figure 23 and Figure 24). Trace elements that are initially concentrated in pyrite are Cu, Pb, and Sn that have consistent concentrations until a thin rim of Sb±As occurs present along with Mo-Cu-Pb-Sn enrichment (Figure 23). Molybdenum is also associated with initial pyrite formation, but shows oscillatory zoning instead of consistent concentrations, and no other elements correlate with this oscillatory zoning of Mo (Figure 23). Following the thin rim of Sb±As, a zone with increased concentrations of As-Sb-Cu-Pb along with Au-Ag-Hg-Se-Co-Ni-In-W occurs (Figure 23). The final stage of pyrite growth shows minor amounts of Se-Pb-Cu on the very edge of the pyrite grains (Figure 23). Concentrations of Au in pyrite reach up to ~ 10 ppm.

Sample 18KG014 (Core 1) pyrite shows a non-uniform (contrasting) distribution of elements in adjacent grains in the selected area (Figure 25 and Figure 26), and

the relationship between their relative growth history is unknown. Grain 1 and Grain 2 labels are denoted in the SEM-BSE photomicrograph in Figure 25. Grain 1 shows little trace element enrichment in the core, with only minor amounts of Co-Cu-In-Mo-Sb. The rim is enriched in As-Co-Mn-Ni-Se-Zn (Figure 25). The core of Grain 2 is enriched in Ag-Cd-Co-Cu-Hg-Ni-Sb-Zn±Mn-Pb-W (Figure 25). The concentrations of the listed elements decrease throughout the pyrite growth history. The rim of Grain 2 is enriched in As-Co-Se±Mn-Ni-Zn. Both grains show simple to oscillatory zoning of As and Sb throughout their growth history (Figure 25). Concentrations of Au in both Grain 1 and Grain 2 reach values similar to that at Nuttby Mountain occurrence (up to 10 ppm) and do not correlate to Ag. Areas of Au enrichment coincide to pitted areas (sieve texture) and As-Co enriched rims, suggesting late gold enrichment (like at the Nuttby Mountain occurrence).
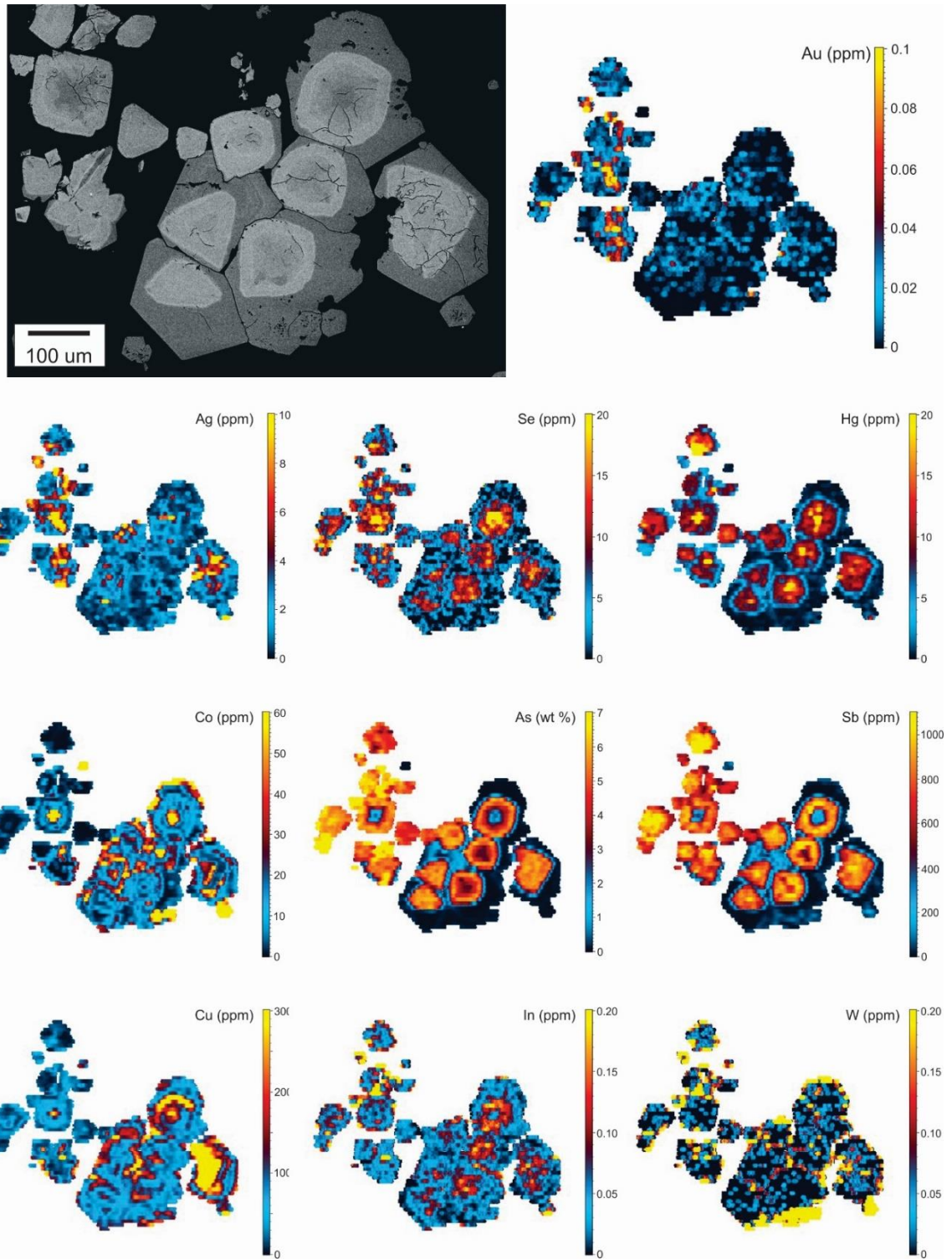
Figure 21 - Element maps of Au, Ag, Se, Hg, Co, As, Sb, Cu, In, and W returned from LA-ICP-MS analysis of pyrite from Warwick Mountain Au occurrence. Values in parts per million, except As in wt. %.
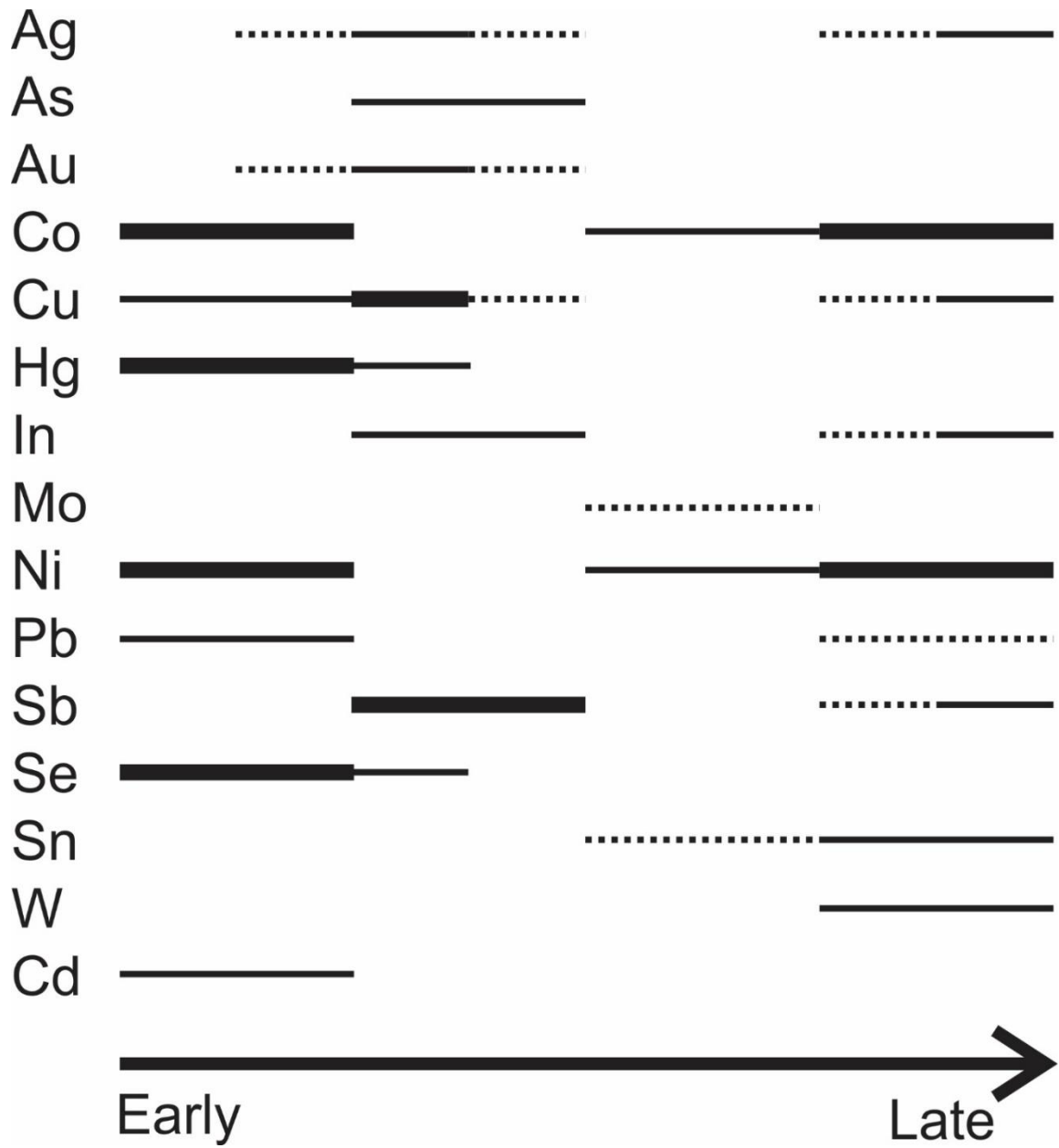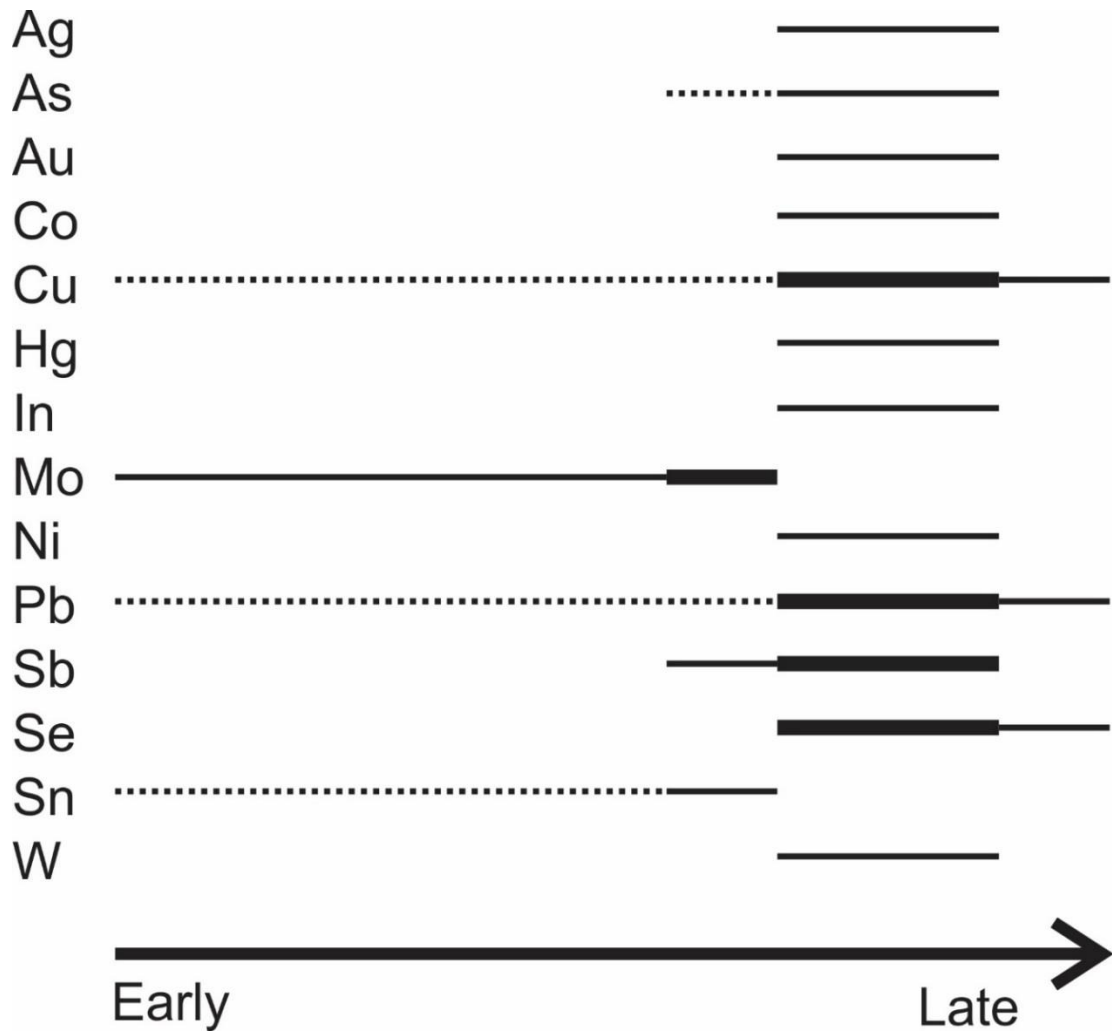
Figure 22 - Pyrite elemental paragenesis for LA-ICP-MS map of pyrite from Warwick Mountain Au occurrence. Thickness of bars for individual elements corresponds to relative concentrations.
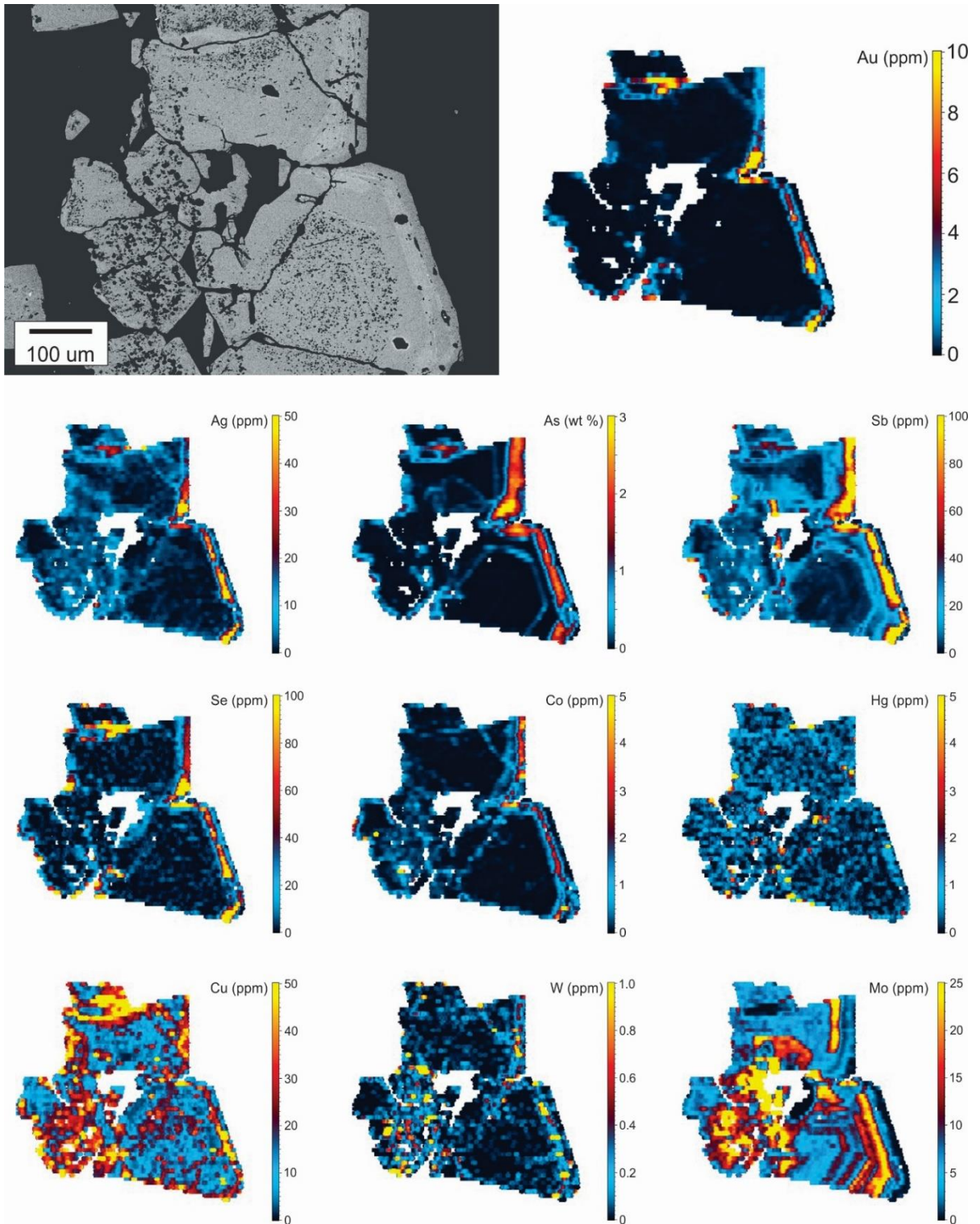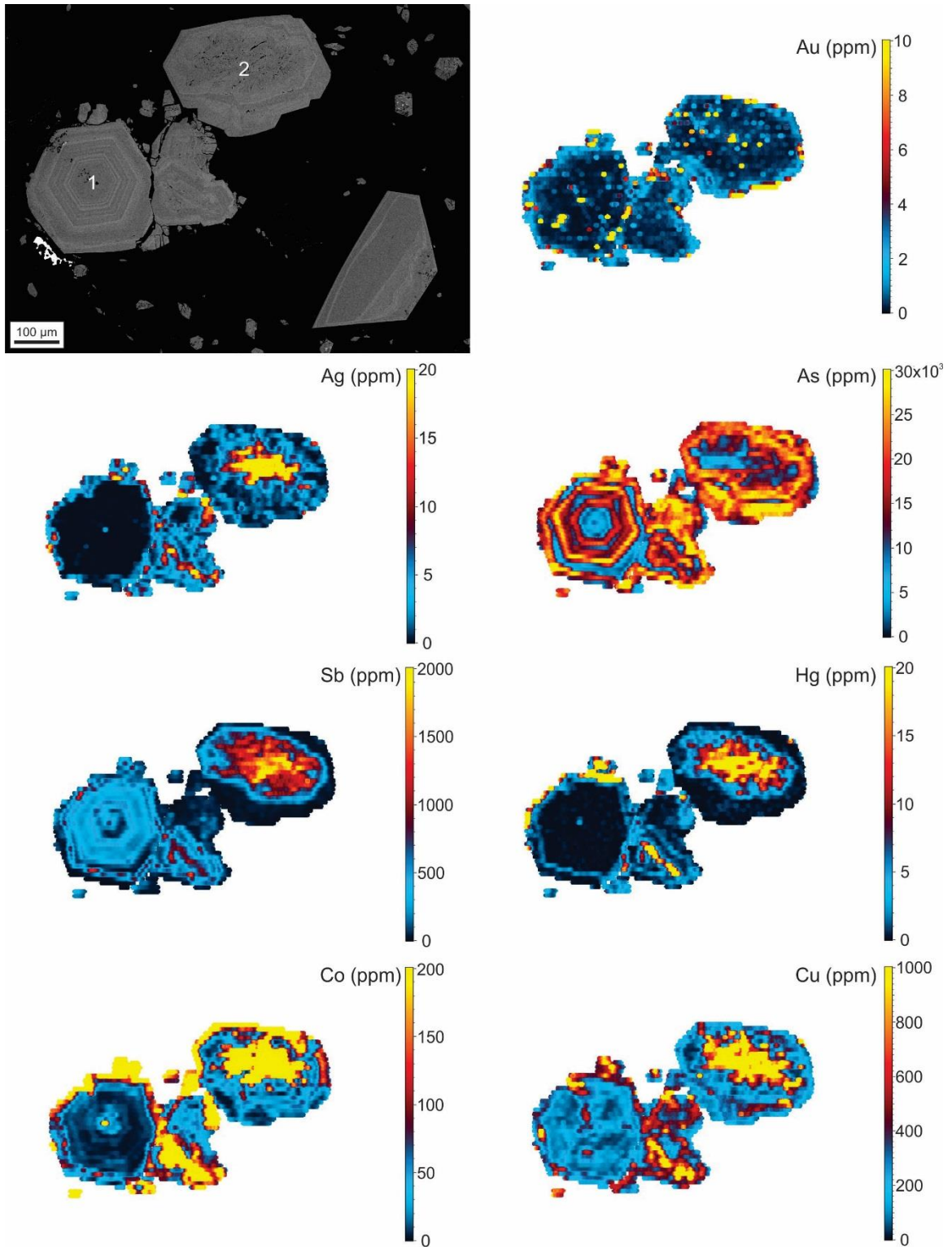
Figure 23 - Element maps of Au, Ag, As, Sb, Se, Co, Hg, Cu, W, and Mo returned from LA-ICP-MS analysis of pyrite from Nuttby Mountain Au occurrence. Values in parts per million, except As in wt. %.

Figure 24 - Pyrite elemental paragenesis for LA-ICP-MS map of pyrite from Nuttby Mountain Au occurrence. Thickness of bars for individual elements corresponds to relative concentrations.

Figure 25 - Element maps of Au, Ag, As, Sb, Hg, Co, and Cu returned from LA-ICP-MS analysis of pyrite from sample 18KG014 (Core 1). Values in parts per million.
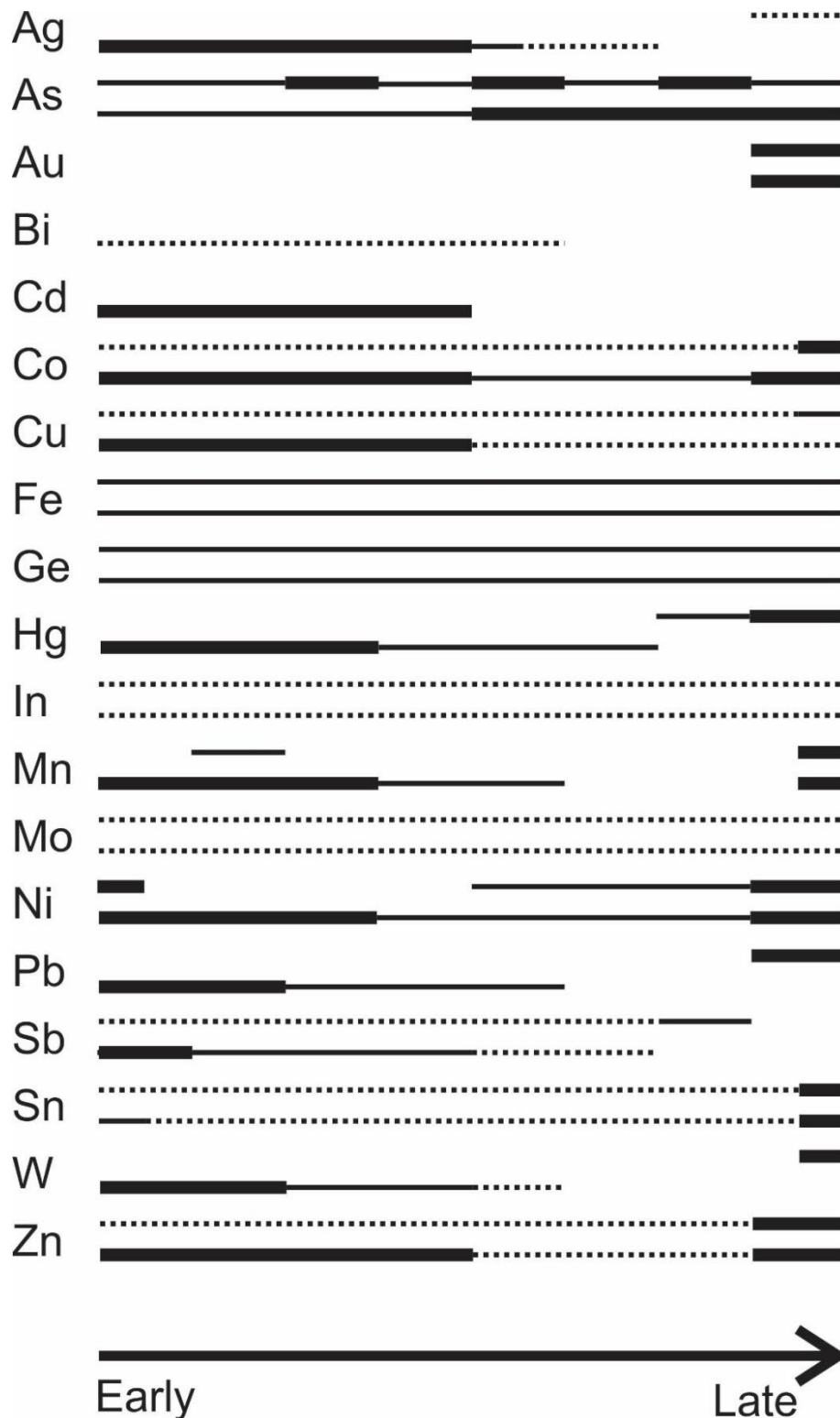
Figure 26 - Pyrite elemental paragenesis for LA-ICP-MS map of pyrite from sample 18KG014 (Core 1). Thickness of bars for individual elements corresponds to relative concentrations. For each element, top paragenesis bar corresponds to Grain 1 and lower paragenesis bar corresponds to Grain 2.

5.0 Discussion

5.1 Style of epithermal mineralization

The host assemblages (bimodal rhyolite-basalt), gangue textures (comb and colloform banding), and sulphide mineral assemblage (pyrite-marcasite-galena, sphalerite, arsenopyrite, chalcopyrite) are consistent with low sulphidation epithermal deposits, and share characteristics with shallow (<300 m) and deep (>300 m) variants of this classification (Hedenquist et al., 2000). Although no cinnabar and/or stibnite were observed, common shallow low sulphidation minerals, assays showed anomalously high concentrations of Hg and Sb which are components of cinnabar and stibnite, respectively (Hedenquist et al., 2000).

5.2 S isotope systematics

5.2.1 Relationship between bulk $\delta^{34}S_{VCDT}$ and bulk S

Bulk S and bulk $\delta^{34}S_{VCDT}$ are positively correlated with the exception of a few samples (Figure 27). This demonstrates that the more pyrite present, the higher the bulk $\delta^{34}S_{VCDT}$. This is not likely to be a function of grain size or relative growth zone size. For that to be the case, samples showing higher bulk S and bulk $\delta^{34}S_{VCDT}$ would have grains with volumetrically larger growth zones with higher $\delta^{34}S_{VCDT}$ values. Comparing results from in-situ SIMS analysis with BSE images, it can be seen that this is not the case. A more likely explanation is that samples containing more sulphide also contain more sulphate formed via weathering processes. Sulphates, enriched in ^{34}S and varying in abundance relative to

sulphide, would give higher bulk $\delta^{34}S_{VCDT}$ values in more weathered/corroded samples.

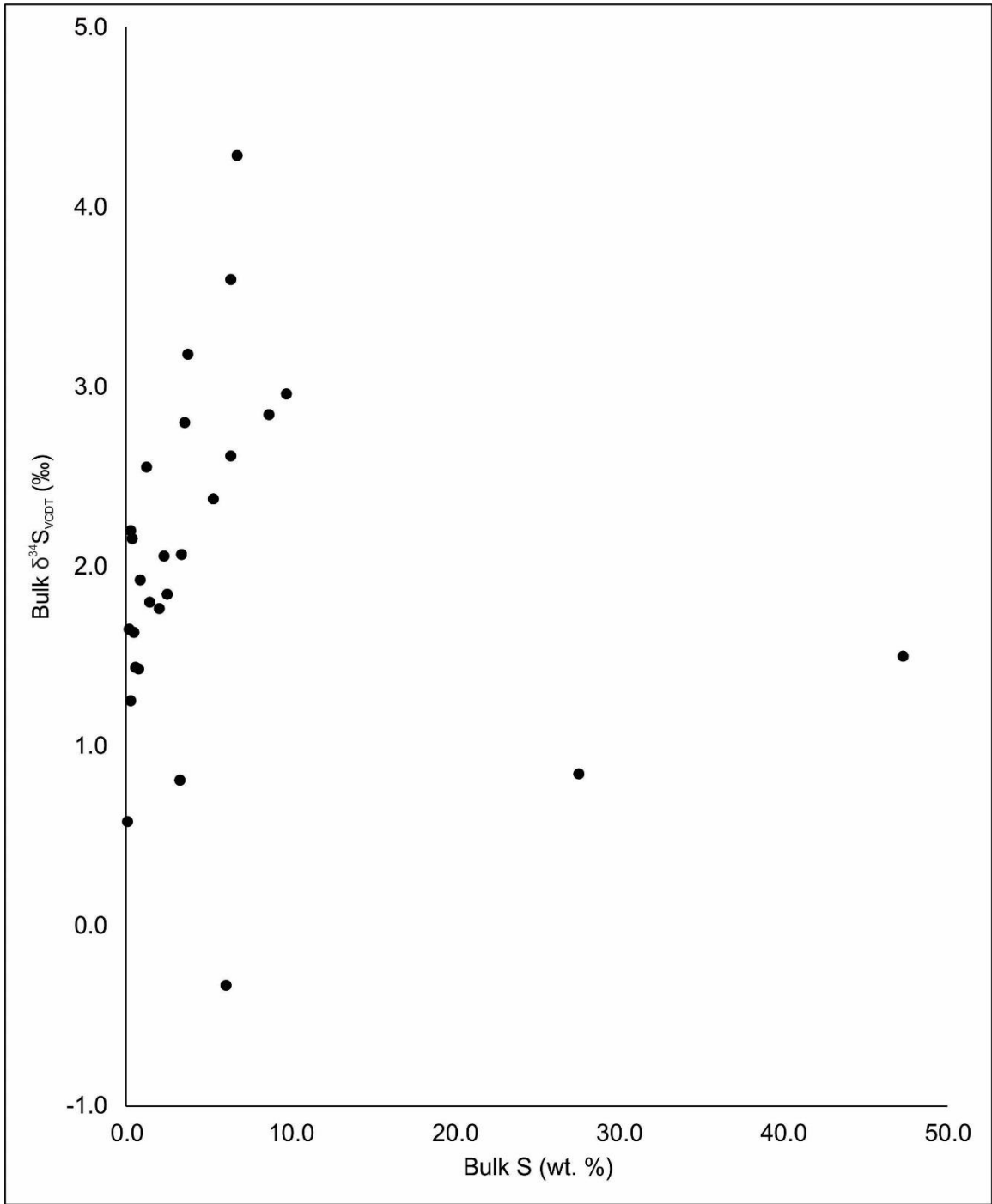Figure 27 - Graph depicting relationship between in-situ δ34SVCDT and bulk S.

5.2.2 Relationship between in-situ $\delta^{34}S_{VCDT}$ and As content

In-situ $\delta^{34}S_{VCDT}$ and As content are positively correlated (Figure 28), but the significance of this correlation must be tested. In total, 135 analyses of in-situ $\delta^{34}S_{VCDT}$ by SIMS were conducted on pyrite grains from Warwick and Nuttby Mountain occurrences, and Core 1 and Core 2 samples. Seven analyses were not included in further calculations as they were considered to be outliers skewing the dataset. The one-sided significance test was used, as the sign of the correlation was relevant to its interpretation. The calculated value of r is 0.343 (Pearson correlation coefficient for normally distributed data). To determine the statistical significance of calculated value of r as an estimate of ρ, the minimum value of r above which we reject the null hypothesis that $\rho = 0$ at a given level of significance for a calculated number of degrees of freedom (DF = number of samples – 2) is referred to. Using standard significance reference tables when using the one-sided test at a DF = 126, the minimum value of r required to reject the null hypothesis at a 99.9% confidence limit (0.1% level) is 0.289. Since our calculated value for r from the actual data set is > 0.289, there is a 99.9% chance that the correlation observed in the sample set also applies to the entire population and that the correlation will be a positive one. This indicates that processes that influence As going in to the structure of pyrite also influence ^{34}S enrichment in pyrite.
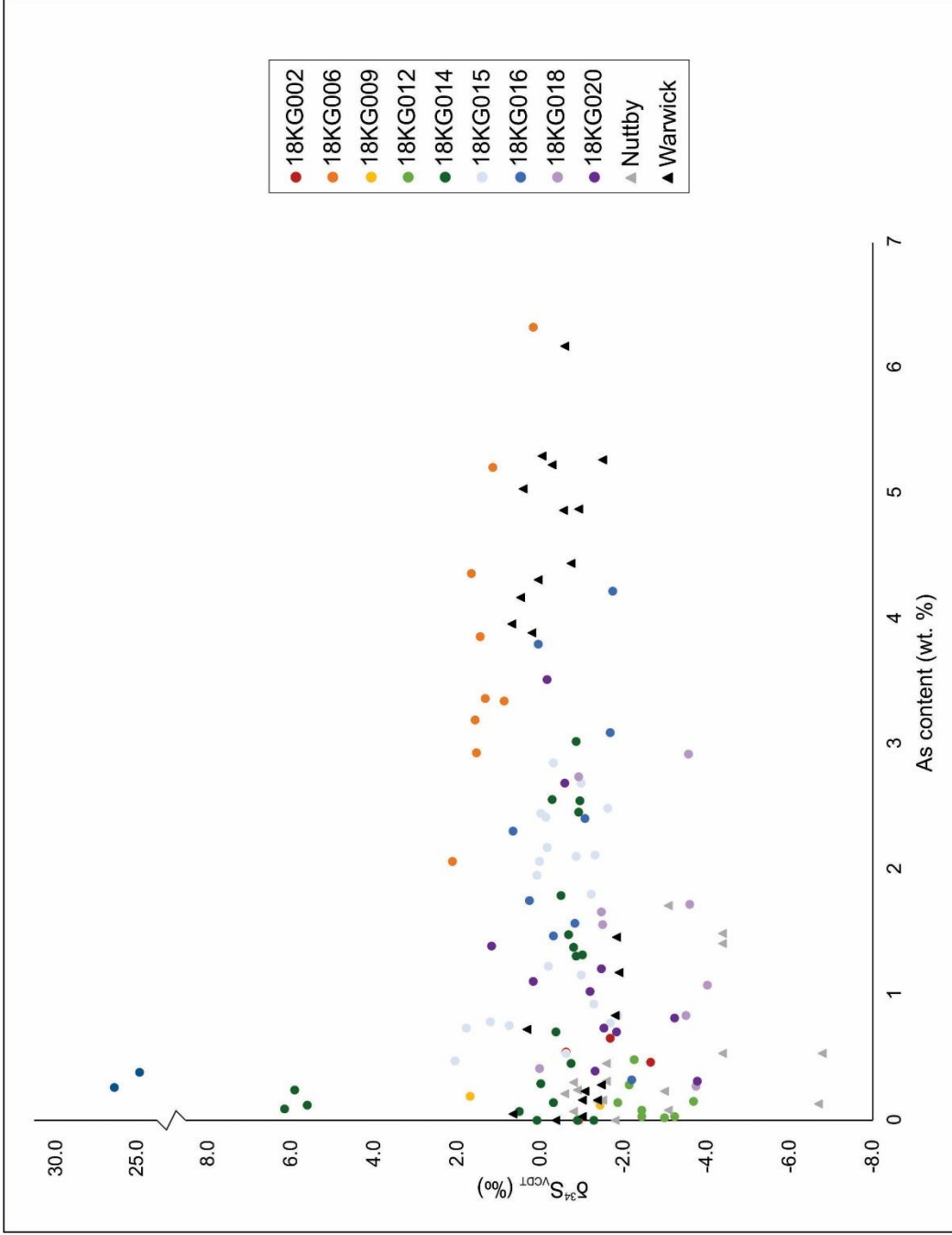
Figure 28 - Graph depicting relationship between in-situ $\delta^{34}S_{VCDT}$ and As content. Analyses grouped by sample.

5.2.3 Relationship between bulk $\delta^{34}S_{VCDT}$ and in-situ $\delta^{34}S_{VCDT}$

A comparison between bulk $\delta^{34}S_{VCDT}$ values and in-situ $\delta^{34}S_{VCDT}$ values from Core 1 and Core 2 samples reveals a broad positive correlation. However, the bulk $\delta^{34}S_{VCDT}$ values are higher than the in-situ $\delta^{34}S_{VCDT}$ values for pyrite by about ~ 2 ‰ (Figure 29). This suggests that the bulk $\delta^{34}S_{VCDT}$ values are a result of ^{32}S enriched sulphide mixed with a ^{34}S enriched component that was not observed petrographically. There are several possible explanations for this. Under typical open or closed system conditions, the formation of sulphates from sulphides causes ^{34}S to fractionate into sulphates and ^{32}S to fractionate in to the sulphides (Sharp, 2007). In a study by Little et al. (1994), sulphate-reducing bacteria were shown to be responsible for microbiologically influenced corrosion, causing pitting, crevice corrosion, dealloying, and under deposit corrosion. Their data shows that ^{32}S accumulates in the corrosion products, while ^{34}S accumulates in bacteria due to biologically-mediated fractionation. During both of these processes, the fractionation only changes the distribution of the ^{32}S and ^{34}S and not the bulk value of $\delta^{34}S_{VCDT}$, meaning that the bulk $\delta^{34}S_{VCDT}$ values vs. in-situ $\delta^{34}S_{VCDT}$ values should still plot on the dashed line (Figure 29). In this study, neither of these processes provide an appropriate explanation since the bulk $\delta^{34}S_{VCDT}$ values are generally higher that the in-situ $\delta^{34}S_{VCDT}$ values. It is more likely that there was an undetected coexisting phase enriched in ^{34}S (i.e. a sulphate rich weathering/corrosion phase), and that during corrosion, ^{32}S was physically removed from the system through degassing of some S-bearing phase (H_2S, SO_2,

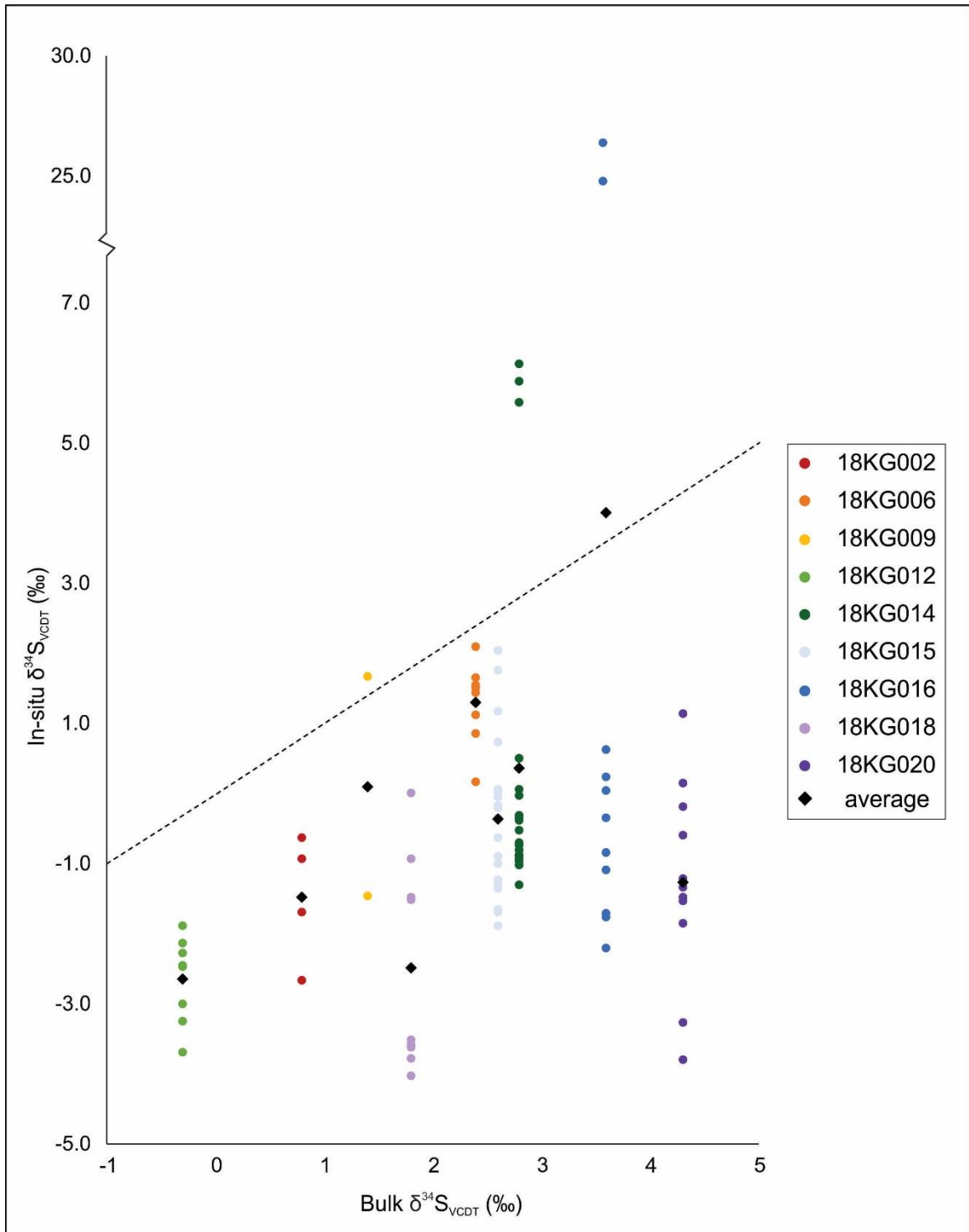COS) or leaching of ^{32}S out of the core samples by precipitation while stored outside.

Figure 29 - Graph depicting relationship between in-situ δ³⁴S$_{VCDT}$ and bulk δ³⁴S$_{VCDT}$. Analyses grouped by sample.

5.2.4 Relationship between in-situ $\delta^{34}S_{VCDT}$ and other parameters

Data were graphed by sample, and grouped based on numerous parameters including As content, grain type, and spot location of the in-situ SIMS analyses. The As content classifications were divided into low, intermediate and high based on an As contents of <1 wt. %, 1-3 wt. %, and >3 wt. %, respectively. Grain type classifications were divided into "clean", "sieve", "fracture", and a combination of sieve and fracture textures, based on the location of in-situ SIMS compared to BSE images. Spot location classifications were divided into "core" and "rim" where compositional zoning relationships were apparent, "grain" where compositional zoning relationships were not apparent, and "overgrowth" where there was distinct new growth on the outside edges of the pyrite grains.

Data plotted based on As content did not show any relationship between samples, but showed trends within specific individual samples (Figure 30). Sample 18KG015 showed that while there was slight overlap, spots with higher in-situ $\delta^{34}S_{VCDT}$ values (0.7 ‰ – 2.0 ‰) had lower As content (0.47 wt. % – 0.79 wt.%), and spots with lower in-situ $\delta^{34}S_{VCDT}$ values had intermediate As content (1.16 wt. % – 2.85 wt. %). Sample 18KG020 showed the opposite in that spots with higher in-situ $\delta^{34}S_{VCDT}$ values (-0.2 ‰ – 1.2 ‰) had higher As content (1.39 wt. % – 3.51 wt. %) and spots with lower in-situ $\delta^{34}S_{VCDT}$ values had lower As content (0.31 wt. % – 1.21 wt. %).

Data plotted based on grain type did not show any relationship between samples, nor trends within individual samples (Figure 31). This evidence suggests

that the mechanism controlling ^{34}S fractionation is not related to grain type according to the textural classifications used.

Data plotted based on spot location did not show strong relationships between samples but showed trends within some individual samples (Figure 32). Pyrite from Nuttby Mountain showed distinct differences between cores and rims, with cores (As-poor) showing $\delta^{34}S_{VCDT}$ values ranging from -1.8 ‰ to -0.6 ‰ and rims (As-rich) showing $\delta^{34}S_{VCDT}$ values between -3.0 ‰ and -6.8 ‰. Pyrite from Warwick Mountain showed indistinct differences between cores and rims, with cores (As-rich) showing $\delta^{34}S_{VCDT}$ values ranging from -1.5 ‰ to 0.7 ‰ and rims (As-poor) showing $\delta^{34}S_{VCDT}$ values between -1.9 ‰ and 0.6 ‰. Pyrite from Core 1 and Core 2 samples showed few distinct differences in the $\delta^{34}S_{VCDT}$ of different zones in pyrite. In pyrite grains where compositional zoning relationships were not apparent ("grain"), $\delta^{34}S_{VCDT}$ values were highly variable, ranging from -4.8 ‰ to 1.7 ‰. In samples where compositional zoning relationships were apparent between rim and core, relationships were weak but significant. In samples 18KG014 and 18KG015, grain cores generally returned more positive $\delta^{34}S_{VCDT}$ values while rims generally returned more negative $\delta^{34}S_{VCDT}$ values similar but not as pronounced as in the Nuttby Mountain pyrite.

An individual pyrite grain from 18KG016 (Core 1) had an overgrowth that returned extremely positive $\delta^{34}S_{VCDT}$ values (24.8 ‰ and 26.4 ‰). The grain showed minor sieve texture, and the overgrowth had a low As content (0.45 wt. % and 0.30 wt. %).

In-situ SIMS analysis of marcasite grains from surface sample 16TM0096A returned all positive $\delta^{34}S_{VCDT}$ values with no differences in composition between marcasite and associated pyrite (Figure 33).

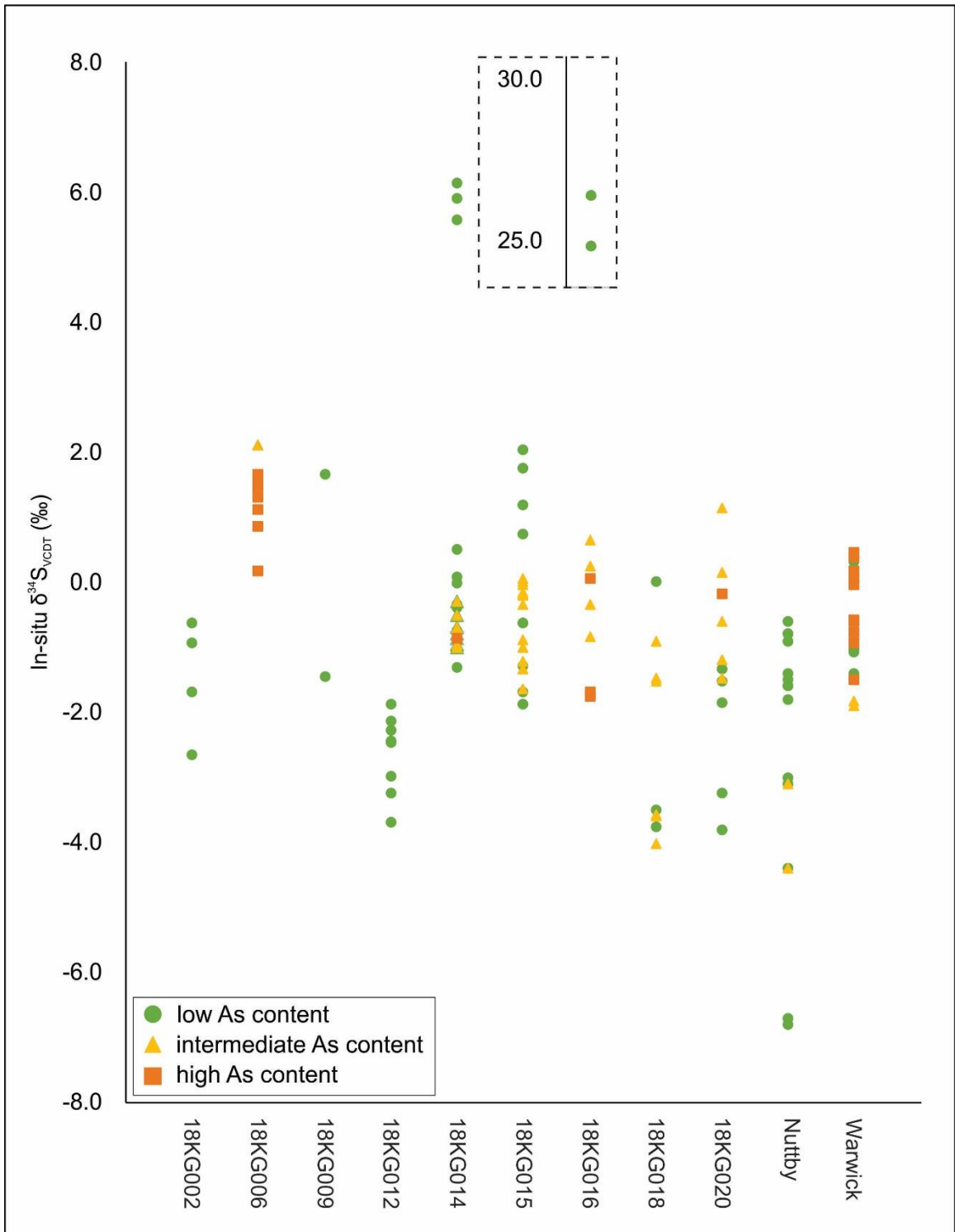Figure 30 - Graph depicting in-situ δ³⁴S$_{VCDT}$ results, with analyses grouped by sample and categorized based on As content.
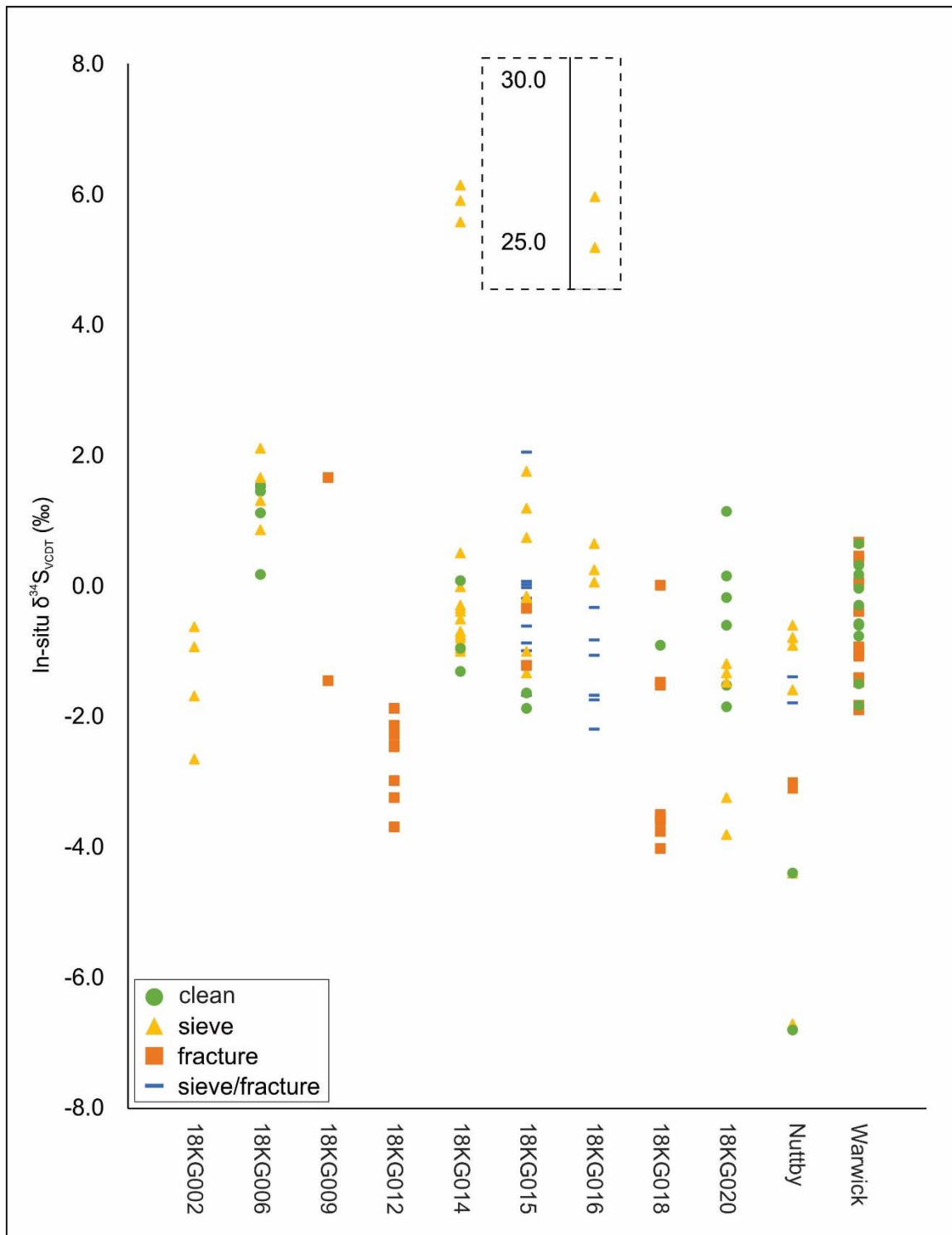
Figure 31 - Graph depicting in-situ δ^{34}S[VCDT] results, with analyses grouped by sample and categorized based on grain type.
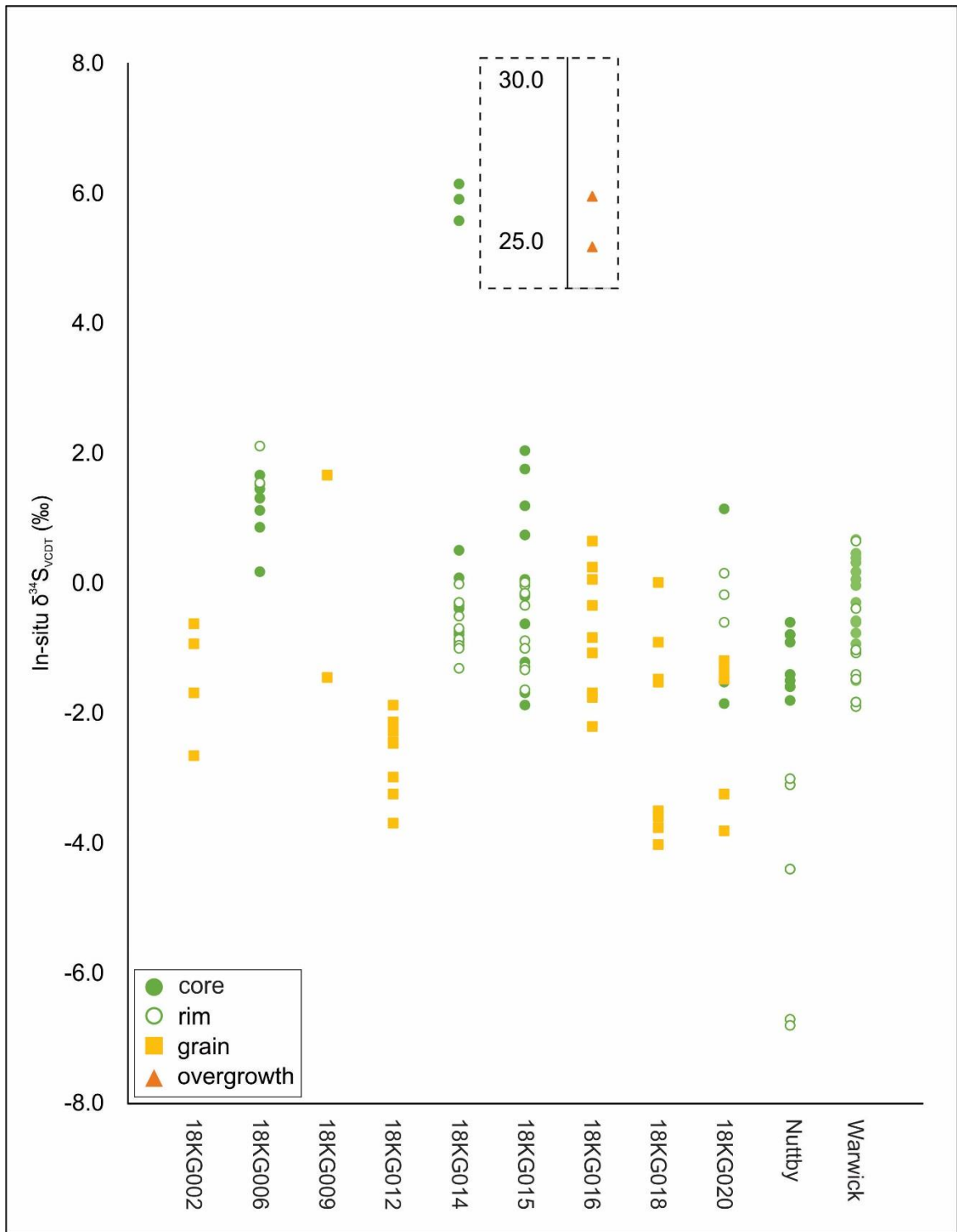
Figure 32 - Graph depicting in-situ $\delta^{34}S_{VCDT}$ results, with analyses grouped by sample and categorized based on SIMS spot location.
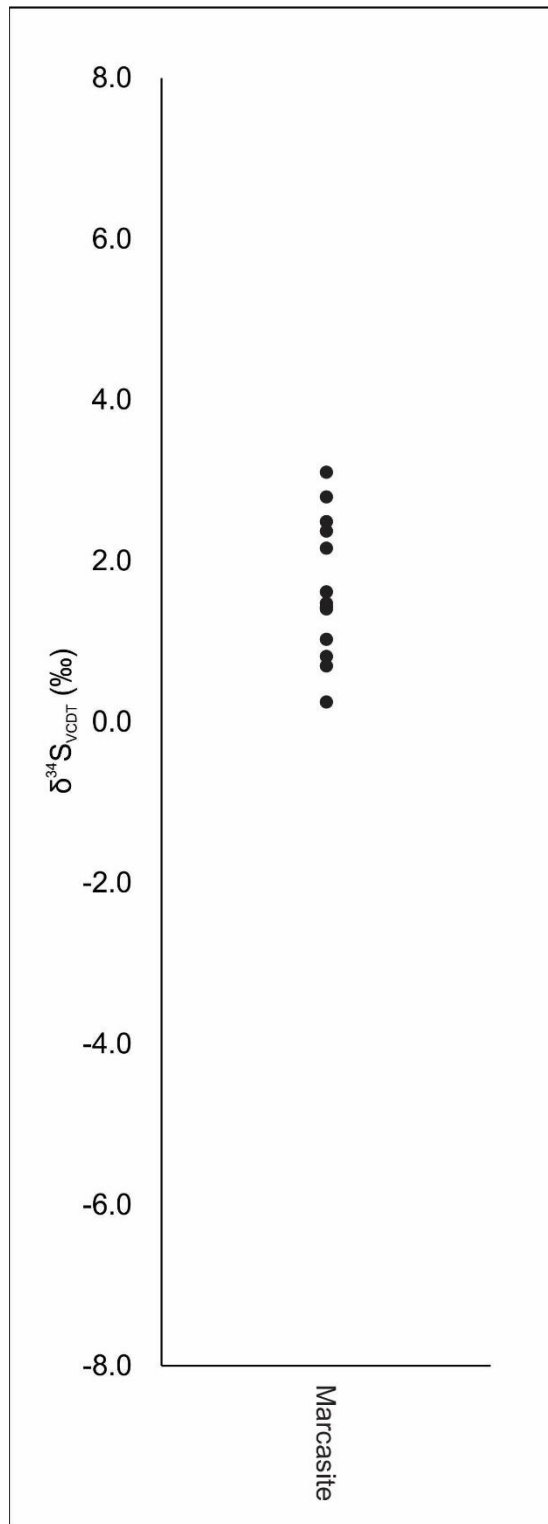
Figure 33 - Graph depicting in-situ δ34SVCDT results of marcasite grain from surface sample.

5.3 Relationship between pyrite chemistry, S isotopes and mineralizing

processes

Coincidence of As-Hg-Se-Sb±Au precipitation (in pyrite zoning), coupled with a lack of Cu mineralization, and minor enrichment in base metals Pb and Zn are features consistent with a low sulphidation epithermal environment. Pyrite (and associated gangue) textures, pyrite trace element chemistry, and S isotope composition suggest that mineralization at the Warwick and Nuttby Mountain occurrences, and in some core samples (18KG014, 18KG015 and 18KG020) formed from fluids that underwent large changes in physical and chemical parameters. However, these changes were markedly different between the sites. At Warwick Mountain, early growth of As-Hg-Se-Sb-enriched arsenian pyrite was followed by a period of overgrowth of relatively trace metal-poor pyrite on early arsenian pyrite cores, and neither stage of pyrite growth was associated with Au precipitation. At Nuttby Mountain, early pyrite is trace metal-poor and shows evidence of extensive dissolution under disequilibrium conditions, followed by a period of overgrowth of As-Sb-enriched arsenian pyrite with the later stage coincident to Au enrichment (~ 10 ppm Au in pyrite). Whereas Au-enriched pyrite overgrowths at Nuttby Mountain coincide to a marked decrease in $\delta^{34}S_{VCDT}$ of up to ~6 ‰ compared to Au-poor cores, this decrease is less apparent or absent at Warwick Mountain. In drill core sample 18KG014, mapped adjacent pyrite grains show different growth histories. Grain 1 is characterized by an As-rich rim, while Grain 2 is characterized by a Ag-Hg-rich rim and a As-rich rim. Both grains show minor late Au enrichment (~ 10 ppm) on the rim of pyrite grains and infilling sieve

texture pits. Both grains show oscillatory zones of As enrichment that generally do not correspond to marked differences in $\delta^{34}S_{VCDT}$ values. Grain 1 shows indistinct differences in $\delta^{34}S_{VCDT}$ values (0.0 ‰ – -0.9 ‰). The individual in-situ $\delta^{34}S_{VCDT}$ analysis on Grain 2 shows comparable $\delta^{34}S_{VCDT}$ values to Grain 1 (-0.8 ‰).

In general, there is not a systematic core-rim variation in all samples because there are numerous types of zoning present. However, in some samples such as at Nuttby and Warwick Mountain, and 18KG014, 18KG015 and 18KG020 from drill core, there are systematic variations in $\delta^{34}S_{VCDT}$ between growth zones independent of As content. There are several possible explanations for this.

When temperature changes, the magnitude of sulphur fractionation between the fluid and respective pyrite in equilibrium with the fluid changes. At low temperatures, the amount of sulphur isotope fractionation is very large and then gets progressively smaller as temperature increases. Therefore, zones with lower $\delta^{34}S_{VCDT}$ values relative to higher $\delta^{34}S_{VCDT}$ values may grow from the same source fluid, but at different temperatures. Lower values of $\delta^{34}S_{VCDT}$ in pyrite rims, for example, may reflect hotter growth temperatures relative to $\delta^{34}S_{VCDT}$ enriched cores.

Fluid composition can also affect $\delta^{34}S_{VCDT}$ values. Lighter fluids ([34]S-depleted) will source lower $\delta^{34}S_{VCDT}$ pyrite while heavier fluids ([34]S-enriched) will source higher $\delta^{34}S_{VCDT}$ pyrite. Therefore, zones with lower $\delta^{34}S_{VCDT}$ values may have grown from more [34]S-depleted fluid entering the system.

A boiling event can also affect δ³⁴S$_{VCDT}$ values, causing the remaining fluid to reach a more oxidized state. Oxidation would lead to a preferential partitioning of ³⁴S into SO$_2$ or SO$_4$:

$$H_2^{34}S_{(aq)} + 4H_2O \rightarrow {}^{34}SO_{4\ (aq)}^{-2} + 2H^+ + 4H_{2(g)}.$$
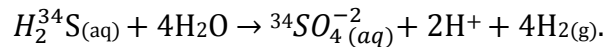
This would leave progressively lighter H$_2$S in the liquid phase, to be incorporated into pyrite:

$$2H_2^{32}S_{(aq)} + Fe^{2+} \rightarrow Fe^{32}S_2 + H_{2(g)} + 2H^+.$$
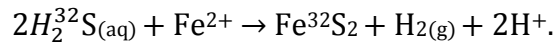
Ultimately this would result in zoned pyrite crystals with heavier cores (pre-boiling) and lighter rims (post boiling).

There may also be a relationship between sulphur isotope zonation and gold deposition in a boiling system as boiling induced H$_2$S loss leads to Au precipitation (from bisulphide complexes; McKibben and Eldridge, 1990).

5.4 Origin of δ³⁴S$_{VCDT}$-enriched pyrite overgrowths

Analysis of δ³⁴S$_{VCDT}$ in pyrite grains by SIMS returned a few anomalously high δ³⁴S$_{VCDT}$ values (24.8 ‰ and 26.4 ‰) in an overgrowth on one pyrite grain from sample 18KG016 (Figure 15G). This is likely reflecting a sulphide sourced from the reduction of seawater sulphate either from seawater or an evaporitic succession above the volcanic sequence. Volcanic units near the location of the drill holes yielded a maximum igneous age of 354.59 ± 0.11 Ma (MacHattie, 2018). The overlying Windsor Group, a carbonate-evaporate succession in the Maritimes Basin, is dated at 334 – 330 Ma (Schenk et al., 1994; von Bitter et al., 2003; Giles, 2009; MacNeil et al., 2018). Seawater (and associated evaporates) during the

early-mid Carboniferous had a $\delta^{34}S_{VCDT}$ value in the range of 20 to 25 ‰ (Rees et al., 1978; Sharp, 2007).

It is possible that incursion of sulphide formed by sulphate reduction affected ongoing mineralizing processes in the underlying bi modal volcanic rocks or that sulphide derived from marine sulphate was introduced at a later date as overgrowths on pyrite. If all of the pore water sulphate was converted to sulphide by dissimilatory sulphate reduction in a "closed system", bulk pyrite overgrowths would have the same $\delta^{34}S_{VCDT}$ values as the dissolved seawater (or evaporate) sulphate (Sharp, 2007).

5.5 Implications for regional exploration

The S isotope signatures reflecting changes in fluid composition or temperature, or boiling, obtained from in-situ SIMS analysis of pyrite are not recognized when using conventional bulk isotopic analytical techniques, validating the necessity for in-situ analysis in weathered surface and core samples. At the Nuttby Mountain Au occurrence and in some core samples in the study area, the distinct drop in $\delta^{34}S_{VCDT}$ values from core to rim in zoned pyrite coincides with Au enrichment in the rims of the pyrite. This provides a valuable exploration tool in locating potential areas of Au mineralization.

6.0 Conclusion

Overall, the findings throughout this study are consistent with a low sulphidation epithermal environment. Host rock setting, assay results showing enrichments in

Au, As, Sb, and Hg, and sulphide mineralogy and gangue textures are all consistent with low sulphidation epithermal gold style of mineralization. The bulk S (as mainly pyrite) correlates to bulk $\delta^{34}S_{VCDT}$. The As content of pyrite correlates to in-situ $\delta^{34}S_{VCDT}$ in pyrite weakly but significantly ($r = 0.343$), likely a result of high As, high $\delta^{34}S_{VCDT}$ zones in pyrite being coincident in a significant number of samples. Bulk $\delta^{34}S_{VCDT}$ correlates to in-situ $\delta^{34}S_{VCDT}$ but bulk $\delta^{34}S_{VCDT}$ values are consistently higher by several ‰, suggesting partial oxidation of sulphides to SO_4 and loss of ^{32}S in core during storage. One sample contained pyrite grains with overgrowths showing very high $\delta^{34}S_{VCDT}$ values, likely attributed to reduction of seawater sulphate possibly from the formerly overlying Windsor Group. There are systematic core-rim relationships in surface samples and a few core samples. The biggest change between core and rim $\delta^{34}S_{VCDT}$ to more negative values in the rim occurs at the Nuttby Mountain occurrence, where there is also trace Au (~ 10 ppm) in the rims of pyrite grains. Trace Au (~ 10 ppm) is also observed in the rim of some pyrite grains in drill core samples, though these do not show the same systematic core-rim variations in $\delta^{34}S_{VCDT}$ and As that are seen at the Nuttby Mountain occurrence. These techniques can be paired together to help vector exploration to potential mineralized low sulphidation epithermal gold systems where changes in fluid chemistry or temperature are preserved in single pyrite grains but are otherwise obscured in bulk samples that have been weathered.

References

Dessureau, G., Piper, D. and Pe-Piper, G., 2000, Geochemical evolution of earliest Carboniferous continental tholeiitic basalts along a crustal-scale shear zone, southwestern Maritimes basin, eastern Canada; Lithos, v. 50, p. 27-50.

Donohoe, H. V. and Wallace, P. I., 1982, Geological map of the Cobequid Highlands, Colchester, Cumberland, and Pictou counties, Nova Scotia, Sheet 1 of 4; Nova Scotia Department of Mines and Energy, Map 1982-6, scale 1:50 000.

Dunning, G. R., Barr, S. M., Giles, P. S., McGregor, D. C., Pe-Piper, G. and Piper, D. J. W., 2002, Chronology of Devonian to early Carboniferous rifting and igneous activity in southern Magdalen Basin based on U-Pb (zircon) dating; Canadian Journal of Earth Sciences, v. 39, p. 1219-1237.

Hedenquist, J., Arribas, A., and Gonzalez-Urien, E., 2000, Exploration for Epithermal Gold Deposits. Reviews in Economic Geology. 13. 245-277.

Holliger, P., and Cathelineau, M., 1988, In situ U-Pb age determination by secondary ion mass spectrometry: Chemical Geology, v. 70, p. 173.

Jensen, L., 2012, Drill program, Whirley Brook Lic#09724, Colchester County, NS; Nova Scotia Department of Natural Resources, Activities Report AR2012-077, 93 pages.

John, D.A., 2001, Miocene and early Pliocene epithermal gold-silver deposits in the northern Great Basin, USA: Characteristics, distribution, and relationship to magmatism; Economic Geology, v. 96, p. 1827–1853.

Little, B., Wagner, P., and Jones-Meehan, J., 1994, Sulphur isotope fractionation in sulfide corrosion products as an indicator for microbiologically influenced corrosion (MIC), *Microbiologically Influenced Corrosion Testing, ASTM STP 1232,* Jeffrey R. Kearns, and Brenda J. Little, Eds., American Society for Testing and Materials, Philadelphia, pp. 180-187.

MacHattie, T. G., 2011, Volcanic stratigraphy and nature of epithermal-style gold mineralization in Upper Devonian-Lower Carboniferous volcanic rocks of the northeastern Cobequid Highlands, Nova Scotia; in Mineral Resources Branch, Report of Activities 2011; Nova Scotia Department of Natural Resources, Report ME 2011-002, p. 14.

MacHattie, T. G., 2013, Newly recognized epithermal-style gold occurrences associated with Late Devonian to Early Carboniferous bimodal volcanism in the northeastern Cobequid Highlands; in Mineral Resources Branch, Report of Activities 2011; Nova Scotia Department of Natural Resources, Report ME 2012-001, p. 31-39.

MacHattie, T. G., 2016, An Update on Bedrock Mapping and Exploration for Epithermal Gold in the Northeastern Cobequid Highlands; in Mineral Resources Branch, Report of Activities 2016; Nova Scotia Department of Natural Resources, Report ME 2016-2017, p. 49-52.

MacHattie, T. G., 2018, Preliminary bedrock geology map of the eastern Cobequid Highlands, Nova Scotia; Nova Scotia Department of Natural Resources, Geoscience and Mines Branch, Open File Map ME 2018-005, scale 1:35000.

MacNeil, L. A., Pufahl, P. K., and James, N. P., 2018, Deposition of a saline giant in the Mississippian Windsor Group, Nova Scotia, and the nascent Late Paleozoic Ice Age; Sedimentary Geology, v. 363, p. 118-135.

McFarlane, C., and Luo, Y., 2012, U–Pb geochronology using 193 nm excimer LA–ICP-MS optimized for in situ accessory mineral dating in thin section. Geoscience Can. 39, 158–172.

Paton, C., Hellstrom, J., Paul, B., Woodhead, J., and Hergt, J., 2011, Iolite: Freeware for the visualization and processing of mass spectrometer data: Journal of Analytical Atomic Spectrometry, v. 26, p. 2508–2518.

Pe-Piper, G., Piper, D. J. W., 2002., A synopsis of the geology of the Cobequid Highlands, Nova Scotia. Atlantic Geology, v. 38, p. 145-160.

Poulsen, K. H., 1996., Lode gold: in Geology Mineral Deposit Types, (ed.) O.R. Eckstrand, W. D. Sinclair, and R. I. Thorpe; Geological Survey of Canada, Geology of Canada, no. 8, p. 323-328.

Riciputi, L.R., Paterson, B.A., and Ripperdan, R.L., 1998, Measurement of light stable isotope ratios by SIMS: Matrix effects for oxygen, carbon, and sulphur isotopes in minerals: International Journal of Mass Spectrometry, v. 178, p. 81–112.

Sharp, Z., 2007. Principles of stable isotope geochemistry. Pearson Education Inc., New Jersey.

Appendix
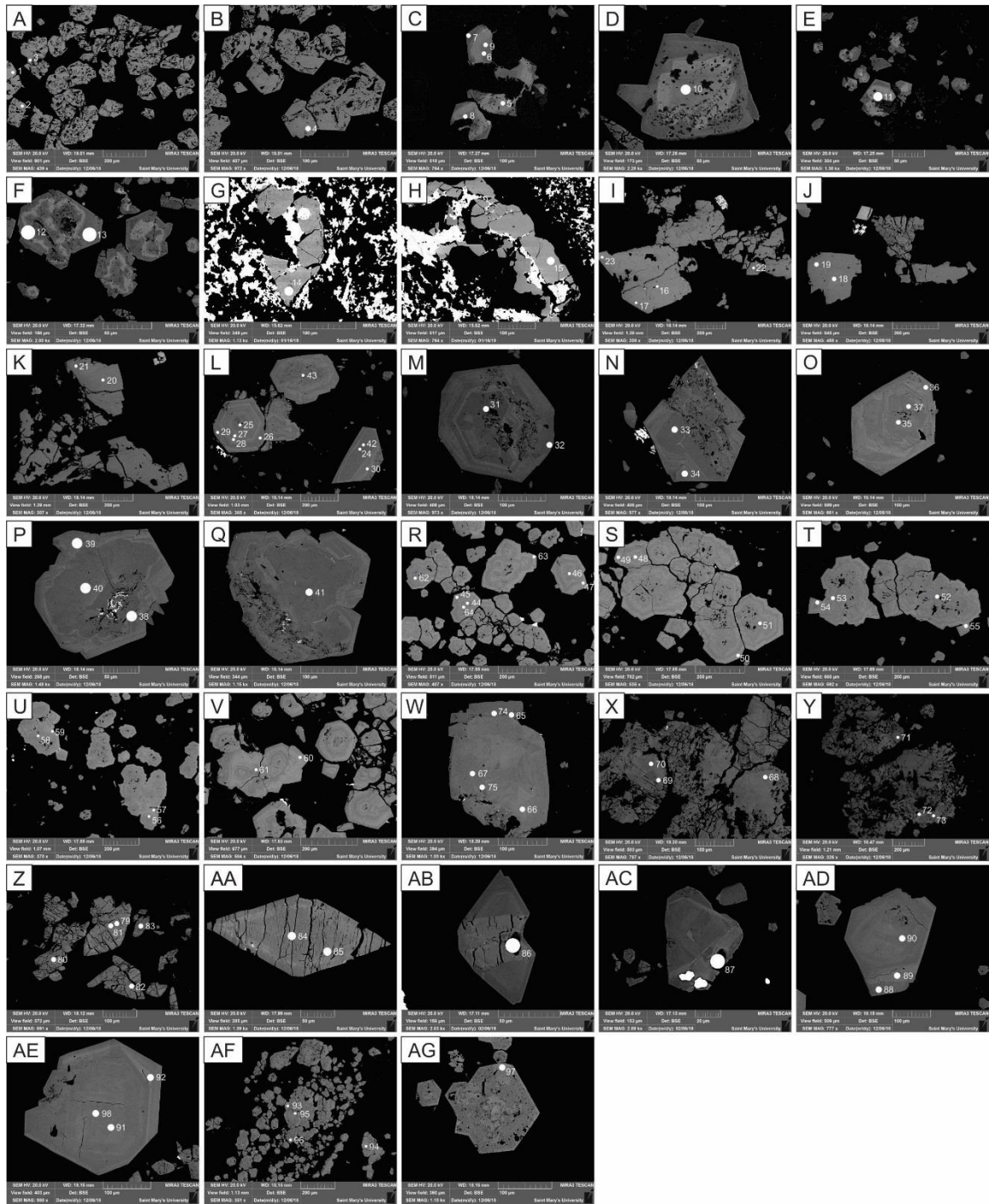
Note: Bright phases in G and H are gold coating remnants from SIMS analysis.